Characterisation of flow and bubble phenomena in a high pressure alkaline water electrolyser.

by

T. Kleist

to obtain the degree of Master of Science
at the Delft University of Technology,
to be defended publicly on Thuesday July 6, 2021 at 10:00 AM.

Student number:	4212746	
Project duration:	August 1, 2020 – July 6, 2021	
Thesis committee:	Dr. ir. J. W. Haverkort,	TU Delft, supervisor
	Dr. ir. W. P. Breugem,	TU Delft
	Dr. ir. M. T. De. Groot,	Nouryon
	Ir. J. Van. Kranendonk,	Zero Emission Fuels

TU Delft

Abstract

Zero Emission Fuels B.V (ZEF) is currently in the process of designing and prototyping a sustainable methanol micro-plant, which captures water vapor and carbon dioxide from the atmosphere and uses those components to eventually produce methanol. In order to produce methanol, hydrogen is required which is produced from the captured water by electrolysis in a zero gap design, high pressure alkaline water electrolyser. The pressure in the electrolysis setup is regulated at a desired operating pressure of 50 bar by a pressure control system, designed by ZEF.

Insight is required in how the flow of electrolyte and bubbles behaves in the electrolysis setup and the electrolyser cells, in order to implement design or operation condition changes to allow for an efficient operation in the eventual micro-plant.

This study focuses on the experimental characterization of the flow and bubble phenomena in the ZEF electrolyser design, during operation at a desired pressure of 50 bar, with the use of visualization by video footage inside the electrolyser cells. Camera equipment used for the visualization consists of a microscope camera and a GoPro camera. An ultrasound Doppler velocimetry device (UDV) was used to measure the electrolyte flow velocity and direction in different parts of the electrolysis setup, in order to substantiate findings made by the camera equipment.

Experiments were conducted with an electrolysis setup based on the current electrolyser design made by ZEF, with the addition of a transparent add-on to allow for visualization of the flow and bubbles inside an electrolyser cell on the oxygen side. First the operation of the electrolyser was characterized by means of IV curves and temperatures, followed by visualization experiments for varying operating pressures and current densities at different parts of the electrolyser cell.

One of the main observations made during the visualization experiments is the periodic occurrence of stagnation of electrolyte and gas flow out of the electrolyser. Stagnation of the flow occurs inside the electrolyser cells on the oxygen side, at the top channels leading the flow out of the electrolyser cells, to eventually a flash tank. Different multiphase flow regimes were observed during active flow through the top channels, which vary based on the operating current density, pressure and temperature. Bubble behavior was observed at different positions on the electrode in the electrolyser cell and possible enhancement of gas crossover was detected in the electrolysis setup and investigated.

The effect of the pressure control system on the operation of the electrolyser was also investigated and showed to affect the electrolyte flow direction in the electrolysis system. Models were made to validate and explain the findings from the visualization video footage and characterization of the electrolyser. A previous made model that characterizes the flow in the electrolysis system is used for comparison.

Due to the lack of a temperature regulation system, a finned tube heat exchanger was modelled to be implemented in the experimental setup as for the eventual electrolysis setup.

Based on the findings from the experiments, recommendations are proposed regarding the experimental and eventual design, and for further development of the high pressure alkaline water electrolyser and the electrolysis system.

Acknowledgements

First and foremost I would like to thank my parents, **Rein & Els Kleist**, for always supporting me throughout my entire life. You believed in me during my study and showered me with love and understanding, for which I am forever grateful. I could not have gone this far without the foundation you gave me.

Furthermore I would like thank my girlfriend, **Iris Brandenburg** for supporting me and providing me with an enormous amount of positive energy and love. You helped me during the more difficult periods of this thesis and make sure I enjoy life to the fullest.

I would like to thank **Willem Haverkort** and **Jan van Kranendonk** for guiding me through my thesis by being my supervisor and daily supervisor respectively. I have learned a lot under your guidance and your enthusiasm made me strive to learn more and dive deeper into my thesis subject. The bi-weekly sessions with **Willem Haverkort** provided direction for my research and made me more interested into the topic of my thesis. You were always enthusiastic about my findings and patient with how I progressed during the thesis. You even arranged a small presentation for the King and I could not think of a better supervisor. **Jan van Kranendonk** always provided me with an engineering view onto occurring problems and issues, and suggestions how to solve them. You motivated me during me entire thesis to keep going and getting the best results possible.

Thanks to the ZEF team, consisting of **Jan, Ulrich, Hessel and Migrank**. I really enjoyed my time at ZEF and working under your supervision during my internship and my thesis. Your ideas and vision really inspired me. You were always open for a talk about the project and providing useful tips and tricks to help me finish my thesis in the best way possible. The coffee card, which I used quite a lot, was also a wonderful source of focus the last weeks of my thesis.

I am also grateful to **Ilco Krikke**, for being my study partner for over 7 years and walking the road to graduation together with me from bachelor to master. Without you, studying for the exams would be so much harder and the road would be a lot harder to walk.

I would like to express my thanks to my fellow students at ZEF for the wonderful time I had with them during my thesis. It was an awesome time together with **Bart, Bart, King Kamal, Samir, Gijs, Shahrukh, Khaled, Michiel, Thorsten, Shawn and the ZEF team**. The interesting discussions and welcome distraction really helped me during my thesis. But most of all the positive vibe in the ZEF team kept me going, thank you!

Finally, I would like to thank all my friends who were with me during my journey as a student. Thanks to **Ralf, Yannick, Erik, Daniel, Thomas, Luuk, Maarten, Menno, Rik, Peter, Guilhem, Tarik, Marc, Wim**.

Tom Kleist
Delft, July 2021

Contents

Nomenclature

Greek symbols

α	Contact angle	[-]
α	electron transfer coefficient	[-]
β'	Temperature inverse	$[K^{-1}]$
β	Contact angle	[-]
γ	Efficiency	[-]
η	Activation overpotential	[-]
ϵ	Porosity	[-]
ϵ	Void fraction	[-]
Δ	Difference	[-]
K	Heat capacity ratio	[-]
K	Specific conductivity	$[S/m]$
ν	Kinematic viscosity	$[m^2/s]$
π	Number of Pi	[-]
ρ	Density	$[kg/m^3]$
Θ	Constant for heat exchanger calculation	[-]
ϕ	Circumferential angle	[-]
Ψ	Prandtl number function	[-]
σ	Surface tension	$[kg/s^2]$
σ	Electrical conductivity	$[S/m]$
θ	Angle	[-]
θ	Bubble coverage	[-]
τ	Tortuosity	[-]

Roman symbols

A	Area	$[m^2]$
C	Specific heat	$[J/kgK]$
c	Concentration	$[mol/m^3]$
d	Diameter	$[m]$
e	Electron	[-]
d	Diameter	$[m]$
D	Diffusivity	$[m^2/s]$
E	Heat transfer coefficient	$[W/m^2K]$
f	Darcy-Weisbach constant	[-]
F	Faraday constant	[-]
F	Force	[N]
G	Gibbs free energy	$[J/kg]$
H	Enthalpy	$[J/kg]$
h_c	Heat transfer coefficient	$[W/m^2K]$
h_v	Virtual heat transfer coefficient	$[W/m^2K]$
I	Ampere	[A]
j	Current density	$[A/cm^2]$
k	Thermal conductivity	$[W/mK]$
K	Permeability	$[m^2]$
K	Resistance coefficient	$[kg/sm^4$
L	Length	$[m]$
$LMTD$	Log mean temperature difference	$[K]$
$\dot{m}$	Mass flow	$[kg/s]$
$\dot{n}$	Molar flux	$[mol/m^2s]$
Nu	Nusselt number	[-]
p	Pressure	[bar]
P	Wetted perimeter	[m]
Pr	Prandtl number	[-]
Q	Generated heat	$[W]$
r	Radius	$[m]$
R	Resistance	[Ω]
R	Gas constant	$[m^3pa/Kmol]$
Ra	Rayleigh number	[-]
Re	Reynolds number	[-]
s	Fin spacing	[m]
S	Entropy	$[J/kg \cdot K]$
t	Time	[s]
T	Temperature	$[K]$
u	Velocity	$[m/s]$
U	Voltage	$[V]$
v	Molar volume	$[m^3/mol]$
$\dot{V}$	Volumetric flow rate	$[cm^3/s]$
X	Constant for heat exchanger calculation	[-]
z	Number of electrons	[-]

Subscripts

a	Air stream
air	Air
$anode$	Anode
am	Ambient air
b	Base
B	Buoyancy
$bubble$	Bubble
$cathode$	Cathode
$cell$	Electrolyser cell
$circuit$	Circuit
$crirc$	Circular
$crit$	Critical
dia	Diaphragm
$diff$	Diffusion
D	Drag
$elec$	Electrolyte
eff	Effective
f	Fin
$footer$	Footer channel
$Faradic$	Faradic
g	Gas
$header$	Header channel
$heat$	Heat exchanger
HHV	Higher heating value
i	Inner
i	Specific component
in	Inlet
$ions$	Ions
l	liquid
L	lift
mem	Membrane
$meter$	Per meter
o	Outer
out	Outer
p	At constant pressure
$pore$	Pore
r	Mean
rev	Reversible
r	Mean
$slug$	slug
S	Interfacial
th	Thermal
$total$	Total
$tube$	Tube
v	At constant volume
$voltage$	Voltage
V	Volumetric
x	X direction
y	Y direction
Y	Yield

Chemical

CH_3OH	Methanol
CO_2	Carbon Dioxide
H_2	Hydrogen
H_2O	Water
KOH	Potassium hydroxide
O_2	Oxygen
HO^-	Hydroxide

Abbreviations

AEC	Alkaline electrolysis cell
AWE	Alkaline water electrolysis
DAC	Direct air capture
EU	European union
FM	Fluid machinery
HHV	Higher heating value
KOH	Potassium hydroxide
LEL	Lower explosion limit
MS	Methanol synthesis
PEM	Polymer electrolyte membrane
PSU	Polysulfone
UEL	Upper explosion limit
ZEF	Zero Emission fuels

1

Introduction.

1.1. Global warming and the use of sustainable energy.

The world is in great demand of energy to keep the planet running. It relies heavily on the use of fossil fuels for its energy production, as well for other products like plastics [40]. The large scale use of fossil fuels over the past years has depleted the reserves present at our globe [56]. The depletion is rapidly increasing and will leave our society with the problem of finding alternative energy sources.

Since the end of the 19th century the use of fossil has been increasing ever since with an alarming rate. The industrial revolution has led to the increase of use of coal at first. Halfway the 20th century the use of crude oil and natural gas became more popular besides coal. The graph in figure 1.1 shows the consumption of fossil fuels since the 19th century [50].

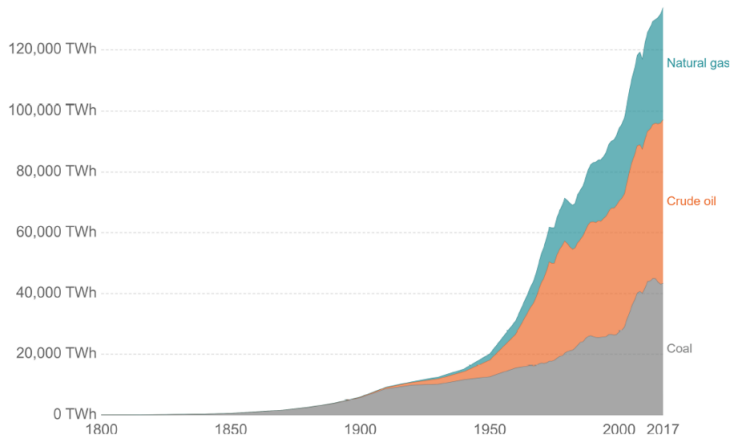

Figure 1.1: Fossil fuel consumption world wide since the 19th century [50].

From the graph it becomes clear that in the last decades the consumption of the of fossil fuels has seen the largest increase and even now is increasing. The reserves of fossil fuels, present at our globe, will eventually be exhausted if they are not given the time to replenish [56]. Besides the eventual exhaustion of the fossil fuels, there is an even larger problem occurring with the large scale use of fossil fuels. The last few decades, the use of fossil fuels has led to an increase in the atmospheric carbon dioxide concentration at our planet [74]. If one looks at the annual total carbon dioxide (CO_2) emission world wide for the last three centuries, a rapid increase since the 1950's becomes visible [48].

Carbon dioxide is called a greenhouse gas. The release of greenhouse gasses in the atmosphere the last few decades has led to the greenhouse effect, which results in the steadily increase of the global average temperature [39]. The global warming of the planet has to be limited, otherwise the rise of the global average temperature will increase to an alarming level. The Paris Agreement by the United Nations aimed at holding the global warming well below 2 °C [51]. Even at the best scenario, where the emission of greenhouse gasses will only see a minor growth, the global average temperature will increase with approximately 2 °C [38]. This will have a large negative impact on the planet, so renewable sources of energy are required to fill the energy consumption need.

The last few years there is a positive, and necessary, growth in the use of renewable energy sources. The energy production from clean sources, namely solar, wind and hydro energy, has increased significantly, as shown in figure 1.2. Over the years, research has been done on renewable energy [32], and it is expected that renewable energy sources will provide between 30 % and 80 % of the world energy demand in 2100 [42].

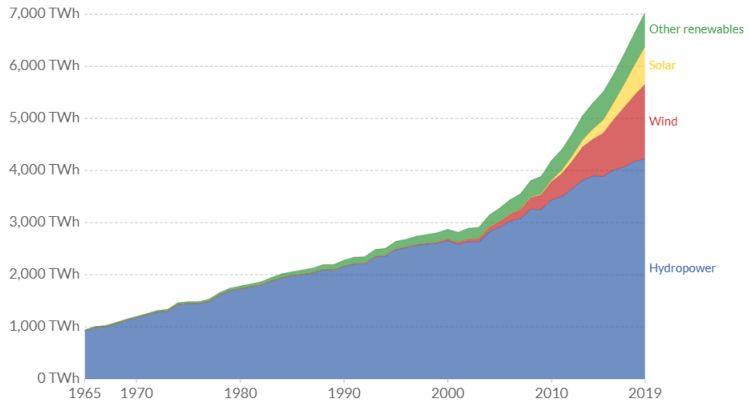

Figure 1.2: Increase in energy production by renewable energy sources from 1965 to 2019 [49].

A lot of research is done on the CO_2 emission neutral or free energy production and the technologies to do so become more efficient. Besides the providing of energy in the form of clean electricity, there is also the demand of a clean fuel which can be used for transportation and energy production or storage purposes. Methanol is a substance which can meet to this demand. It can be used as a storage medium to store electrical generated energy into chemical energy [47]. The storage can be done in the form of a liquid fuel which can easily be transported. Methanol can be used as a fuel, or fuel additive, to power vehicles [25]. The production of methanol can come from a lot of different sources, which makes it more attractive to produce. In the end is methanol a clean energy source that has a lot of positives as an energy storage medium and for energy production.

1.2. Zero emission fuels B.V.

Zero Emission Fuels B.V (ZEF) is a start-up company that is specialized in zero emission technology. Their goal is to produce methanol with a process that is CO_2 neutral, to contribute in a positive way to the global warming of the planet. ZEF is currently working on designing and prototyping a micro-plant which will be used for methanol synthesis. The production of methanol is powered by the surplus energy of solar panels. The micro-plant is able to capture water and CO_2 from the atmosphere, and uses those as feed stock for the methanol synthesis.

The future as seen by ZEF, is a large solar panel farm with small micro-plants connected to three solar panels each. The advantage of the micro-plants are that they can be easily disconnected from the solar panels for maintenance or repairs. Because of the small size and flexibility, the micro-plants allow for dynamic operation and have a potential for mass production.

1.2.1. ZEF micro-plant.

The ZEF micro-plant is divided into five subsystems which each contribute to the production of methanol from sunlight and air. Each sub-system has his own task and works together with the other subsystems in order to let the micro-plant produce methanol. The five subsystems and a short description are presented below:

- **Direct Air Capture (DAC)**: Captures CO_2 and water vapor from the atmosphere. The system separates the captured gasses into two product streams.
- **Fluid Machinery (FM)**: The captured CO_2 is transported to the FM subsystem and pressurized to a pressure of 50 bar. Possible presence of water is purged from the product stream.
- **Alkaline Electrolysis (AEC)**: In this subsystem water is converted at high pressure into hydrogen and oxygen, by an alkaline water electrolyser. The hydrogen is supplied to the methanol synthesis subsystem and the oxygen is sent to a degasser unit.
- **Methanol Synthesis (MS)**: The produced hydrogen and the pressurized CO_2 are supplied to the MS subsystem and are synthesized to form methanol and water.
- **Distillation (DS)**: During the synthesis of methanol, water is formed as a byproduct. In order to produce grade AA (98% pure) methanol the water is separated from the final product by a distillation column.

The five subsystems can be presented in the form of a process diagram. A simplified version of the process diagram of the ZEF micro-plant can be seen in figure 1.3.

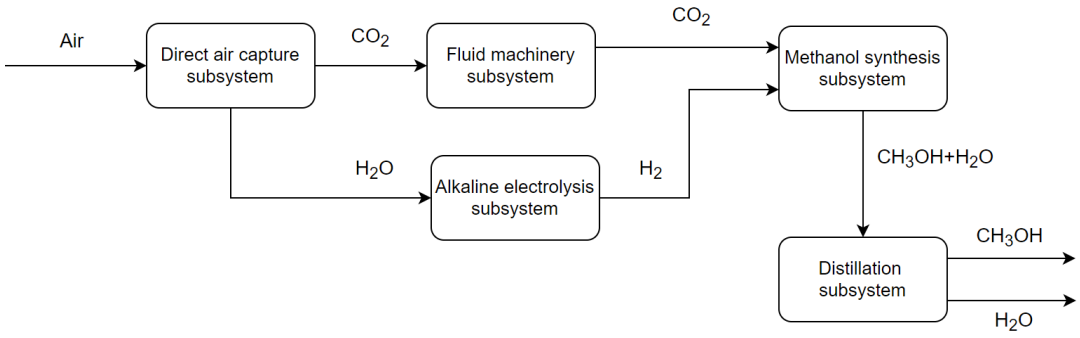

Figure 1.3: Simplified process diagram of the ZEF micro-plant, containing the five subsystems. Focus of this thesis is on the AEC subsystem.

1.2.2. Alkaline Electrolysis subsystem.

The focus of this thesis is on the alkaline water Electrolyser in the AEC subsystem. The AEC subsystem consists of four smaller subsystems: a pressure booster, a degasser unit, the alkaline water electrolyser and two flash separators. Figure 1.4 shows a schematic representation of the AEC subsystem.

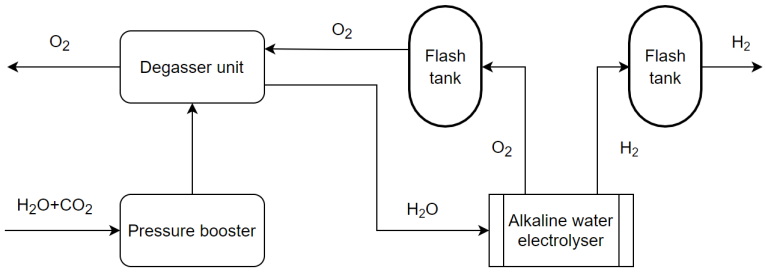

Figure 1.4: Simplified process diagram of the AEC subsystem, consisting of a pressure booster, a degasser unit, two flash tanks and the alkaline water electrolyser.

Water captured from the atmosphere enters the AEC subsystem in the degasser unit, where any residual CO_2 is removed from the water stream. The water is removed with the use of oxygen that is produced by the electrolysis process in the electrolyser. The purified water is pressurized in the pressure booster to a pressure of 50 bar and transported to the alkaline electrolyser. At the electrolyser the electrolysis of the water happens and hydrogen and oxygen are produced at a pressure of 50 bar. The produced gasses are each transported to their own flash tank, where the gasses are separated from the alkaline solution.
The alkaline electrolyser itself is a complex and expensive part of the ZEF micro plant. An overview of the specifications of the ZEF electrolyser are presented in appendix chapter B in table B.1.

The electrolyser consists of a stack of 18 cells, which are compressed and designed to operate under high pressure conditions of 50 bar while remaining leak tight. The configuration of the cells consists of a bipolar zero-gap configuration and uses Zirfon Perl UTP 500 diaphragms [62]. Potassium hydroxide (KOH) is used for the electrolyte. The pressure inside the electrolyser is maintained by a pressure control system that uses liquid level sensors, pressure sensors and purging valves. Instead of using a pump for the re-circulation of the electrolyte, the flow is induced by natural convection. The natural convection is caused by the bubble evolution at the electrodes of the electrolyser cells, and due to the pressure differences that occur inside the electrolyser system.

1.3. Thesis scope.

One of the crucial phenomena that is related to efficient and safe operation of the electrolyser system is the flow inside the AEC subsystem. The flow of the electrolyte is induced by natural convection and follows a certain path from the electrolyser half-cells to the corresponding flash tank and re-circulates back to the half-cells. Possible mixing of electrolyte from the hydrogen side and oxygen side, by back flow or oscillating flow behaviour, will lead to gas crossover, which can lead to explosive mixtures being present in the electrolyser stack. Stagnation and oscillating flow also lead to less efficient operation, which makes optimizing the flow in the electrolyser stack even more important.

The mass flow and flow velocity also determine how efficient the temperature in the system can be regulated. At the moment, there is no regulation of temperature possible in the AEC subsystem. When operating at higher operating current densities, the temperatures in the AEC subsystem can rise significantly, increasing gas crossover and posing a risk to the integrity of the electrolyser cells.

With the above in mind, the scope of the thesis is determined. The main goal of the thesis is to characterise the flow and bubble phenomena inside the ZEF alkaline electrolysis system, with the main focus on the flow phenomena. This to get a better insight in the electrolysis process. In the end a flow characterisation map is made for the flow and bubble phenomena inside the electrolysis system. The characterisation is substantiated by visualization of flow and bubble phenomena in a small scale high pressure alkaline water electrolyser stack. Experiments are conducted on an experimental setup that represents the electrolysis system from the ZEF micro-plant. During the visualization experiments, data is gathered by sensors and an ultrasound Doppler velocimetry device. Experimental data is compared with literature and a previous model, made by I. Daniil [9], that predicts the flow velocity in different elements (pipes, half-cells, flash tanks), the pressure in these elements and estimates the electrolyte level and gas density in the flash tanks . The gathered experimental data will eventually be used to improve the flow in the electrolyser system and implement a temperature regulation system that can keep the temperature on a desired level and can accommodate to sudden temperature difference.

1.3.1. Research questions.

In order to get to the scope of the thesis, research questions are proposed. The last research question is added to investigate the effect of pressure on the bubble behaviour when comparing low and high pressure operation. The purpose of the research question is to gather scientific knowledge. The research questions are shown below:

- **Does the characterisation of the flow and bubble phenomena, by a flow characterisation map, in the electrolysis system impose operational restrictions for the electrolyser stack, regarding efficient and safe operation?**
- **Does the influence of the pressure control system lead to unexpected or undesired flow behaviour inside the electrolysis system?**
- **Can an effective temperature regulation system be modeled and eventually installed for the electrolyser stack, based on the observation and characterisation of the flow inside the electrolysis system?**
- **Does operating at a low pressure and a low current density lead to the same bubble behaviour as operating at a high pressure and a high current density?**

2

Theoretical background study of alkaline water electrolysis.

This chapter will give an insight in the theoretical background of alkaline water electrolysis. Previous literature is consulted, which will contribute to a clear overview of all the relevant elements regarding water electrolysis. The literature study will serve as a reference for understanding and validating certain phenomena that will occur during the experimental research.
The literature study starts with the explanation of the basics of water electrolysis and some in depth geometry. This is followed by the system resistances, thermodynamics and efficiency determination of specifically alkaline water electrolysis. Subsequently important subjects regarding the scope of the thesis, such as gas crossover, bubble influence, flow phenomena and high pressure electrolysis, are discussed. Thereafter the state of the art on high pressure alkaline electrolysis is treated and a small summary of the findings is presented at the end of the theoretical background study.

2.1. Basic principles of water electrolysis.

Electrolysis is an electrochemical process where liquid water molecules are split into hydrogen and oxygen in gas form, as shown in equation 2.1. This process takes place in an electrolysis cell when a certain amount of electrical energy is supplied, which allows the bonds between the water molecules to be broken.

$$H_2O(l) \rightarrow 0.5O_2(g) + H_2(g) \tag{2.1}$$

The main components of a basic water electrolysis unit are the electrodes (the cathode and the anode), an electrolyte and a power supply [71], as shown in figure 2.1. Both electrodes are connected to a power supply and are placed in an ion conducting electrolyte. When a direct current (DC) is applied, electrons start flowing from the power supply to the negative cathode, where the electrons are consumed by hydrogen ions (H^-) to form hydrogen. In order to balance the electrical charge, hydroxide ions (OH^-) are transferred through the electrolyte to the positive anode, where the ions give away electrons and oxygen and water are formed. Both sides of the electrolyser cell are separated by a diaphragm, which prevents mixing of the evolving gasses but allows for ions and water molecules to permeate.

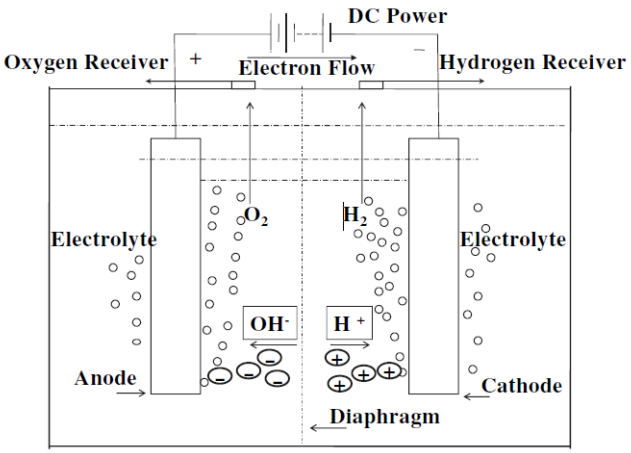

Figure 2.1: Schematic illustration of a basic water electrolysis unit. The main components and the electrochemical process are presented. Figure adapted from Zeng et al. [71]

At the moment, different electrolyte systems are developed for water electrolysis. The three main developed systems are: alkaline water electrolysis (AWE), proton exchange diaphragm electrolysis (PEM) and solid oxide electrolysis (SOE) [7]. From these electrolysis systems, AWE has the most mature technology and offers relatively stable operation and low capital cost. PEM offers high efficiency, a compact design and less gas permeation compared to AWE. Both technologies are already commercialized while SOE is more in developing phase and not widely used yet. In appendix chapter A.9, typical specifications for the different electrolyser systems are compared. In the remaining part of this theoretical study the focus will be on AWE technology, since this is the electrolysis technology used in the ZEF micro-plant.

2.2. Alkaline water electrolysis.

An alkaline water electrolysis system follows the same operation principle as a basic water electrolysis system. The main difference is in the electrolyte that is used for conducting the ions through the cell. For AWE, a strong base is used as the electrolyte. The most common used electrolyte in alkaline water electrolysis is potassium hydroxide (KOH), because its avoids huge corrosion losses [31] and offers a high conductivity [53]. Typically, KOH is used in an aqueous solution with a 20-30 wt% concentration with operating temperatures ranging from 50 to 90°C [71].

Electrode material properties and morphology greatly influence the reaction kinetics that take place in AWE system [8]. The most common electrode material used is nickel, due to its high catalytic activity and availability as well as low cost [33]. The production of hydrogen occurs at negative cathode, while the production of oxygen occurs at the positive anode. The half reaction that occurs on the surface of the anode and the cathode, is shown below in respectively equation 2.2 and equation 2.3.

$$2OH^- \longrightarrow H_2O + 0.5O_2 + 2e^- \tag{2.2}$$

$$2H_2O + 2e^- \longrightarrow H_2 + 2H_2O \tag{2.3}$$

2.3. Electrolyser cell geometry.

The cell configuration of an alkaline water electrolyser consist usually of cells that are assembled in a stack. There are two main stack designs, namely the monopolar and the bipolar stack design [53]. A defining geometrical aspect of alkaline water electrolysers is the gap distance between the electrodes and the diaphragm. Based on the gap distance, an electrolyser can either be defined as a finite gap or a zero gap design electrolyser. The main configurations of an alkaline water electrolyser is treated in more detail in appendix chapter A.2.

2.4. Electrolysis system resistances.

In order to achieve the electrochemical reaction process, a sufficient electrical energy supply is required. The required energy is increased by the electrical resistances in the water electrolyser. These resistances are from the circuit, activation energies necessary for the electrochemical reaction to occur on the electrode surfaces, effective electrode surface area due to partial coverage of gas bubble formation and the ionic transfer resistances within the electrolyte solution [71]. Figure 2.2 shows an electrical circuit analogy of the resistances present in a water electrolysis system.

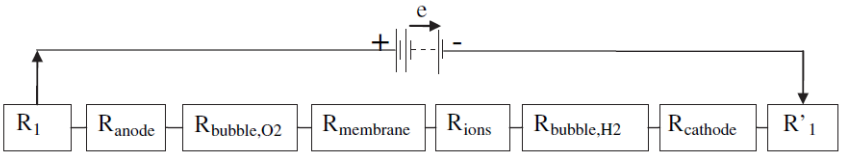

Figure 2.2: Electrical circuit analogy of the resistances present in a water electrolysis system. The resistance $R_{membrane}$ is referred to as R_{dia} in the report. Figure adapted from Zeng et al. [71]

.

The resistance on the left, R_1, is the external electrical circuit resistance at the anode. The resistance includes the wiring and connections to the anode. Resistance R_{anode} originates from the overpotential of the oxygen formation reaction a the anode surface area. $R_{bubble,O2}$ is the resistance due to the partial coverage of the anode surface area by the formed oxygen bubbles. The electrolyte and diaphragm resistances are represented by respectively R_{ions} and R_{dia}. $R_{bubble,H2}$ originates from the partial coverage of the cathode surface area by the the formation of hydrogen bubbles. $R_{cathode}$ is the resistance caused by the overpotential of the hydrogen formation at the cathode surface area and $R_1^{'}$ is the external electrical circuit resistance of the cathode. From the electrical circuit analogy, the total resistance can be expressed by equation 2.4.

$$R_{total} = R_1 + R_{anode} + R_{bubble,O_2} + R_{ions} + R_{dia} + R_{bubble,H_2} + R_{cathode} + R_1^{'} \tag{2.4}$$

The system resistances can be divided into three categories. These are the electrical circuit, the transport and the electrochemical reaction resistances. All resistance categories are treated below.

2.4.1. Circuit resistances.

The electrical circuit resistances at the anode and the cathode come from the wiring and and connections, represented by R_1 and $R_1^{'}$. These resistances can be calculated with the use of Ohm's law. The calculation is presented in equation 2.5.

$$R_1 = \frac{U}{I} \tag{2.5}$$

Here U stand for the applied voltage and I for the applied current. The electrical circuit resistances can also be calculated with the physics equation, shown in equation 2.5.

$$R_1 = \frac{L}{\mathrm{K} \cdot A} \tag{2.6}$$

In the equation L, K and A stand for the length, specific conductivity and cross sectional are of the conductor.

2.4.2. Transport resistances.

The transport related resistances are the physical resistances in the electrolysis process. The gas bubbles covering the electrode surfaces of the electrodes and the presence of the bubbles in the electrolyte solution are an example of the resistances. The resistances to the ionic transfer in the electrolyte and the diaphragm resistance also contribute to the resistance. Altogether do the transport resistances consist of $R_{bubble,O2}$, R_{ions}, R_{dia} and $R_{bubble,H2}$. Resistance to the flow of ions in the electrolyte and resistance to the flow of electrons can be named as ohmic losses.

2.4.3. Electrochemical reaction resistances.

The overpotentials required in order to overcome the activation energies of the hydrogen and oxygen formation reaction are due to the electrochemical resistances. The reaction resistances cause the increase in overall cell potential and are the energy barriers of the reactions, which determine the kinetics of the electrochemical reactions [3]. The reactions resistances are represented by R_{anode} and $R_{cathode}$. When improving the energy efficiency of a water electrolysis process, and the performance of the system, the understanding of these resistances and minimizing them is of utmost importance.

2.5. Electrolysis thermodynamics.

The electrolysis of water requires an energy input for the reaction to occur. The minimum amount of energy is called the equilibrium cell voltage, which can be defined as the potential difference between the anode and cathode [67]. The definition is shown in equation 2.7, where U^0_{anode} stands for the anode potential and $U^0_{cathode}$ stands for the cathode potential.

$$U^0_{cell} = U^0_{anode} - U^0_{cathode} \tag{2.7}$$

The equilibrium cell voltage of an electrochemical cell can also be obtained from the change in Gibbs free energy. The overall Gibbs free energy for standard conditions can be expressed with equation 2.8.

$$\Delta G^0_{cell} = z \cdot F \cdot U^0_{cell}. \tag{2.8}$$

Here z stands for the number of electrons transferred, F is the Faraday constant and $U^0_{cell}$is the standard equilibrium potential for water electrolysis. The driving force for a spontaneous cell reaction is the negative value of the Gibbs free energy change. Which can be written as shown in equation 2.9 [53].

$$\Delta G_{cell} = \Delta H_{cell} - T\Delta S_{cell} \tag{2.9}$$

Where ΔH_{cell} and ΔS_{cell} stand for respectively the enthalpy change and the entropy change for the cell reaction, and T stands for the temperature in Kelvin.

2.5.1. Thermodynamics at standard conditions.

At standard conditions (1 bar, 25 °C) the Gibbs free energy becomes +237.2 kJ mol^{-1} [26], The Gibbs free energy can be used to determine the equilibrium cell voltage, the minimum amount of electrical energy required in order to produce hydrogen, as shown in equation 2.10.

$$U_{rev} = \frac{\Delta G^0_{cell}}{z \cdot F} = \frac{237.2}{2 \cdot 96485} = 1.23\,V \tag{2.10}$$

This value of this cell voltage is 1.23 V and can also be specified as the reversible potential, which is represented by U_{rev} in the equation.

Since the Gibbs free energy has a positive value, the reaction is thermodynamically unfavourable at room temperature and can only occur when heat is consumed. This means the overall reaction is endothermic. The additional amount of energy needed can be supplied in the form of heat from an external heat source or by a sufficient supply of electrical energy, which generates heat inside the electrolyser cell. The potential necessary for the electrolysis to occur with the additional supply of energy is called the thermoneutral potential [46]. The thermoneutral potential can be calculated with equation 2.11 by using the enthalpy change necessary for the reaction, which has a value of +285 kJ mol^{-1}.

$$U_{th} = \frac{\Delta H^0_{cell}}{z \cdot F} = \frac{285}{2 \cdot 96485} = 1.48\,V \tag{2.11}$$

In the equation ΔH^0_{cell} stands for the enthalpy change and U_{th} represents the thermoneutral potential, which at standard conditions has a value of 1.48 V.

2.5.2. Thermodynamics at elevated temperatures.

When operating at higher temperatures than room temperature, the thermodynamic functions, (ΔG, ΔH, ΔS), have to be reconsidered. The pressure and the absolute temperature are the two main variables which help to provide an expression of the thermodynamic functions from which the reversible and thermoneutral potential of the electrolyser can be calculated. To show the effect of temperature on the enthalpy change and the Gibbs energy change, figure 2.3 shows a plot of the enthalpy change and Gibbs energy change, at a constant pressure of 1 bar, as a function of absolute temperature [28]. The relationship between

the electrolyser cell potential and the operating temperature can be expressed as shown in figure 2.4. In the figure the reversible cell voltage and the thermoneutral voltage are plotted against the absolute temperature.

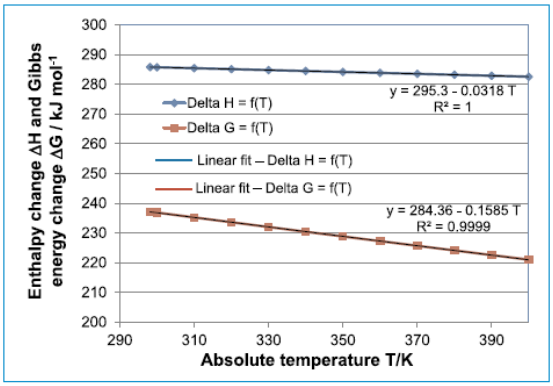

Figure 2.3: Enthalpy change and Gibbs energy change for decomposition of water as function of absolute temperature. Figure adapted from Lamy et al. Figure adapted from Lamy et al.[28].

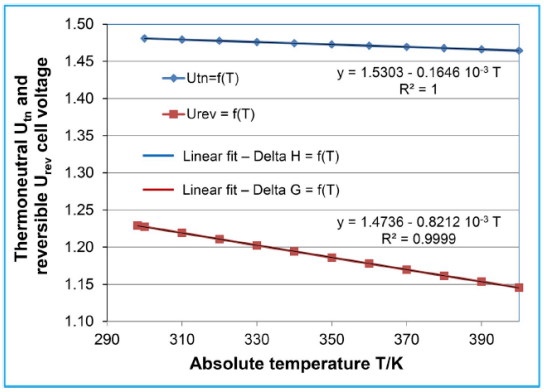

Figure 2.4: Plots of the thermo-neutral voltage and reversible voltage for decomposition of water as a function of absolute temperature. Figure adapted from Lamy et al. [28].

The lines present in figure 2.4 represent the thermoneutral voltage line and the equilibrium voltage line. The latter one is the red line that represents the minimum potential required for the electrolysis of water. Below the line, electrolysis of water is not possible. The thermoneutral voltage blue line represents the actual voltage that must be applied for the electrolysis to be an exothermic reaction. Below the thermoneutral voltage line and above the equilibrium voltage line, the electrolysis of water is an endothermic reaction and requires added heat or electrical energy. The plot clearly shows that at a higher operating temperature the thermoneutral potential change can be neglected when comparing operating under 25 °C, (U_{th}=1.48 V) and 100 °C, (U_{th}=1.47 V). The reversible cell voltage does decrease more significant with a change of 5 % between operating at 25 °C, (U_{rev}=1.23 V), and 100 °C, (U_{rev}=1.17 V).

2.6. Electrode kinetics.

The electrode reaction rate is characterised by the current density. It depends on the nature and on the treatment of the electrode surface [72]. The reaction rate also depends on the electrolyte solution that is in contact with the electrodes. The ions in the electrolyte solution form layers, called double layers , on the electrode surface, which influences the reaction rate. Finally, the reaction rate depends on the the reaction overpotential at the electrode. In the appendix chapter A.3 the electrode kinetics are treated in more detail, with the oxygen and hydrogen evolution steps together with the reaction rate for each step. The Butler-Volmer equation and the Tafel equation will also be briefly discussed.

2.7. Electrolysis efficiency.

The efficiency of electrolysis can be expressed in different ways. Normally, the voltage efficiency can be calculated based of the amount of voltage needed to split the water divided by the total voltage applied to the whole electrolysis cell [6]. Equation 2.12 represents the calculation.

$$\gamma_{voltage} = \frac{U_{anode} - U_{cathode}}{U_{cell}} \cdot 100\% \tag{2.12}$$

Other efficiencies that can be calculated are the Faradic efficiency and the thermal efficiency [71]. For the calculation of the efficiencies, respectively the Gibbs free energy change and the enthalpy change of the electrolysis reaction are used. The Faradic efficiency calculation is shown in equation 2.13 and the thermal efficiency calculation is shown in equation 2.14.

$$\gamma_{Faradic} = \frac{\Delta G}{\Delta G + Losses} \cdot 100\% = \frac{U_{\Delta G}}{U_{cell}} \cdot 100\% \tag{2.13}$$

$$\gamma_{th} = \frac{\Delta H}{\Delta H + Losses} \cdot 100\% = \frac{U_{\Delta H}}{U_{cell}} \cdot 100\% \tag{2.14}$$

In the equations, $U_{\Delta G}$ stands for the equilibrium voltage required for the electrolysis reaction, 1.23 V at standard conditions, and $U_{\Delta H}$ stands for the thermoneutral voltage required for the electrolysis reaction, 1.48 V at standard conditions.

The Faradic efficiency stands for the percentage of the theoretical energy necessary for the electrolysis of water against the cell voltage. The value for the efficiency is always less than 1 because of losses in the cell. The thermal efficiency has an added voltage on top of the reversible voltage in order to maintain the thermal balance. The thermal efficiency can become larger than 1, as the system may absorb heat when operating in endothermic mode, as shown in figure 2.4.

Another way to determine the efficiency of a water electrolysis system is to compare the hydrogen production against the electrical energy applied to the system. This can be done in terms for the hydrogen production rate and for the energy carried by the hydrogen produced [71]. The latter uses the high heating value (HHV) of the hydrogen. Both calculations for the efficiency are shown respectively in equation 2.15 and equation 2.16.

$$\gamma_{H_2 productionrate} = \frac{r_{H_2 productionrate}}{\Delta U} \cdot 100\% = \frac{\dot{V}_{H_2}}{U_{cell} \cdot j \cdot t} \cdot 100\% \tag{2.15}$$

$$\gamma_{H_2 yield} = \frac{U_{HHV}}{\Delta U} \cdot 100\% = \frac{283.8}{U_{cell} \cdot j \cdot t} \cdot 100\% \tag{2.16}$$

where U_{cell} stands for the cell voltage, j for the current applied to the cell and t stands for time. $\dot{V}_{H2}$ represents the hydrogen production rate at unit volume electrolysis cell. The higher heating value of one mole hydrogen is represented by U_{HHV}, with a value of 283.8 kJ

2.7.1. Overpotential.

The overpotential does depend on the temperature and on the current density, as shown in the Bulter-Volmer equation. In figure 2.5 the cell voltage is plotted against the current density.

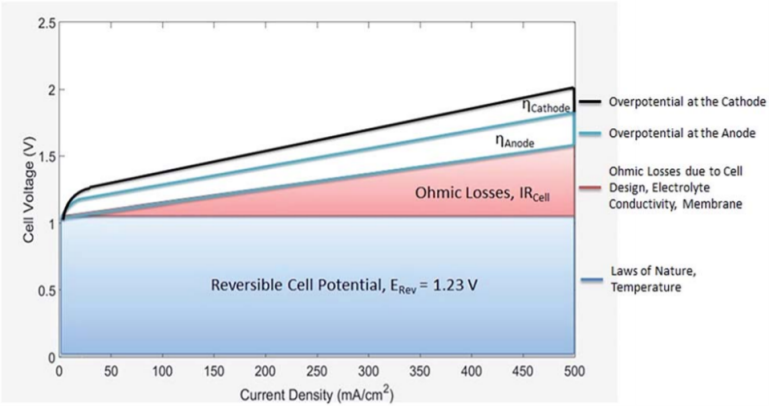

Figure 2.5: Contribution of different losses leading to the overpotential in an electrolyser cell. The Ohmic losses show to become more dominant at increasing current density. Figure adapted from Phillips et al. [43].

From the figure, it becomes clear that at higher current densities the overpotential increases. The overpotential from the hydrogen and oxygen evolution are the main contributing resistances in the electrolyser cell at lower current densities. If the current density increases, the Ohmic losses become more dominant in contributing to the overpotential.

The overpotential can be divided by the current density in order to unify the units of the resistances to the unit Ohm, and compare the energy losses caused by the different resistances [65]. This is illustrated in figure 2.6, where, $E_{loss,\ electrolyte}$, stands for the energy losses due to bubbles in the electrolyte and the ionic transfer resistance. At higher current densities, the coverage of bubbles on the electrode surface shows to be the main contributor to the overpotential with the losses in the electrolyte.

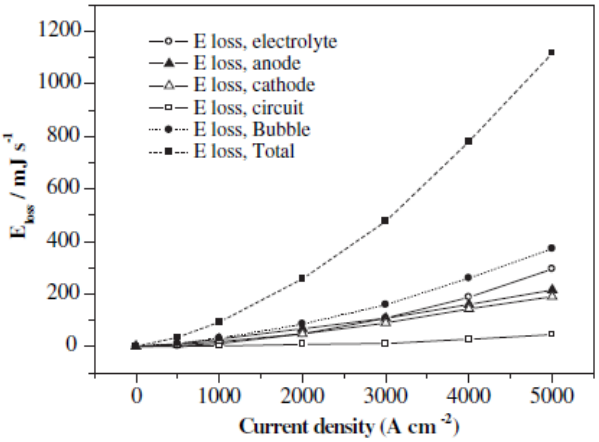

Figure 2.6: A qualitative comparison of energy losses caused by resistances in the system. The losses due to the bubbles in the electrolyser cell show to be the main contributor to the overpotential at increasing currrent density. Figure adapted from Zeng et al. [71]

.

2.8. Gas crossover.

When operating an electrolysis system, it is desired that the produced gasses of hydrogen and oxygen are released with a 100% purity. In reality cross contamination of the two gasses occurs, which is called gas crossover. There are several parameters that affect the gas crossover, such as the operating temperature and pressure, the electrolyte flow, the cell separator properties and the electrolyte cycling strategy.

It is important that the purity of the evolving gasses at the flash tanks is monitored. This to ensure that the gas mixtures stay below the explosive limits [24]. Experiments were conducted to estimate the explosive limits of the hydrogen and oxygen mixtures at different temperatures and pressures [55]. The lower explosion limit (LEL) at atmospheric conditions is 4 mol% hydrogen in the oxygen product flow, whereas the upper explosion limit (UEL) is 4.8 mol% oxygen in the hydrogen product flow. In order to maintain a safe operation, the values for the crossover should stay under 50 % of the LEL and UEL.

Gas crossover can take place in different ways. The produced gasses can crossover in dissolved form, in the electrolyte, through the separator in the electrolyser cell or through the mixing of the electrolyte cycles. Furthermore there are two main physical mechanisms that trigger gas crossover in alkaline electrolysers [59], namely: mass diffusion caused by concentration differences of the dissolved gasses and mass convection due to pressure gradients along the flow and electro-osmosis.

2.8.1. Gas crossover through the diaphragm.

Hydrogen and oxygen are present at each of their respective sides of the diaphragm, either in the gas phase in bubble form or dissolved inside the electrolyte. The diaphragm blocks the mixing of the generated hydrogen and oxygen. Nevertheless, dissolved gasses can permeate through the diaphragm because of its porous structure, inciting crossover. Trinke et al [59] studied this effect and found that the gas permeation is triggered by the concentration difference across the separator, the differential pressure and through electro-osmotic drag. These phenomena are explained in more detail in appendix chapter A.5.

2.8.2. Gas crossover through electrolyte mixing.

The largest contribution to the overall gas crossover is because of the electrolyte mixing [59]. It is important to study and track the flow in the electrolyser, especially at the pressure equalizing pipe. By knowing the velocity profile of the electrolyte in the piping system at different operating conditions, it is possible to predict mass transport of dissolved hydrogen and/or oxygen to the opposite side [9].

2.9. Bubble influence on electrolysis performance.

During the electrolysis process, hydrogen and oxygen bubbles are formed on the surfaces of respectively the anode and the cathode. When the bubbles have grown large enough, they detach from the surface. If the electrodes surface areas is covered with bubbles, the electrical resistance of the whole system is increased. This is because of the reduced contact between the electrode surface and the electrolyte solution, which blocks the electron transfer and increases the Ohmic losses [71]. When bubbles move through the electrolyte, they also decrease the electrical conductivity of the electrolyte, which also leads to an increase in Ohmic losses. The volume occupied by the gas bubbles in the electrolyte is often called the void fraction.

Understanding of the dynamics of bubble behaviour is an important element in order to determine the departure of bubbles from the electrodes. The electrode surface can be treated, to make the surface rougher to increase activation sites for bubbles to grown on [22], or to make the surface more hydrophillic to reduce surface coverage by gas bubbles [70]. Additives can also be added to the electrolyte solution in order to reduce the surface tension of the bubbles, which results in easier detachment from the electrode surface [71]. Mechanically influencing the circulation of the electrolyte is also a means to force bubbles departing from the electrode surface. The detachment of bubbles, depending on the replacement of electrolyte at the electrode interface is known as the wettability [15].

2.9.1. Current density effect.

Experiments were done by Zhang et al. [73] to check the influence on the critical diameter for bubble department on the cell voltage and electrolyte concentration. The critical diameter stands for the average bubble diameter size necessary for a bubble to release from the electrode surface. Experiments were done with a 20 wt% concentration of KOH, at standard conditions. The anode and the cathode used for the experiments were both made from nickel plates. The electrolyte flow was vertical upwards with a velocity between 0 and 1 m/s. The current density was varied to check the effect on the critical diameter of the gas bubbles. The results of the experiments are shown in table 2.1.

Table 2.1: Influence of current density on critical diameter for hydrogen and oxygen bubbles. Data from research done by Zhang et al. [73].

Current density [mA/cm^2]	Cell voltage [V]	Crit diameter hydrogen [mm]	Crit diameter oxygen [mm]
0.3	1.72	0.59	0.60
0.45	1.83	0.88	0.89
0.60	1.88	1.09	1.08
0.75	1.93	1.03	0.96

It was found that an increase in current density lead to an increase in bubble diameter. The increase of the critical diameter for the gas bubbles resulted in a higher cell voltage, which is in line with an increase of the resistance inside the electrolyser cell due to coverage of the electrode surface by the gas bubbles. A higher cell voltage also results in an increased interfacial tension, which ensure gas bubble stick longer to the electrode surface and thus increase in size before detachment. The small decrease in critical diameter of the gas bubbles at higher current density can occur due to the increase of ohmic losses. This results is local heating which cause a temperature gradient on the electrode surface.

2.9.2. KOH concentration effect.

Another set of experiments was done by Zhang et al. [73] to see the effect of different values of KOH concentration on the critical diameter of hydrogen bubbles. The conditions at the experiments were a current density of 0.6 ma cm^{-2} and a temperature of 22 °C . The results from the experiments are shown in table 2.2.

Table 2.2: Influence of KOH concentration on critical diameter for hydrogen bubbles. Data from research done by Zhang et al. [73].

KOH concn, [M]	Cell voltage [V]	Crit diameter hydrogen [mm]
0.5	1.88	1.08
1.0	1.80	0.50
2.0	1.78	0.36
4.0	1.77	0.24

From the table, it becomes clear that the critical diameter for hydrogen bubbles becomes smaller at higher KOH concentrations. The cell voltage also decreased with the increasing KOH concentration. It was suggested that the increase in viscosity of the liquid electrolyte solution resulted in a smaller deviation of the contact angels. This leads to earlier bubble detachment.

2.9.3. Bubble departure from electrode surface.

The conditions for a bubble to depart from the electrode surface were studied by Zhang et al. [73]. The study resulted in the prediction of the critical bubble diameter for departure from the electrode surface area. The formula necessary for the calculation and the results from the study, are explained in further depth in appendix chapter A.4. The main findings where the specification of the forces that act on a bubble while at the electrode surface, as shown in figure 2.7 , and a formula for the critical diameter of gas bubbles. Both findings conclude that increasing electrolyte flow decreases the critical bubble diameter.

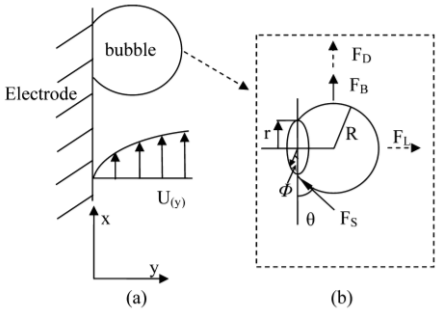

Figure 2.7: (a) Gas bubble on electrode electrode surface with vertical direction of electrolyte flow presented. (b) Forces acting on gas bubble on electrode surface. Forces present are: buoyancy, drag, lift and surface tension force. Figure adapted from Zhang et al. [71].

2.10. Rate of electrolysis reaction.

The amount of oxygen or hydrogen that is produced for a electrolyser cell can be calculated by using the law of Faraday [71]. The molar flow rate for oxygen and hydrogen can be determined with respectively equation 2.17 and equation 2.18.

$$\dot{n}_{O_2} = \frac{\nu_{O_2} \cdot j \cdot A_{cell}}{F \cdot z} = \frac{j \cdot A_{cell}}{F \cdot 4} \tag{2.17}$$

$$\dot{n}_{H_2} = \frac{\nu_{H_2} \cdot j \cdot A_{cell}}{F \cdot z} = \frac{j \cdot A_{cell}}{F \cdot 2} \tag{2.18}$$

Here ν stands for the Stoichiometric coefficient, which has the value 0.5 for the oxygen and 1 for the hydrogen reaction, and A_{cell} stand for the surface area of the respective electrode in the electrolyser cell. In order to determine the volume flow rate, the molar flow rate needs to be multiplied with the molar volume based on the surrounding conditions. The molar volume can be determined with the ideal gas law, as shown in equation 2.19 and used in equation 2.20 and equation 2.21 for respectively oxygen and hydrogen.

$$\frac{V}{n} = v = \frac{R \cdot T}{p} \tag{2.19}$$

$$\dot{V}_{O_2} = v_{O_2} \cdot \dot{n}_{O_2} = \frac{R \cdot T}{p} \cdot \frac{j \cdot A_{cell}}{F \cdot 4} \tag{2.20}$$

$$\dot{V}_{H_2} = v_{H_2} \cdot \dot{n}_{H_2} = \frac{R \cdot T}{p} \cdot \frac{j \cdot A_{cell}}{F \cdot 2} \tag{2.21}$$

In the equations, v stands for the molar volume, R stands for the gas constant and p stands for the pressure in pascal. From the equations above, it becomes clear that the the produced volume of hydrogen and oxygen goes up with increasing temperature and current density, and lowers with increasing pressure. The production rate of hydrogen shows to be twice as high as oxygen under the same conditions, due to the Stoichiometric coefficient.

2.11. Multiphase flow in a channel.

The evolved gasses in the electrolyser cells, under the buoyancy force, will travel to the flash tank. The hydrogen and oxygen will travel in bubble form, and partly dissolved in the electrolyte bulk, through pipe together with the electrolyte in multiphase flow. Multiphase flow through a pipe can be characterised into different types of flow regimes. The most common flow regimes for vertical pipes or tubes are shown in figure 2.8 [68].

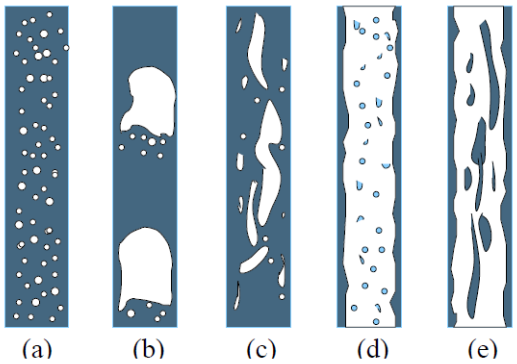

Figure 2.8: Most common multiphase flow regimes in a pipe, (a) bubbly flow, (b) slug flow, (c) churn flow, (d) annular flow, (e) wispy annular flow. Figure adapted from R. Wetind. [68].

Each flow regime presented above and its characteristics is explained in more detail below:

- **Bubbly flow:** Flow with a low rate of coalescence.
- **Slug flow:** Flow with bubbles starting to coalesce and form large elongated bubbles. The bubbles can reach over the width of the channel and are separated by liquid slugs.
- **Churn flow:** Flow with coalesced bubbles which are more elongated than slug flow. The width of the coalesced bubbles is also smaller than the channel width.
- **Annular flow:** Flow with gas travelling in the middle of the channel. The channel wall contains a film of liquid.
- **Wispy annular flow:** Same a annular flow, but with elongated liquid slugs travelling in the middle of the gas flow.

A flow regime can be characterised based on two properties, namely the superficial liquid velocity and the superficial gas velocity. If these two properties are plotted against each other, a flow regime map can be defined. An example of a flow regime map for vertical flow and horizontal flow for a gas/liquid mixture is presented in figure 2.9. The possible flow regimes presented in the flow regime map are visualized in the figure.

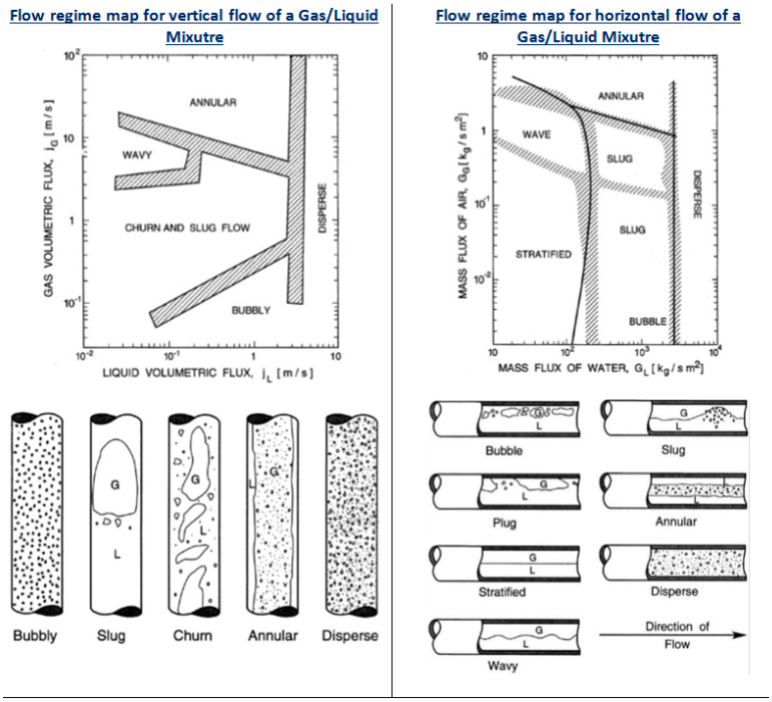

Figure 2.9: The left figure shows a flow regime map for vertical flow of a gas/liquid mixture while the right figure shows a flow regime map for horizontal flow for a gas/liquid mixture. On the x-axis the superficial gas velocity is shown where on the y-axis the superficial liquid velocity is shown. The possible flow regimes occurring on the flow regime map are presented in the figure. Figure adapted from I. Fetoui. [14]

2.12. Electrolysis at high pressure.

Some researchers have asserted that pressurized electrolysis degrades the system efficiency [10]. Research done by Roy et al. [52] shows that electrolysis at elevated pressures leads to an decrease in system efficiency. The reversible cell potential changes at higher pressure and temperature. If it is assumed that the operating pressure is the same in both half cells and there is nog gas leakage across the diaphragm, the simplified Nernst equation can be used to calculate the reversible cell potential [28], as seen in equation 2.22 .

$$\Delta U_{rev} = \Delta U^0_{rev} - \frac{R \cdot T}{z \cdot F} ln \frac{p_{H_2} \cdot p^{0.5}_{O_2}}{p_{H_2O}} \tag{2.22}$$

Here ΔU^0_{rev} is the temperature dependent term for the reversible potential at a pressure of 1 bar, which can be evaluated with equation 2.23 [19]. p_{H2}, p_{O2} and p_{H2O} represent the partial pressures of H_2, O_2 and H_2O respectively.

$$\Delta U^0_{rev}(T) = 1.50342 - 9.956 \cdot 10^{-4} T + 2.5 \cdot 10^{-7} T^{-2} \tag{2.23}$$

From the Nernst equation, it becomes clear that the reversible potential increases at increasing pressure, as can be seen in figure 2.10 from research done by Roy et al. [52].

Reversible voltage at various temperatures and pressures.

Pressure [bar]	Temperature [°C]				
	40	50	60	70	80
1	1.227	1.211	1.195	1.178	1.159
5	1.262	1.248	1.233	1.219	1.204
10	1.275	1.262	1.248	1.234	1.220
20	1.289	1.276	1.262	1.249	1.236
50	1.308	1.295	1.282	1.270	1.257
100	1.322	1.309	1.297	1.285	1.273

Figure 2.10: Reversible potential at various temperature and pressure. Figure adapted from Roy et al. [52].

2.12.1. Bubble influence.

At higher pressures, their is a positive effect on the Ohmic overpotential due to improved bubble kinetics and electrical conductivity. When produced, the generated bubbles cover the electrode surface, which decreases the active area of the electrode and increases the activation overpotential. The active area of the electrode can be determined, based on the bubble coverage of the electrode surface, as shown in equation 2.24, with θ being the bubble coverage. When the operation pressure increases, the coverage of of the bubbles on the electrode decreases, based on the ideal gas law.

$$A_{active} = A_{total} \cdot (1 - \theta) \tag{2.24}$$

At higher pressures the bubble size does decrease, based on the ideal gas law, resulting in smaller heavier bubbles on the electrodes which leads to an increase in the electrical conductivity when the current density is kept constant. With the Bruggeman correlation the increase in electrical conductivity, σ can be calculated [66], as shown in equation 2.25.

$$\frac{\sigma_{KOH-bubble}}{\sigma_{KOH}} = (1 - \epsilon)^{\frac{3}{2}} \tag{2.25}$$

Where ϵ stands for the void fraction. Smaller bubbles moving through the electrolyte result in a lower void fraction, which also increases the conductivity of the electrolyte. The buoyancy force decreases with a smaller bubble diameter, which decreases the rising velocity of the bubbles and so reducing the natural convection flow of the electrolyte.

The higher pressure does however also result in an increased residence time of the bubbles on the electrode, due to a decrease in natural convection by the buoyancy force. The critical diameter of bubbles does increase and with more of the gasses dissolved in the electrolyte at high pressure [59], which influences bubble size as they rise in the electrolyte, might lead to larger bubbles observed in the electrolyte than expected.

2.12.2. High pressure effect on IV curve.

The effect of pressure on the operation of a zero gap alkaline water electrolyser was studied with a numerical model by Jang et al. [23] with almost similar conditions for eventual operation of the ZEF electrolyser. The electrolyser was operated at a current density of 0.6 A/cm^2 for a varying current density range, of 1, 5, 10, 20, 50 and 100 bar, and at a temperature of 70 °C with 30 wt% KOH and Zirfon diaphragms. Figure 2.11 shows the variations in the cell voltage and anode activation, cathode activation and Ohmic activation overpotentials plotted against the pressure.

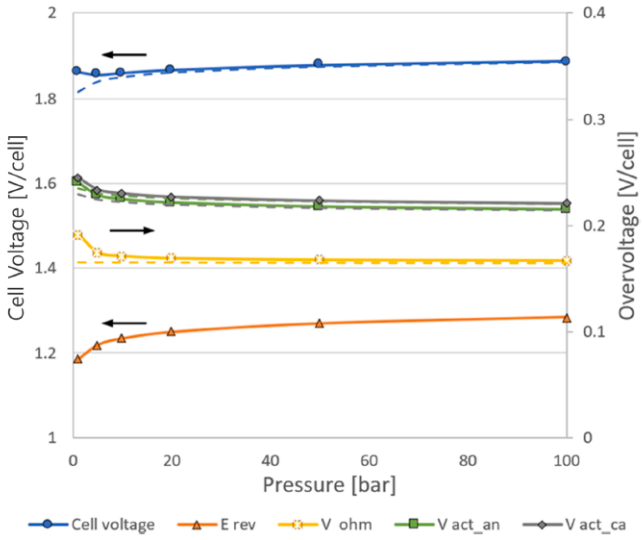

Figure 2.11: Variations in cell voltage and anode activation, cathode activation, and ohmic overvoltages. Simulated for a pressure increasing from 1 to 100 bar, a current density of 0.06 A/cm^2 and a temperature of 70 °C. Figure adapted from Jang et al. [23].

It is visible that the pressure increase results in a decrease in the activation overpotentials and in the Ohmic overpotential. Especially from 1 to 5 bar is the decrease more noticeable before decreasing gradually to a pressure of 100 bar. Although the small bubbles have the disadvantage of to their low buoyancy force, their positive effects shows to be of a greater impact. In the end the lower activation and Ohmic overpotentials seem to be counterbalanced by the increase in reversible cell voltage, resulting in a small variation of cell potential compared to operation at 1 bar.

The effect of current density on the cell voltage was also studied for operating pressures from 1 bar to 100 bar. The results are plotted in an IV curve in figure 2.12.

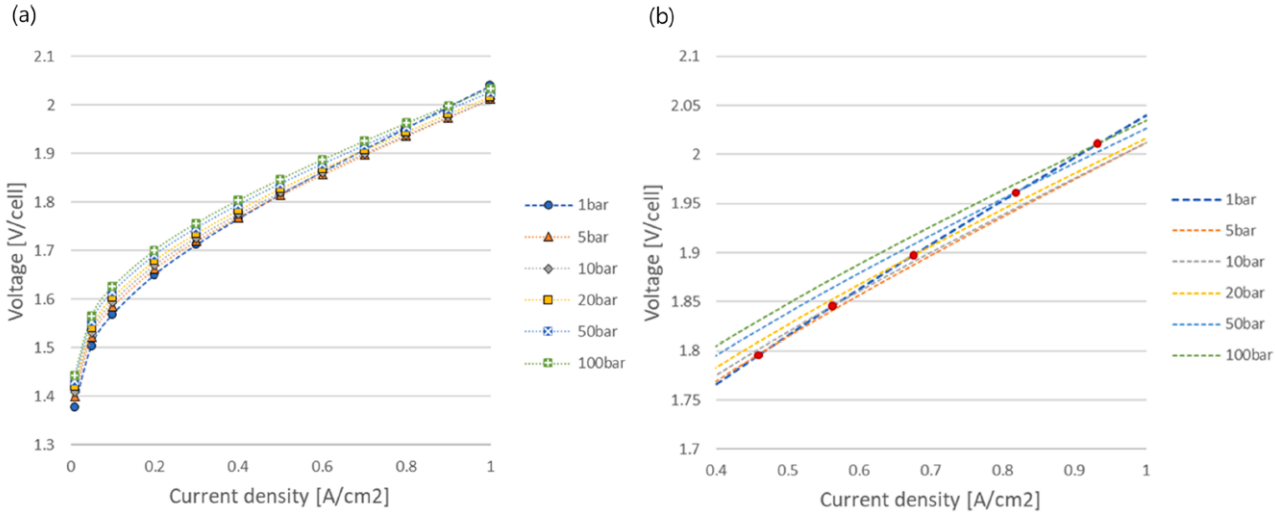

Figure 2.12: (a) Simulated IV curve for various operating pressures, ranging from 1 to 100 bar, for a current density range to 1 A/cm^2. (b) Zoom in of figure 2.12 onto the intersection points of the various pressures. Figures adapted from Jang et al. [23].

The figure shows that the effect of pressure on the increase of the reversible cell voltage is higher in the low current density range. The positive influence of the pressure increase becomes visible at higher current densities, due to the increase of bubble evolution.

2.13. State of the art on high pressure alkaline electrolysis.

2.13.1. Alkaline electrolysis development.

Alkaline electrolyser have a long tradition of being used, and are nowadays available in great number for commercial use. In the recent decades, important development were made for alkaline electrolysis. The most important points of development are presented below [10].

- Zero-gap configuration, reducing the ohmic losses by minimizing the distance between electrodes.
- New diaphragm materials. Previously made of asbestos, the use of inorganic diaphragms were investigated, such as antimony polyacid impregnated with polymers [61] or porous composites composed of a polysulfone matrix and ZrO_2 [62].
- Increase in operating temperature, promoting electrolytic conductivity and improving reaction kinetics at the electrodes.
- Electrocatalytic materials, developed to reduce overpotentials at the electrodes.

There are also certain challenges for alkaline electrolysis [10], which are outlined below:

- Designing a porous electrode design that allows for effective evacuation of bubbles, decreasing Ohmic losses.
- Optimizing porous alloy catalyst with Ni, Fe and Co.
- Preventing hydride formation and hydrogen embrittlement in Ni cathode.
- Reducing the pore diameters of diaphragms for greater purity.

All the development done so far leads to the state of the art for alkaline electrolysis technology, which defines the operating conditions of the AWE such as pressure, temperature and current density together witch specifications as voltage efficiency, operating life and durability. The development and perspective on the technology for alkaline electrolysers, has been researched by Ziems et al. [75]. In table 2.13 the results of the research are presented.

Specification	Symbol	Unit	State of the art	Short-term Development	Middle-term Development
Temperature	ϑ	°C	70–80	80–90	> 90
Pressure	p	bar	30	> 60	> 100
Current density	i	kA/m^2	3–4	6–8	> 10
Cell voltage	U	V	1.9–2.3	1.8–2.1	1.7–2.0
Voltage efficiency	Φ	%	64–78	70–82	74–87
Spec. energy use, sys	Ψ_{sys}	kWh/Nm^3	4.6–6.8	4.5–6.4	4.4–5.9
Part load capacity	θ	%	25	< 15	< 10
Operating life	τ	h	< 90000	> 100000	> 120000
System durability	Π	y	< 25	30	> 30

Figure 2.13: Development perspectives of alkaline electrolysis technology. Figure adapted from Ziems et al. [10].

The state of the art electrolyser operate at a pressure of 30 bar with an operating current density around 3-4 kA/m^2, resulting in an operating temperature between 70 and 80 °C and a cell voltage of 1.9 to 2.3 V. The operating pressure desired by ZEF is higher than the state of the art AWE at the moment, however short-term development should lead to technology which allows for operating at higher pressures. After a longer period of time, AWE are expected which operate a pressures above 100 bar.

2.13.2. Previous work done at ZEF.

Previous research has been done at ZEF for the alkaline water electrolyser. With the use of computation modelling a hydrodynamic force balance and an electrical current network model were developed by M. Geraedts [17]. With the models, the fluid velocity at different points in the AWE and bypass currents could be determined.

K. Sriram [58] did a thermal and flow characterisation for the AWE. The focus of the research was to keep the flow and leaking currents in the electrolyser in check, based on the electrical current network from M. Geraedts and the bubble production. Experiments were conducted with a mock electrolyser setup at atmospheric conditions and altered to simulate high pressure conditions. From the experimental research, recommendation were made to increase the top channel width to keep the leaking currents in check.

The most recent research was done by I. Danill [9], who made a flow model based on a transient hydraulic network analysis. The model can predict the electrolyte flow and pressure response in various elements and locations in the electrolyser. It can predict the level of gas crossover under different operating conditions. The model is used during the experimental analysis of this thesis to validate findings regarding the flow phenomena. Key findings from the model were the oscillatory flow behaviour and a high differential pressure between the stack anodes and cathodes caused by the opening of the purge valves.

2.14. Theoretical background study summary.

Based on the thesis scope, the research questions and the literature study done on previous research, a small summary is made of the most interesting findings that will contribute to characterising and optimizing the AWE design, and will help validating the experimental findings.

- With increasing operating temperature:
  - The efficiency increases, or the overpotential decreases, due to the decrease of Gibbs Free Energy.
  - The gas solubility becomes lower, which has a positive effect on crossover.
  - Increasing temperature has a strong influence on performance, but is limited by degradation issues and material restrictions.
- For an increased current density:
  - The efficiency decreases, due to an increase in overpotential with the ohmic losses as the main contributor due to the increase in bubble generation.
  - The crossover decreases due to less dissolved product gasses.
  - The production rate for hydrogen and oxygen is increased.
- When operating at high pressures:
  - The efficiency slightly decreases, due to an increase in reversible cell voltage.
  - A reduction in bubble size, lowering the void fraction in the electrolyser cell and reducing the ohmic losses.
  - Bubble kinetics improve.
  - More dissolved product gasses in the electrolyte, enhancing crossover through diffusion and convection over the diaphragm.
- Regarding bubble dynamics:
  - Generated bubbles cover the electrode surface area, increasing electric resistance due to less contact between electrode surface and electrolyte.
  - Volume occupied by bubbles, void fraction, decreases the conductivity of the electrolyte.
  - Critical bubble diameter increases with increasing current density.
  - Increase in KOH concentration decreases the critical bubble diameter.
  - The buoyancy force is the main driving force for the upward flow of bubbles for low electrolyte velocities.

3

Experimental setup and equipment.

For the experimental phase, an electrolysis setup from ZEF is used to get to the characterisation and visualisation of the flow and bubble phenomena in the electrolyser stack. The electrolysis setup consists of an alkaline water electrolyser stack and its auxiliary equipment. In this chapter, all the components from the setup, the operation of the setup, the control scheme for pressure regulation, and the methodology behind the experiments is discussed.

3.1. Electrolysis setup.

The electrolysis setup consists of the electrolyser stack and its auxiliary equipment, which are the flash tanks, a hand pump, the system sensors and pressure purge valves. In figure 3.1 an overview of the electrolysis setup is presented. The electrolysis setup is placed in a tank which is called the Bunker Twin. The electrolyser stack is the most important component of the experimental electrolysis setup and is treated first in the section below.

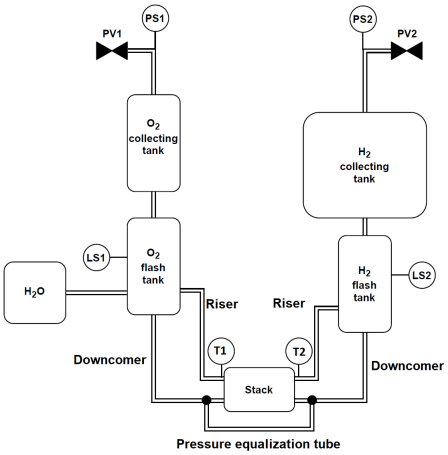

Figure 3.1: Overview of the ZEF experimental electrolysis setup, with the electrolyser stack and auxiliary equipment shown. H_2O stands for the hand pump for supplying water to the system. Sensors in the system are represented by the circles, which are discussed in more detail in chapter 3.2.1. Figure adapted from I. Daniil [9].

3.1.1. Electrolyser stack.

The stack used for the experiments consists of three electrolyser cells. The stack has a bipolar design, explained in more detail in appendix chapter A.2.2, and uses a new design concept: the cookie roll. The cookie roll design consist of several circular discs, comprising two half cells, stacked on top of each other, resembling a cookie roll. The discs have a hole in the middle through which a bolt is inserted to connect all the cells. In appendix chapter B figure B.1(a) an external representation of the electrolyser stack used in the eventual ZEF micro-plant and the cookie roll design are shown, while figure B.1(b) shows a cross sectional view with the half cells visible.

The outer and inner disc material is made of a high performance thermoplastic named polysulfone (PSU), known for its thermal stability at elevated temperatures. PSU can also be used in an alkaline environment due to its high resistance to hydrolysis, combined with a high electric resistivity. The bipolar plate is made of 316 stainless steel and provides structural strength. A visual representation of a single disc is shown in appendix chapter B figure B.2(a) with its important components named and in figure B.2(b) where a cross sectional view of the stack is shown.

A stack bolt is inserted through the bolt holes of the discs. The discs are then compressed against each other, and the bolt tightened with a nut, to form the electrolyser cells. O-rings ensure that the cells remain leak tight during operation. When under

operation, electrolyte enters the stack through channels called footers and eventually the half cells through a square bottom channel. Evolved gas bubbles at the electrode leave the cell at a square top channel. The buoyancy force of the bubbles is the driving force for the electrolyte re-circulation in the electrolysis system by natural convection. The half cells are separated by a Zirfon Perl UTP 500 diaphragm, ensuring one side is the hydrogen side and the other side is the oxygen side. The dimensions of the electrolyser cell and its components are presented in appendix chapter A.6

3.1.2. Electrodes and Zero-gap design.

The ZEF electrolyser cell consists of a zero gap design. Permascand electrodes are placed in each half cell and are connected to the bipolar plate with a current collector made from a 316 stainless steel wave spring. When the discs are assembled, the electrodes compress the Zirfon diaphragm between them. The Zirfon diaphragm has a thickness of 0.5 mm, resulting in a 0.5 mm distance between the electrodes. The gap between the electrodes and the bipolar plate on each side is 4 mm. A picture of one disc inserted with a electrode and current collector is made visible in appendix chapter B in figure B.3. The disc is shown at an angle of 45 degrees in picture B.4.

3.2. Electrolysis setup.

The electrolysis setup is a self-pressurizing system. The pressure is raised by the production of hydrogen and oxygen gas, which also drives the electrolyte re-circulation through the setup. The produced gasses travel under the effect of the buoyancy force towards flash tanks, where they are separated from the liquid electrolyte. The tube leading to the flash tank is called the riser, where the tube from the flash tank to the electrolyser stack is called the downcomer. All the 316 stainless steel tubes in the system are made of Swagelok tubes, with an outer diameter of 6 mm and an inner diameter of 4 mm. On top of the flash tanks are the storage tanks, where the combined volume of flash and storage tank has trice the volume that of the oxygen side. This due to the gas production rate of hydrogen being two times larger than oxygen, as explained in chapter 2.10. A list of the flash and storage tank dimensions is shown in table 3.1.

Table 3.1: Flash and storage tank dimensions of the electrolysis setup.

Component	Diameter	Height	Volume
Oxygen flash tank	35 mm	105 mm	101 cm^3
Hydrogen flash tank	35 mm	137 mm	132 cm^3
Oxygen storage tank	35 mm	105 mm	101 cm^3
Hydrogen storage tank	73 mm	105 mm	439 cm^3

Two pressure purge valves above the storage tanks regulate the pressure inside the setup. The oxygen side and hydrogen side are connected through a pressure equalization tube, which equalizes the pressure on each side of the system. The replenishment of water comes from a manual hand pump on the oxygen side.

3.2.1. System sensors.

The electrolysis setup can regulate the operating pressure in the electrolyser stack with the use of purge valves. There are two purge valves present in the setup: the oxygen purge valve on the oxygen storage tank and the hydrogen purge valve on the hydrogen storage tank. The opening and closing of the valves is determined by the monitoring of the pressure, temperature and electrolyte level in the setup. All the relevant sensors in the setup are presented below:

- PS1: Pressure sensor at the oxygen side.
- PS2: Pressure sensor at the hydrogen side.
- T1: Temperature sensor at the oxygen outflow channel.
- T2: Temperature sensor at the hydrogen outflow channel.
- LS1: Level sensor at the oxygen side.
- LS2: Level sensor at the hydrogen side.

The pressure sensors are placed in the storage tank of both the hydrogen and the oxygen side. The pressure difference measured, is the pressure difference over the diaphragms inside the electrolyser stack. The temperature sensors are placed at the beginning of the outgoing tub of the stack to the flash tanks. Since PSU is a good isolating material (Thermal conductivity of 0.26 W/m K), the temperature in the stack was chosen to be measured by the temperature of the electrolyte flow through the riser tube. The two level sensors measure the height of the electrolyte level in the flash tanks, which lowers when the pressure increases and drops when pressure is relieved from the system.

3.2.2. Pressure control scheme.

With the values from the sensors, the pressure in the system can be regulated with the opening and closing of the purge valves. There are three different stages in the control scheme, which happen when the purge valves are open or closed. The three stages are treated below, with the addition of electrolyte concentration and water management.

1. Pressure purge valves closed:
This stage is active when both the pressure purge valves are closed and the system is under operation. Oxygen and hydrogen are produced at both the electrodes and the pressure is rising. The hydrogen tank is made larger, due to the faster production rate of hydrogen, but the gas pressure level on the oxygen side rises faster. The difference in pressures ensures that the electrolyte is flowing from the oxygen side to the hydrogen side, through the pressure equalization tube. Continuous production of gasses

ensures the electrolyte does not flow backwards to the stack. Because of this effect, the electrolyte level in the oxygen flash tank will drop, and the level sensor becomes dry. This is made visible in figure 3.2.

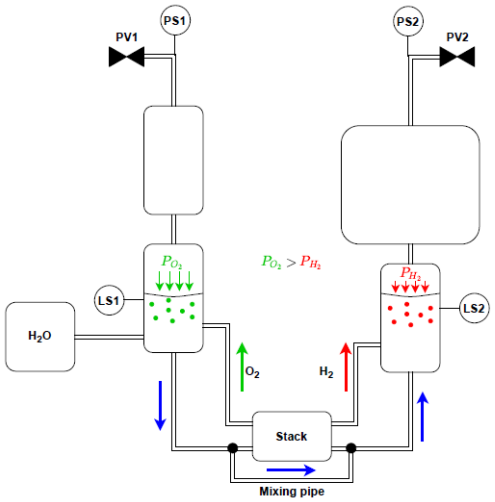

Figure 3.2: Overview of the electrolysis system with the electrolyte flow direction presented when both purge valves are closed. The pressure equalization tube is called the mixing pipe in the figure. Figure adapted from I. Daniil [9].

2. Oxygen purge valve opened:
This stage activates when the oxygen level sensor becomes dry for a fixed period of time. When active, the oxygen purge valve opens for a short amount of time, 100 ms, and oxygen is purged from the oxygen storage tank. The purge of oxygen results in a pressure drop, which leads to the rising of the liquid level in the oxygen flash tank. The electrolyte is transported from the hydrogen side through the equalizing tube to the oxygen side, as shown in figure 3.3(a).

3. Hydrogen purge valve opened:
The third stage happens when the pressure in the hydrogen storage tank exceeds 50 bar. The hydrogen purge valve opens, for 50 ms, and the pressure is relieved from the system, increasing the liquid level in the hydrogen flash tanks. The electrolyte will move to the hydrogen side as shown in figure 3.3(b). This will lower the liquid level in the oxygen flash tank, which will trigger the oxygen purge valve, leveling the liquid levels in the flash tanks. This will results in oscillating behaviour of the electrolyte flow inside the system.

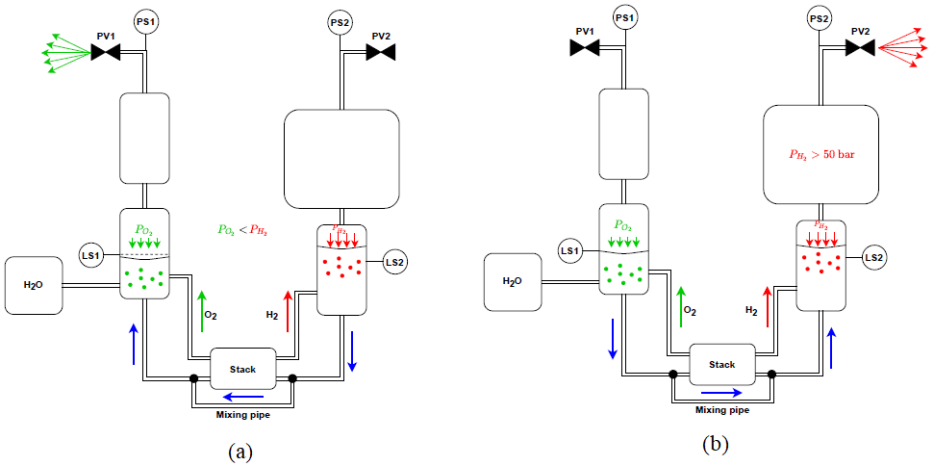

Figure 3.3: (a) Overview of the electrolysis system with the electrolyte flow direction presented when the oxygen purge valve opens. (b) Overview of the electrolysis system with the electrolyte flow direction presented when the hydrogen purge valve opens. Figures adapted from I. Daniil [9].

Electrolyte concentration:
Water consumption at the cathodes will gradually reduce the total amount of water in the system. If the level sensor at the hydrogen side becomes dry, it means water needs to be replenished in order to get the electrolyte concentration back to its original level. This process is done manual at the electrolysis setup, but is automated in the eventual ZEF micro-plant. Since

the electrolyte concentration will fluctuate, even more regarding the manual refilling process, steps were taken to ensure the fluctuations are as little as possible.

When the system is filled with KOH electrolyte for the first time, it is made sure the electrolyte is filled up to the point that both level sensors are wet. Based on the dimensions of the flash tanks, shown in table 3.1, it was chosen to fill the system with electrolyte 3 cm above the level sensors, which relates to 58 cm^3 KOH. When the electrolyte levels drops during operation, the hand pump is used to refill the KOH up to the same level as before operation.

3.3. Visualization setup and equipment.

The characterisation of the bubble and flow phenomena is supported with visual images and video footage shot inside the electrolyser stack. Modifications were made for the electrolyser stack designed by ZEF, in order to get a transparent stack design. Different camera's were used for the visualisation of the bubble and flow phenomena and a ultrasound Doppler velocimetry (UDV) device was used to measure electrolyte velocity in the electrolysis setup. In this chapter, the newly designed transparent stack is treated with the different visualisation equipment and the UDV device.

3.3.1. Transparent electrolyser stack.

The transparent electrolyser stack is a modification of the current electrolyser stack design, explained in detail in chapter 3.1.1. The standard end plate has been removed and is replaced by a transparent add on. This add on consist of a new steel end plate with windows, a polycarbonate (PC) plate, a polymethyl (PMMA) plate and a 136 stainless steel connector plate. Since the PC and PMMA plate do not conduct electricity, the connector plate will serve as the connection to the power supply instead of the new end plate. The new end plates serves to contain the pressure inside the stack, and the windows are used by the camera to look through. The components of the transparent add on and their properties and dimension are presented in table 3.2.

Table 3.2: Components of the transparent add on with their dimensions and properties.

Component	Diameter [mm]	Thickness [mm]	Material	Melting temperature [°C]
End plate	130	20	316 stainless steel	1648
Polycarbonate plate	130	15	Polycarbonate	110
PMMA plate	130	5	Polymethyl	160
Connector plate	130	1	316 stainless steel	1648

The new end plate has two square windows, from 40 cm by 40 cm, on the top and bottom half, which allow to see through the end plate onto the electrode and channels in the electrolyser cell. The transparent PC plate is for structural purposes and provides strength against compression and the pressure from within the stack. The transparent PMMA plate is in contact with the electrolyte and serves as a barrier for the PC plate, because of its resistance against the KOH environment. Since the new end plate has no electrical connection to the the rest of the electrolyser stack, a connector plate is placed between the PMMA plate and the electrolyser cell. The connector plate is connected to the positive side of the power supply. An exploded view of the transparent add on is presented in appendix chapter B figure B.5.

The footage shot with the visualisation equipment can only be done through the two windows in the end plate. The plate is slightly tilted to the left to be able to film the entrance of the top channel and exit of the bottom channel. The view through the two windows in the end plate onto the inside of the electrolyser cell is made visible in appendix chapter B figure B.6.

3.3.2. Camera equipment.

In order to characterise the bubble and flow phenomena inside the electrolyser stack, different camera equipment was used for the visualization. Two types of camera were used: a GoPro Hero Black 8 camera and a digital USB microscope camera. The Gopro camera was used for an overview shot through the top window of the end plate and the microscope camera was used for the zoomed in shots at different interesting points through both the top and the bottom window. The positions that were filmed are shown in chapter 3.5 in figure B.7. The specifications of both cameras and their respective filming positions are treated in detail in the sections below.

Microscope camera:

In order to a better view at the evolution of gas bubbles at the electrodes, a microscope camera was used. The camera was also used to zoom in on the top and bottom channels of the electrolyser cell, to film the bubble flow, slug flow and possible stagnation of the flow or oscillatory flow. A picture of the microscope camera used for the experiments, is shown in figure 3.4.

Figure 3.4: Image of the microscope camera used for experiments.

The main specifications of the camera, that are relevant for the experiments, are shown below in table 3.3. The table shows that the microscope camera has a relative low frame rate. At high electrolyte velocities, it might be difficult to track bubbles with the use of particle image velocimetry [2]. The camera length, combined with the limited space in the Bunker Twin, limits the amount of electrolyser cells that the electrolyser stack can consist of.

Table 3.3: Main specifications of the microscope camera used for the experiments.

Specification	Value
Resolution	640x360p
Frame rate	30 fps
Length	135 mm
Radius	30 mm
Weight	200 g
Video format	AVI

Figure 3.5 shows the camera view on the electrode. The length and width of the holes in the Permascand electrodes were measured by hand to be respectively 3 mm and 1 mm, and are represented by the red line for the length and blue line for the width in figure 3.5. When using the lines as a reference, the window view onto which is zoomed in shows to be 8.5 mm in width and 4 mm in height. With these values, bubble sizes seen in the footage can be determined.

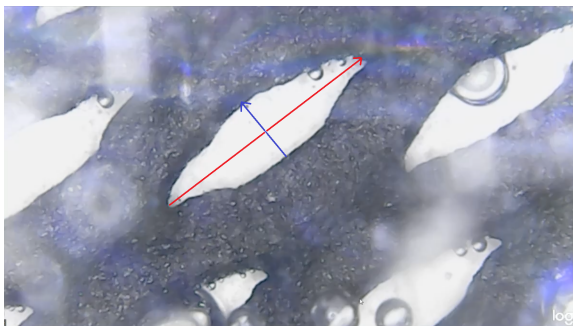

Figure 3.5: Microscope camera view on the Permascand electrode. The red and blue arrow are used as a reference for determining the bubble size in a later stadium. The red arrow has a length of 3 mm while the blue arrow has a length of 1 mm.

GoPro Hero Black 8:

The GoPro Hero black 8 was used during the experiments to get an overview through the windows in the end plate. While the microscope camera is mainly used for the characterisation of the flow and bubble phenomena in the stack, the GoPro is used to provide additional footage to support certain findings from the experimental data and microscope camera footage.

The GoPro footage was shot mainly through the top window, where the top half of the electrode, and the current collector, and the top channel were visible. Possible coalescence of bubbles at the ceiling and stagnation at the entrance of the top channel can be made visual with this view. In figure 3.6 the GoPro overview to the top window is presented with it's main specifications presented in table 3.4.

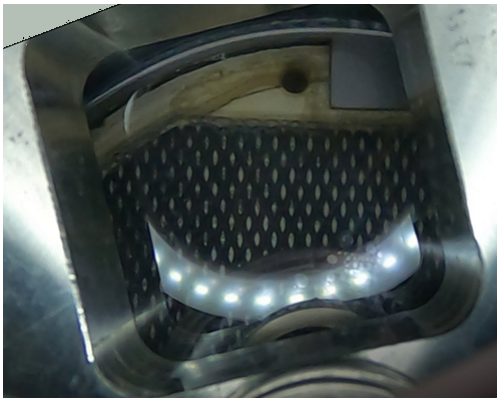

Figure 3.6: GoPro Hero Black 8 overview through the top window in the end plate, onto the top of the electrode and the top channel of the electrolyser cell. The reflection of the lighting in the Bunker Twin is visible in the figure as a the white semicircle.

Table 3.4: Main specifications of the GoPro Hero Black 8 camera, used for the experiments.

Specification	Value
Resolution	1080x780p
Frame rate	120 fps
Length	28.4 mm
Height	48.6 mm
Width	66.3 mm
Weight	200 g
Video format	MP4

3.4. Ultrasound Doppler velocimetry device.

In order to measure the velocity in certain components of the electrolysis system, an ultrasound Doppler velocimetry, (UDV), device was used. This device uses the pulsed ultrasound Doppler method to measure the velocity of small particles or bubbles within a moving fluid. With UDV, the velocities are derived from shifts in positions between pulses with the Doppler effect playing a minor role [13]. The working principle of the UDV is explained in appendix chapter A.8 in more detail.

3.5. Methodology.

In this chapter, the methodology behind the experiments is treated. The goal of the experiments is to characterise the bubble and flow phenomena inside the electrolyser stack in order to answer the research questions proposed in chapter 1.3.1. Data is gathered during experiments with the camera equipment, explained in chapter 3.3.2, and from the sensors present in the electrolysis system, as explained in chapter 3.2.1. The data is used to support the findings from the visualisation of the bubble and flow phenomena. In the end, a flow characterisation map is defined based on the operating current density and pressure, which will present different bubble and flow phenomena inside the electrolysis system. Relevant subjects are different flow regimes in the electrolyser channel, possible stagnation of the flow, oscillating flow and back flow and determining of bubble size and behaviour. For the experiments a 3 cell electrolyser stack is used, due to the length of the microscope camera and the limited space in the Bunker Twin. Unfortunately only one side of the electrolyser cell can be filmed during the experiments. The oxygen side, anode, of the farthest electrolyser cell is visualized during the experiments.

3.5.1. Characterisation of operation of the electrolyser stack.

The first set of experiments is conducted to characterise the operation of the electrolyser at different pressures and current densities. The current density range is set at 0.017 to 0.4 A/cm^2. This range is chosen based on the desired operating current density of the ZEF electrolyser stack and on current density values used in current electrolyser setups. The first experiment is to characterise the pressure build up of the system from 1 bar to 50 bar. Relevant data from the sensors and power supply, such a voltage, temperature and electrolyte levels, is gathered to validate future findings. Experiments were conducted to characterise the operation at low pressure, in a range of 1-3 bar, and at high pressure, in a range of 47-50 bar. These operations will be compared to see the effect of operating pressure.

3.5.2. Characterisation of bubble and flow phenomena.

The bubble and flow phenomena inside the electrolyser cell are characterised with the use of the visualisation equipment: the microscope camera and the GoPro camera. Video footage is shot at different positions in the electrolyser cell. The different filming positions are presented in appendix chapter B in figure B.7.

Each filming position is treated individually below :

1. **Top half overview**: This position is used to get an overview of the top half of the electrolyser cell, which consists of the top side of the electrode and the top channel with its entrance. The position is filmed with the GoPro camera. Due to the microscope zooming in on a specific position, an overview of the surroundings can give extra insight by linking the microscope filming positions.

2. **Top channel**: The top channel position allows to visualize the different flow regimes that occur when the generated bubbles and electrolyte flow through the top channel to the riser and eventually to the flash tank. Possible back flow or oscillating flow could also be observed.
3. **Entrance top channel:** The entrance effects that take place at the top channel are an important part to visualize. The generated bubbles have to flow into the small channel and coalescence of bubbles could possibly lead to stagnation of the flow through the top channel. The bubbles at the top of the electrolyser have the largest diameter in size, after coalescing or growing when flowing upwards due to dissolved gasses in the electrolyte, and validating this assumption would be interesting.
4. **Top of electrode + ceiling:** This positions allows for the opportunity to film the bubble diameter at the top at the electrode. Possible bubble growth due to travelling upwards in the electrolyte, with dissolved gasses, could be seen. The effect of the small incline of the ceiling on the transport of bubbles to the top channel can be inspected.
5. **Bottom of electrode:** This position allows to characterize the generated bubbles at the bottom of the bubble curtain, where the electrode flow is the lowest. The bottom of the bubble curtain also contains the least amount of bubbles, which results in easier characterisation of individual bubbles. The comparison with bubbles filmed at the top of the electrode is especially interesting. The effect of electrolyte circulation on the critical diameter of the bubbles is taken out by filming at the bottom furthest away from the bottom channel.
6. **Bottom channel:** The bottom channel should only re-circulate electrolyte back into the electrolyser cell. Possible re-circulation of bubbles, which has a negative effect on gas crossover, could be seen. Back flow during operation could also be observed.

During the experiments, each position is filmed for varying current densities and pressure levels. The focus is on the videos shot at high pressure levels at 47-50 bar, equal to the operating level of the ZEF electrolyser stack. The current density is varied between 0.017 and 0.4 A/cm^2. For scientific purposes, the experiments at high pressure are compared with experiments at low pressures, 1-3 bar, for the same range of current densities. In order to be able to compare the data and videos from the experiments, temperature management is of utmost importance. Temperature management at high current densities should be difficult due to the lack of a temperature regulation system. By increasing or decreasing the current density, the temperature value should be able to be regulated to some extend.

3.5.3. Characterisation of electrolyte flow in the electrolysis system.

The electrolyte flow in the electrolysis system is driven by natural convection due to the generation of gas bubbles at the electrodes. As explained in section 3.2 does opening the purge valves affect the flow direction and velocity. Validation of this effect and the measurement of electrolyte velocity in the tubes of the electrolysis system can be done with the UDV device. Possible stagnation or back flow of the electrolyte can also be monitored. The UDV transmitter is placed against a 316 stainless steel tube in the electrolysis system. In order to get a fixed position for the transmitter at a small angle, it is placed in between two plates. The plates also ensure the viscous gel will not flow of the tube if it becomes less viscous at higher temperatures. The gathered data from the experiments is used to support the findings from the video footage of the microscope camera and the GoPro camera and to validate the findings from the model from I. Daniil [9].

4

Experimental results and analysis.

In this chapter, the findings and observations from the experimental research are presented and discussed. A first set of experiments was conducted to characterise the operation of the electrolyser stack. The build up of pressure to 50 bar was monitored and operation at low pressure and at high pressure was researched. Visualisation of flow and bubble phenomena on the oxygen side of an electrolyser cell was performed for varying current densities and pressure levels for various positions in the electrolyser cell. The UDV device was used to measure the electrolyte velocity in the electrolysis system for the riser and the downcomer tube. Based on the gathered data, calculations were made for occurrence of flow stagnation, gas crossover and flow directions in the electrolysis system. A temperature regulation system is modelled and checked for implementation in the experimental setup and in the eventual ZEF electrolysis system. At the end of the chapter a flow characterisation map is made, based on the findings and observations during the experimental research and on the calculations made.

4.1. Characterisation of operation of the electrolyser stack.

The characterisation of operation of the electrolyser stack has been done with the main focus on operating at high pressures in a range of 47-50 bar. Experiments were also conducted at low pressures and during the build up of pressure up to 50 bar. First a standard operating current density was determined, which was applied in future experiments when building up the pressure to 50 bar.

4.1.1. Determining standard operating current density.

The applied current density determines the amount of hydrogen and oxygen generated at respectively the cathode and the anode, as explained in chapter 2.10. In order to conduct the experiments as efficient as possible a quick pressure build up to 50 bar is desired, while keeping the temperature inside the stack at a safe level. Based on the good insulation properties of PSU and on the fact that the temperature is measured outside the stack, which gives a slightly less accurate reading than inside the electrolyser stack, temperatures were determined to stay below a temperature reading of 60 °C during the experiments. Earlier experiments with a previous design of the electrolyser stack resulted in material failure when the operating temperature reading rose above 70 °C.
A first experiment was conducted to determine the desired current density for the pressure build up, while keeping the temperature below the 60 °C. The operating current density was set at 0.3 A/cm^2. During the experiment, the pressure in the electrolysis system raised to 34 bar after 2300 seconds, visible in figure 4.1. The small pressure drops come from the opening of the oxygen purge valve, made visible with the blue circles in the graph. The temperature level on the oxygen side in the stack rose to 57 °C during the build up of pressure to 34 bar, presented in figure 4.2 Since the temperature kept rising, the experiment was halted and a lower current density value chosen for the pressure build. Eventually 0.2 A/cm^2 was chosen as the standard operating current density for increasing the pressure to 50 bar, due to the temperature rising to a maximum of 49 °C. This can be seen in temperature plot of future experiments in this chapter. The 0.2 A/cm^2 allows for a safe operation by keeping the temperature in check.

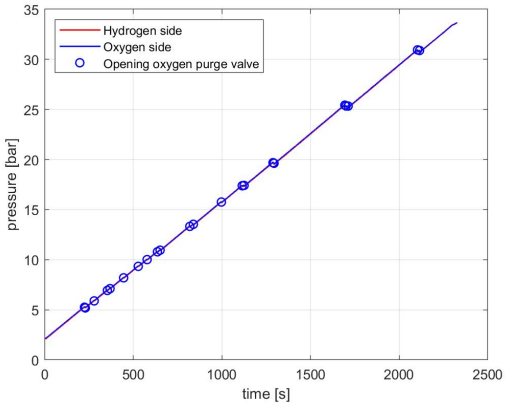

Figure 4.1: Pressure increase over time when operating at a current density of 0.3 A/cm^2. The small pressure drops in the graph come from the opening of the oxygen purge valve in order to level the electrolyte level in the flash tanks, made visible by the blue circles.

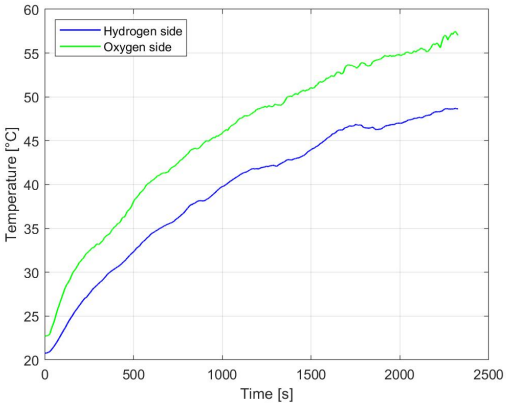

Figure 4.2: Temperature measurements for the oxygen and hydrogen side during pressure build up of the electrolyser stack. The temperature is measured at the riser tube of oxygen and hydrogen side. The temperature difference comes due to worse insulation of the hydrogen temperature sensor.

From the temperature plot in figure 4.2 it is seen that the temperature measured for the hydrogen side is significantly lower than on the oxygen side. It is expected that the temperatures on each side of the electrolyser cells are roughly equal. Due to the earlier mentioned issue with insulation of the temperature sensors, on the outgoing Swagelok tubes of the electrolyser stack, this difference in measured temperature is caused. From now on, the temperature measured on the oxygen outgoing Swagelok tube is considered as the temperature in the electrolyser stack.

4.1.2. Pressure build up to 50 bar.

Multiple experiments have been conducted on the pressure build up to 50 bar for a current density of 0.2 A/cm^2. The starting conditions where a pressure slightly above 2 bar and a temperature around 23 °C. The varying starting pressure and starting temperature for different experiments, come due to the necessity of wetting both level sensors before the start-up. The plots shown in this chapter, present the results from an experiment where the pressure is build up to 50 bar with starting conditions of 5 bar and temperature of 30 °C. This specific experiment was chosen due to most representative data based on all the other experiments. The values presented in the tables in this section show the average values taken over the multiple experiments.

Operating pressure.

The pressure plot of the electrolyser stack for operating at 0.2 A/cm^2 is made visible in figure 4.3. The opening of the hydrogen and oxygen purge valves is also represented in the figure. The blue circles stand for the opening of the oxygen purge valve and the red circle for the hydrogen purge valve.

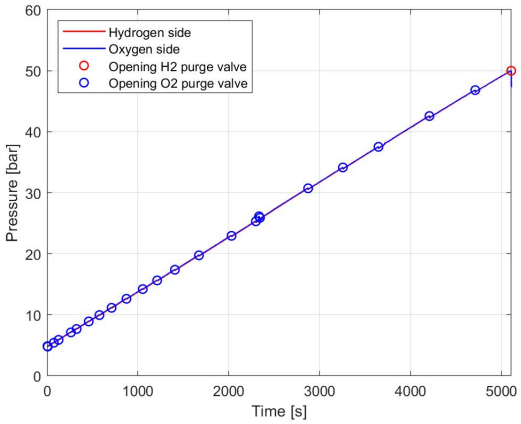

Figure 4.3: Pressure increase from 5 to 50 bar, during operation at 0.2 A/cm^2. The opening of the oxygen and hydrogen purge valve is visualized by respectively the blue and red circles. The cluster of opening of the oxygen purge valve after 2320 seconds, at a pressure of 25 bar, comes from the manual supplying of water to the electrolysis system by the hand pump, increasing the electrolyte level in the oxygen flash tank. The interval between the opening of the oxygen purge valve, due to measured electrolyte level in the oxygen flash tank, increases with increasing pressure.

The plot shows a constant increase in pressure up to 50 bar. Based on all the experiments, the average time for the pressure increase to 50 bar from a starting pressure of 2 bar showed to be 5501 s, roughly 1 hour and 31 minutes. The opening of the

oxygen purge valve, to level the electrolyte level in the system, happens more frequently at the start of the pressure build up. The time in between each purge increase for longer operation time and a higher pressure.
After 2320 seconds and reaching a pressure of 25 bar, the hydrogen level sensor became dry after an oxygen purge, and the system had to be refilled. This lead to a pressure increase, followed by two consecutive oxygen purges.
For convenience, all the relevant data gathered from the experiments for the pressure build up, is presented in table 4.1 in the chapter below.

Operating temperature.
The temperature increase for both the hydrogen and oxygen electrolyte flow goes at the same rate, except the hydrogen temperature remains lower according to the temperature sensors, due to better insulation of the oxygen temperature sensor. The temperature increase during pressure build up is presented in figure 4.4.

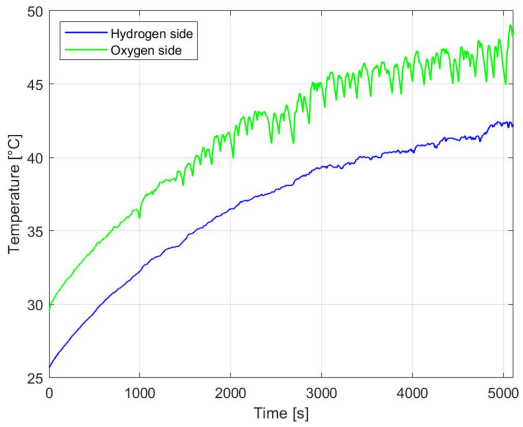

Figure 4.4: Temperature increase for the oxygen and the hydrogen side during build up of pressure to 50 bar at a current density of 0.2 A/cm^2. Fluctuation in the temperature measurement of the oxygen side starts occurring frequently after 1500 seconds, at a pressure of 18.5 bar. Fluctuations for the temperature measurement on the hydrogen side starts fluctuating after 2000 seconds at a pressure of 23 bar, however these fluctuation remain small. As explained earlier comes the temperature difference from the worse insulation of the hydrogen temperature sensor.

An important observation is the fluctuation in the temperature reading for the oxygen side, starting after the after the pressure reaches 15 bar. For pressures above 20 bar the fluctuation of temperature occurs on a frequent base and the temperature difference between peaks increases with increasing pressure. The hydrogen side temperature reading also shows signs of fluctuation in temperature but these fluctuations are small and stay withing a 0.3 °C range. Since the temperature is measured at the outgoing electrolyte flow of the electrolyser stack, the assumption is made that the fluctuations come from stagnation of the electrolyte re-circulation, or stagnation of the flow, on the oxygen side of the electrolyser stack. From now on,the moment the re-circulation of the electrolyte stops, or the flow through through the channels to the flash tank is halted, is referred to as flow stagnation. The period in between the occurrence of flow stagnation will be referred to as a stagnation cycle. The finding of possible flow stagnation is compared with video footage from the microscope camera and GoPro camera at the top channel in the electrolyser cell. This is done later in chapter 4.3.1. An overview of the relevant data gathered from the temperature plots of the pressure build up is presented in table 4.1.

Table 4.1: Relevant data gathered from the pressure and temperature sensors for the pressure build up to 50 bar.

Specification	Value
Average time for reaching 50 bar	5501 s
Average temperature when reaching 50 bar	47 °C
Average starting pressure for flow stagnation oxygen side	18.5 bar
Average starting pressure for flow stagnation hydrogen side	23 bar

It must be noted that during the first set of experiments this behaviour of fluctuation did not occur, as can be seen in figure 4.2 in chapter 4.1.1. During the first set of experiments, a small leak occurred in a manual purge valve on top of the hydrogen storage tank, which was not noticed until a few experiments later. All the experiments treated further in the thesis report were done without leakage in the system, except when mentioned. The behaviour of the small leak on the hydrogen side is treated in more detail in chapter 4.9.

Electrolyser cell voltage.
The voltage for one electrolyser cell during pressure build up is presented in figure 4.5. The cell voltage decreased during the build up of pressure to 50 bar. As explained in chapter 2.5.2 does the cell voltage decrease for increasing temperature, which results in an increasing efficiency. The measured cell voltage started at a value of 2.80 V and showed to be decreasing till a value of 2.38 V when reaching 50 bar.

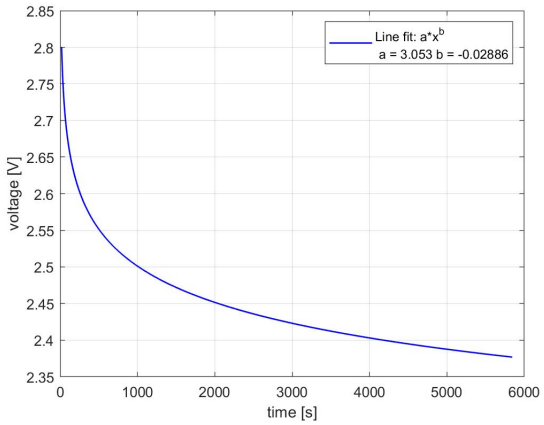

Figure 4.5: Cell voltage during build up of pressure at 0.2 A/cm^2. The voltage drops over time due to the increase in temperature.

4.1.3. Operation at 50 bar.

Operating pressure.

When a pressure of 50 bar is reached in the electrolyser stack, the hydrogen purge valve opens to relief the pressure from the system. This results in a pressure drop, followed by the opening of the oxygen purge valve in order to equalize the electrolyte level in both the flash tanks. Operating at 50 bar is a continuation of these events. Figure 4.6 presents the change in pressure for operating up to 50 bar, for a current density of 0.2 A/cm^2. The moment the purge valve are opened, are visible in the plot with a red and blue circle for respectively hydrogen and oxygen.

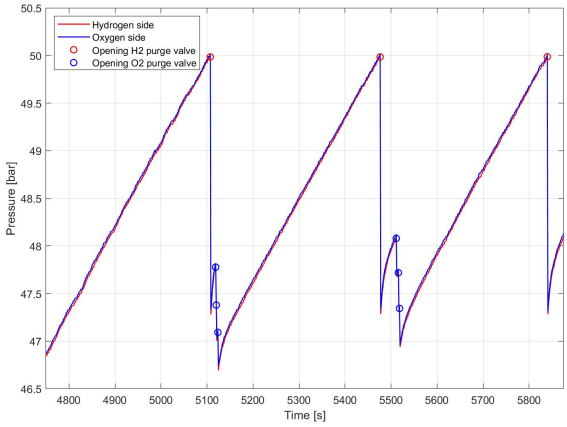

Figure 4.6: Pressure increase during three hydrogen purge cycles at 0.2 A/cm^2 and an average temperature of 47.5 °C. The opening of the oxygen and hydrogen purge valves opening is visualized by the blue and red circles respectively. The pressure drop when the hydrogen purge valve is opened shows to be 2.7 and the opening of the oxygen purge valve leads to an average pressure drop of 0.4 bar.

Three hydrogen purge cycles are visible in the plot, which each take approximately 364 s. When the hydrogen purge valve opens, for 50 ms, the pressure drops 2.7 bar. When the level sensor in the oxygen flash tank measures the decline in electrolyte level the oxygen purge valve opens for 100 ms, three times in a row, to balance the electrolyte level in the system and leading to a pressure reduction of 0.4 bar in the system. After the opening of the purge valves, the pressure builds up again to a pressure of 50 bar. All the important data from the pressure plot is presented in table 4.2

Table 4.2: Relevant data gathered from the pressure sensors for operating at a pressure of 47-50 bar and an average temperature of 47.5 °C.

Specification	Value
Pressure operating range	47-50 bar
Average time between hydrogen purge cycle	364 s
Pressure drop hydrogen purge valve	2.7 bar
Pressure drop oxygen purge valve	0.4 bar
Average pressure build up time between hydrogen purge cycles	337 s

The effect of the opening of the purge valves when the system reaches 50 bar, has been modelled by I. Daniil [9]. The models shows a difference in pressure drop for the oxygen flash tank and the hydrogen flash tank, which is shown in figure 4.7.

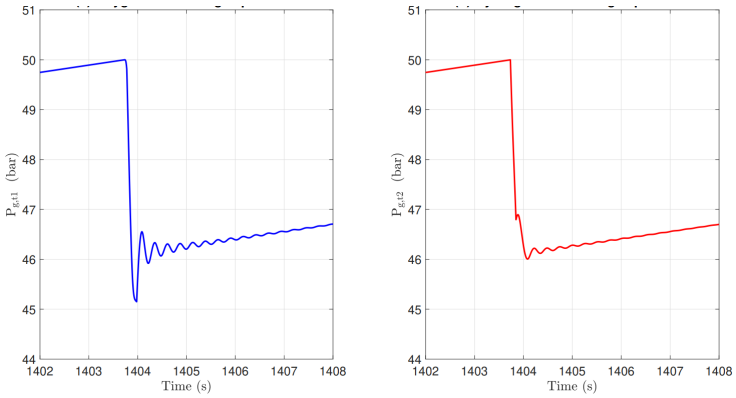

Figure 4.7: Simulated pressure drop and oscillatory behaviour of pressure caused by simultaneous opening of the pressure purge valves for respectively the oxygen flash tank (a) and the hydrogen flash tank (b). Simulation done by I. Daniil. [9].

The pressure on the oxygen side drops to a pressure of 45.2 bar after opening of both valves, while the hydrogen side drops to a pressure of 46 bar. Compared to the experimental data, are the pressure drops due to the opening of the valves higher and differ for the oxygen and hydrogen side. There is also an oscillatory behaviour visible in the plot which is not seen in the experimental data. It must be said that the model opens both of the purge valves simultaneously and that with the experiments three oxygen purges were necessary to level the electrolyte level in the system. The pressure sensors were also not modelled to measure the pressure at a high frequency so the oscillatory behaviour cannot be validated with the pressure sensor data.

Operating temperature.
The temperature readings for the hydrogen side and the oxygen side are presented in figure 4.8. As explained before, in chapter 4.1.2, does the hydrogen electrolyte temperature appear to be lower compared to the oxygen electrolyte due to worse insulation.

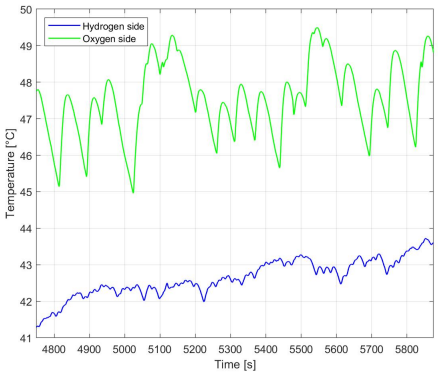

Figure 4.8: Temperature plot inside the electrolyser stack for oxygen and hydrogen while operating at 47-50 bar and 0.2 A/cm^2.The fluctuation for the oxygen side temperature sensor reading is clearly visible. Fluctuations in temperature reading on the hydrogen side are a lot smaller.

The temperature plot shows that for operating at a pressure range of 47-50 bar, temperature sensor readings result between 45 and 50 °C. The effect of operating at a high pressure on the temperature fluctuations is clearly visible for the oxygen side. The temperature fluctuations on the hydrogen side stay relatively small at high pressures.

An assumption is made that the temperature fluctuation are caused by stagnation of the re-circulation of the electrolyte flow. The flow stagnation causes the Swagelok tube, to which the temperature sensor is connected, to cool down. This effect is studied into further depth with the visualisation experiments done in chapter 4.3. Table 4.3 shows all the relevant information taken from the temperature plot at high pressure.

Table 4.3: Relevant data gathered from the temperature sensors for operating at a pressure of 47 to 50 bar and a current density of 0.2 A/cm^2

Specification	Value
Operating temperature range electrolyser stack	45-50 °C
Average time between temperature peaks	70 s
Average temperature increase with electrolyte flow oxygen side	2 °C

Cell voltage.

The voltage over the electrolyser stack depends on the resistances in the system. During operation at 47-50 bar, and an average temperature of 47 °C, the voltage over the electrolyser showed to be 2.26 V when operating at a current density of 0.2 A/cm^2.

4.2. Comparison of low and high pressure operation.

After the experiments for the characterisation of operation of the electrolyser stack were done, a new set of experiments was conducted at low pressure and at high pressure. The experiments were focused on the comparison for low and high operating pressure for a varying current density. For a low operating pressure of 1.8-3 bar and a high operating pressure of 47-50 bar, the current density was varied between 0.017 and 0.4 A/cm^2 for different temperatures.

4.2.1. High and low pressure IV curve.

During the experiments, the current density was varied while trying to keep the temperature level constant in the electrolyser stack. Due to the lack of a temperature regulation system, the temperature was regulated by alternating the current density, which proved to be a difficult task. Keeping the pressure constant also proved to be difficult, especially at high pressures, due to the pressure drop occurring when opening the purge valves. A problem occurring at low pressure was the fast increase in pressure at the higher side of the current density range.

After the experiments, the most reliable data was gathered at a high pressure of 49 bar for four different temperature values, namely 41 °C, 47 °C, 50°C and 55°C. The reliable data gathered for low pressure operation was taken at a pressure range of 1.9 to 2.1 bar. Multiple data was gathered for each value of the current density range and averaged into 2 bar data for temperature values of 22 °C, 35 °C and 41 °C.

The electrolyser cell voltage was plotted against the corresponding current density for the low pressure and high pressure operation, and a curve fit was used to obtain the IV curves. Rahim et al. [45] proposed a curve fit for obtaining the electrolyser cell voltage for an alkaline water electrolyser, as a function of the current density and the temperature in Kelvin. The function for the curve fit is shown in equation 4.1.

$$U = U_{rev} + a \cdot log\left(\frac{b + \frac{c}{T} + \frac{d}{T^2}j + 1}{e}\right) + \left(\frac{f + g \cdot T}{e}\right)j \tag{4.1}$$

A curve fitting application from Matlab was used to apply the curve to the data from the experiments, in order to determine the constants for the function. Figure 4.9 shows a 3D plot from the curve fitting application based on the curve fit from equation 4.1 and the experimental data at a high pressure. The data point are all lying just above or below the surface area of the curve fits. The constants used in the curve fit are presented in table 4.4.

Table 4.4: Curve fitting constants corresponding with the plot in figure 4.9

Curve fit constant	U_{rev}	a	b	c	d	e	f	g
Value	1.23	0.0816	4.545	4.675	12.1	0.0018	0.02434	-6.337e-05

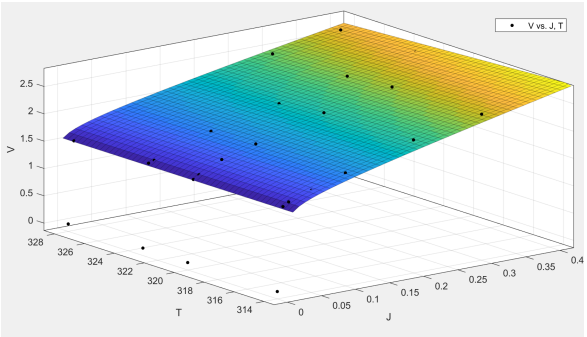

Figure 4.9: (curve fit

If the curve fit is applied in the plots for the electrolyser cell voltage and the corresponding current density and temperature value, figure 4.10 en figure 4.11 can be consulted for respectively low pressure operation at 2 bar and high pressure operation at 49 bar.

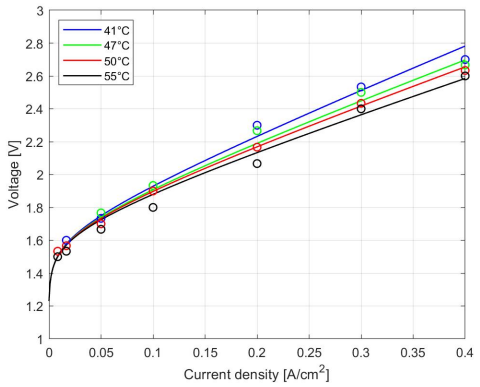

Figure 4.10: IV curve for operating a pressure of 49 bar for varying current density at four different temperature levels of 41, 47, 50 and 55 degrees Celsius. Data points in the graph are averages of multiple values gathered during experiments. The IV curve comes from curve fit function: $U = U_{rev} + a \cdot log\left(\frac{b+\frac{c}{T}+\frac{d}{T^2}j+1}{e}\right) + \left(\frac{f+g\cdot T}{e}\right)j$. Curve fit becomes less representative for the highest temperature.

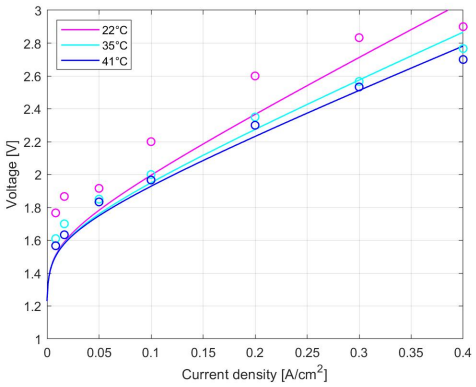

Figure 4.11: IV curve for operating a pressure of 2 bar for varying current density at three different temperature levels of 22, 35 and 41 degrees Celsius. Data points in the graph are averages of multiple values gathered during experiments. The IV curve comes from curve fit function: $U = U_{rev} + a \cdot log\left(\frac{b+\frac{c}{T}+\frac{d}{T^2}j+1}{e}\right) + \left(\frac{f+g\cdot T}{e}\right)j$. Curve fit becomes less representative for the lowest temperature.

The curve fit shows to reasonably represent the experimental data, except for the highest temperature and the lowest temperature data points. In order to get a more representative curve fit for the experimental data, the curve fit function in equation 4.2 is used, which simplifies the curve fit from Rahim et al. and takes out the temperature dependence.

$$U = U_{rev} + a \cdot log(b \cdot j + 1) + c \cdot j \tag{4.2}$$

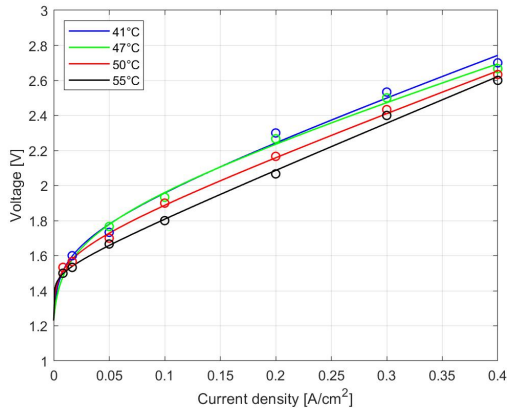

Figure 4.12: IV curve for operating a pressure of 49 bar for varying current density at four different temperature levels of 41, 47, 50 and 55 degrees Celsius. Data points in the graph are averages of multiple values gathered during experiments. The IV curve comes from curve fit function: $U = U_{rev} + a \cdot log(b \cdot j + 1) + c \cdot J$

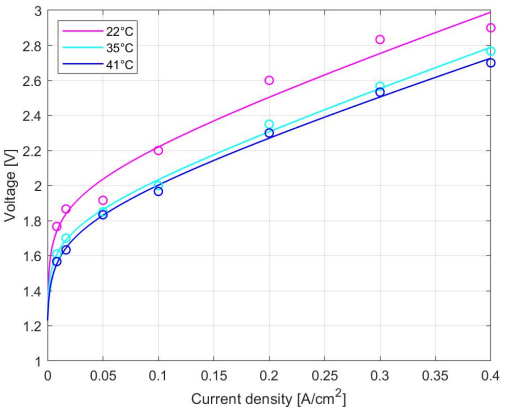

Figure 4.13: IV curve for operating a pressure of 2 bar for varying current density at three different temperature levels of 22, 35 and 41 degrees Celsius. Data points in the graph are averages of multiple values gathered during experiments. The IV curve comes from curve fit function: $U = U_{rev} + a \cdot log(b \cdot j + 1) + c \cdot J$

From the graphs above, it becomes clear that operating at higher temperatures leads to a decrease in the cell voltage of an electrolyser cell and a more efficient operation, as seen in chapter 2.5.2. However an increase in current density leads to an increase in the cell voltage, decreasing the efficiency of operation. At a low pressure, the same effect of current density and temperature is observed on the cell voltage compared with high pressure operation. The measured cell voltage values for the current density range and different temperatures is presented in table 4.5 and table 4.6 for respectively operating at a 49 bar and 2 bar.

Table 4.5: Effect of current density on cell voltage when operating at a pressure of 49 bar for temperature values of 41, 47, 50 and 55 degrees Celsius.

Current density [A/cm^2]	Voltage at 41 °C	Voltage at 47 °C	Voltage at 50 °C	Voltage at 55 °C
0.008	1.53	1.50	1.52	1.50
0.017	1.60	1.57	1.57	1.53
0.05	1.73	1.76	1.70	1.67
0.1	1.93	1.93	1.9	1.80
0.2	2.30	2.26	2.17	2.07
0.3	2.53	2.50	2.43	2.40
0.4	2.70	2.67	2.63	2.60

Table 4.6: Effect of current density on cell voltage when operating at a pressure of 2 bar for temperature values of 22, 35 and 41 degrees Celsius.

Current density [A/cm^2]	Voltage at 22 °C	Voltage at 35 °C	Voltage at 41 °C
0.008	1.76	1.61	1.56
0.017	1.87	1.70	1.63
0.05	1.92	1.85	1.84
0.1	2.20	2.00	1,97
0.2	2.60	2.35	2.30
0.3	2.83	2.57	2.35
0.4	2.90	2.76	2.7

In order make a relevant comparison between operating at a low pressure and at a high pressure a similar operating temperature is required, due to the temperature effect of the measured voltage over a electrolyser cell. The lack of a temperature regulation system resulted in only one voltage measurement for the same temperature for operating at 49 bar and 2 bar. The IV curve for both values of operating pressure for a temperature of 41 °C is presented in figure 4.14. The curve fit function used comes from equation 4.1, due to being representative for the low pressure operation and the high pressure operation for the corresponding temperature.

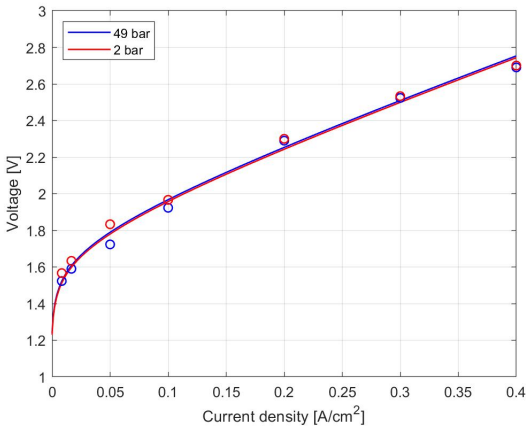

Figure 4.14: Comparison of IV curve for operating at a low pressure, 2 bar, and a high pressure, 49 bar, for a constant temperature of 41 °C. The data points for the voltage differ slightly at lower current densities but show to be equal for at the higher operating current densities. The IV curve comes from curve fit function: $U = U_{rev} + a \cdot log\left(\frac{b+\frac{c}{T}+\frac{d}{T^2}j+1}{e}\right) + \left(\frac{f+g\cdot T}{e}\right)j$

The effect of pressure on the overpotential is supposed to small, as explained in chapter 2.12.2. A small increase in overpotential is expected for operating at higher pressures according to Jang et al. [23]. From figure 4.14 it seems that at low current density values, operating at a high pressure results in a slightly lower overpotential, which is in line with the findings from figure 2.12 in chapter 2.12.2.

The effect of operating between 2 bar and 49 bar seems negligible when operating at a current densities of 0.3 and 0.4 A/cm^2. From figure 2.12 in chapter 2.12.2, overpotential for operating at 1 bar and 50 bar seem to cross at just above 0.8 A/cm^2. The difference can be explained in the differences between the experimental setup and the modelled setup by Jang et al. The effect of bubbles and dissolved gasses at higher pressures also posses difficult to model, which results in models deviating from experimental results.

4.3. Visualization of flow in the electrolyser cell.

Experiments were conducted to visualize the flow in the electrolyser cell, by zooming in with the microscope camera onto the top channel of the cell, the entrance of the top channel and onto the ceiling of the electrolyser cell. The GoPro camera was used to get an overview of all the filming positions from the microscope camera at the same time. The video footage shot at those

positions will give an insight in the flow phenomena and will validate the suspicion of flow stagnation from the temperature sensor readings. Observed flow regimes are based on the possible flow regimes presented in chapter 2.11 in figure 2.9.

4.3.1. Top channel microscope camera.

At first, the video footage shot at the top channel is analysed. The footage was shot at a pressure range of 47 to 50 bar and at a temperature range of 40 to 45 °C. The current density was varied for 0.017-0.3 A/cm^2. The filming position of the microscope camera in the electrolyser cell is shown in appendix chapter B in figure B.8(a), with the view of the camera shown in figure B.8(b).

A first observation made at the top channel, was that during certain periods of time the produced oxygen gas would stop flowing through the channel. Shortly after, a slug would be observed that travelled through the channel before it stopped moving in the camera view. This observation was made for the entire current density range and can be seen in figure 4.15. Before this phenomena, the produced oxygen would flow through the channel either as slug flow, plug flow or bubbly flow until the oxygen flow stagnates. During the time the oxygen flow is stagnant the oxygen production at the electrode continuous, which leads to the assumption that the increasing volume of oxygen in the electrolyser cell results in a relatively large, compared to the width of the top channel, oxygen bubble at the entrance of the top channel. Based on the temperature sensor data from chapter 4.1.2 and the observation made in figure 4.15 the assumption can be made that the electrolyte flow through the channel, and the electrolyte re-circulation in the electrolysis system, stagnates at certain points during operation.

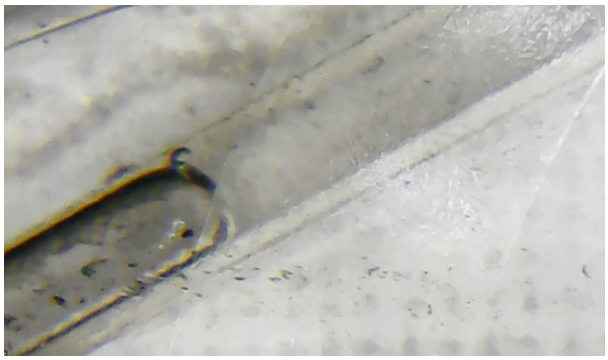

Figure 4.15: Oxygen slug being stuck in the top channel for a pressure range of 47-50 bar.

However another observation was made which counteracts the assumption that the electrolyte flow stagnates. Figure 4.16 shows the moment a slug is stuck in the channel with a channel filling bubble ahead. The buoyancy force is the driving force for the oxygen bubbles and slugs to travel into the channel and through the riser towards the flash tank. This force is counteracted by the surface tension of the build up oxygen bubble that grows during the stagnation of the oxygen flow through the channel, which is explained in more detail in chapter 4.4. However the bubble in figure 4.16 can only be held in place by a downward force generated by electrolyte flow, from the flash tank into the electrolyser cell. This generates friction which counteracts the buoyancy force of the bubble. Figure 4.17 shows how liquid can flow past a body of gas in a square duct, which further supports the theory.

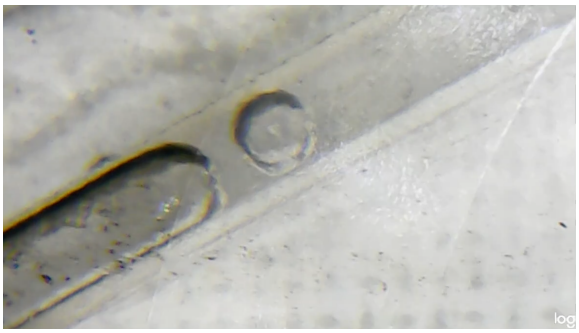

Figure 4.16: Oxygen slug stuck in the top channel with a channel filling bubble ahead which is also stuck. The bubble shows the possibility of back flow past the bubble.

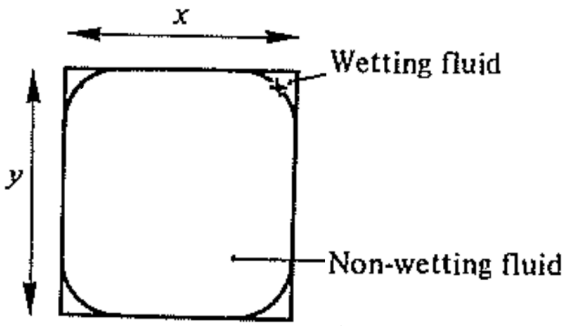

Figure 4.17: Schematic of a oxygen body traveling through a square duct. The wetting fluid in the corners suggest that back flow is possible past a slug or a bubble, as presented in figure 4.16.

The phenomena of the electrolyte flow seeming to stagnate, according to the temperature sensor data, and the stagnation of oxygen flow through the channel is discussed in more detail in chapter 4.4. First the effect of varying current density on the video footage is treated in the section bellow, followed by video footage shot at the entrance of the top channel and at the ceiling. This to get more insight in the flow through the channel before analysing the stagnation phenomena.

Effect of varying current density.

When operating at 0.3 A/cm^2, the time period without oxygen flowing through the channel showed to be the shortest compared to the other current densities The time for these periods was recorded and compared to the data from the temperature sensor. The time between peaks in the temperature data showed to be in line with the observed time between the moments the oxygen flow starts to stagnate. The time period between stagnation of the oxygen flow is called a flow stagnation cycle. The average time for a flow stagnation cycle, for operating at a high pressure and for varying current density, is presented in figure B.10 at the bottom of this section.

For operating at 0.3 A/cm^2, slug flow is immediately observed through the top channel after the build up oxygen, during a flow stagnation cycle, travels as slug through the channel. Slug flow is the main observed flow regime, and just before the flow stagnates again plug/bubbly flow is observed for a short period of time of 2 to 3 seconds. The slug flow observed is presented in figure 4.18(a) and figure 4.18(b).

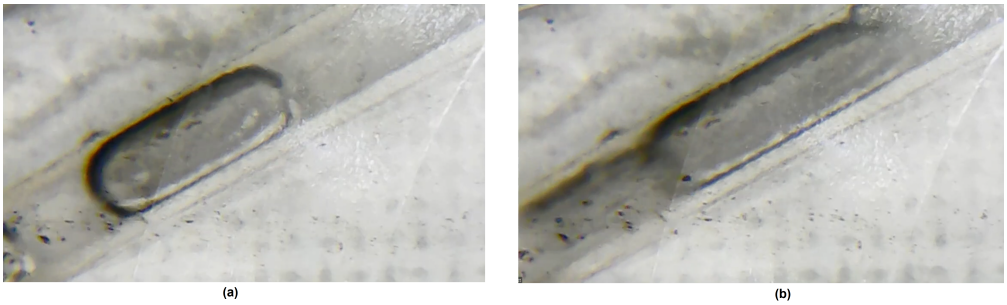

Figure 4.18: (a) Slug flow observed through the top channel at a current density of 0.3 A/cm^2. Observed at 0.3 A/cm^2. (b) Slug flow observed through the top channel, immediately after the slug generated during a flow stagnation cycle travelled through the channel. Due to the velocity of the slug, the image is blurred.

The slugs that were observed in the top channel differ in size, with an average length of 5.30 mm. The length of slugs was determined based on the dimension of the channel, being 1.5 mm in width. In time, the interval between slugs decreases and eventually the oxygen flow stagnates again. All the data gathered about the slugs is presented in table 4.7 at the end of this section for all the operating current densities.

Operating at 0.2 and 0.1 A/cm^2 resulted in the same behaviour regarded to the stagnation of the oxygen flow as with 0.3 A/cm^2. The time period of a flow stagnation cycle showed to increase with the decreasing current density. The same method for the determination was used as for 0.3 A/cm^2 and the data gathered is also presented in figure B.10. The flow through the channel observed, showed to be alternating between slug flow and plug flow, but mainly consisting of slug flow for operating at 0.2 A/cm^2, while operating at 0.1 A/cm^2 resulted in alternating slug flow and plug flow with less slug flow observed. From time to time bubbly flow is observed. In figure 4.19(a) and figure 4.19(b), the respectively observed slug and plug flow for operating at 0.2 A/cm^2 is presented. The slug flow and plug flow at 0.1 A/cm^2 is presented respectively in figure 4.20(a) and figure 4.20(b).The average slug length observed during the experiments showed to be 3.85 and 2.77 mm for respectively 0.2 and 0.1 A/cm^2.

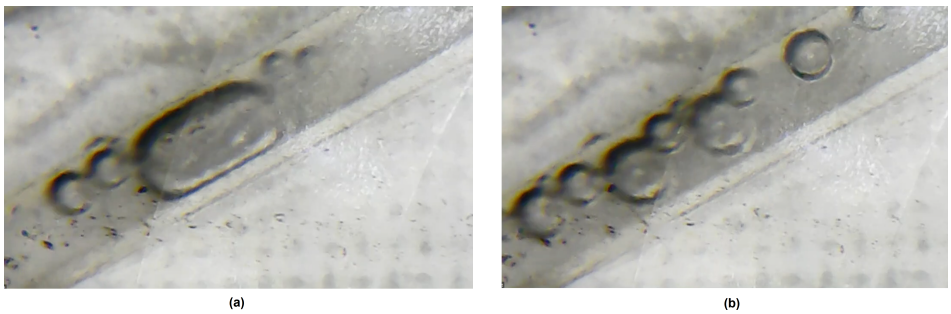

Figure 4.19: (a) Typical slug flow observed for operating at 0.2 A/cm^2. (b) Plug flow seen when operating at 0.2 A/cm^2

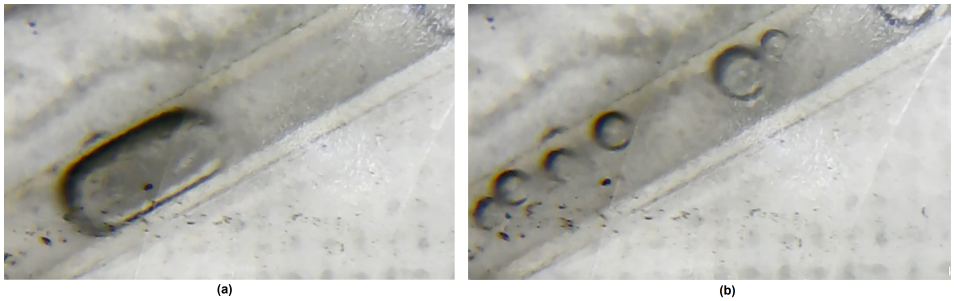

Figure 4.20: (a) Typical slug flow observed for operating at 0.1 A/cm^2. (b) Plug flow observed when operating at 0.1 A/cm^2

When operating at a current density of 0.017 A/cm^2, an interesting observation was made. The generated oxygen bubbles were able to travel through the top channel without stagnation of the oxygen flow occurring. The flow through the channel consist of bubbly flow, with most of the bubbles not clearly visible on a single frame from the video footage. Occasionally a slug, or a bubble with almost the top channel width, travels through the channel. An example of such a bubble and slug is presented in figure 4.21(a) and 4.21(b).

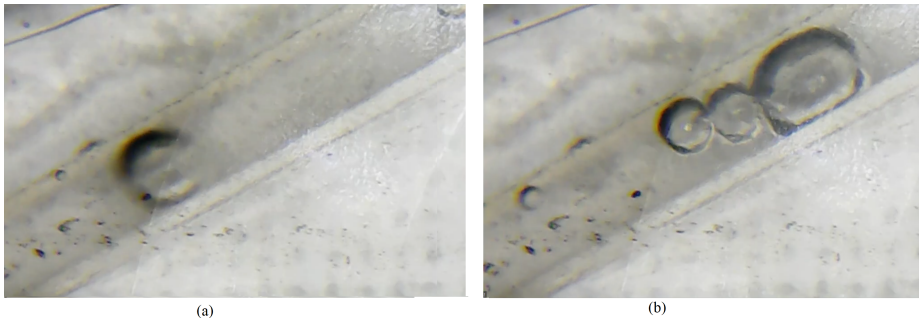

Figure 4.21: (a) Larger bubble observed through top channel when operating at a current density of 0.017 A/cm^2. Smaller bubbles travelling through the channel cannot be observed due their size and velocity. (B) Slug observed through top channel when operating at a current density of 0.017 A/cm^2.

Since the electrolyte velocity depends on velocity and volume of the produced oxygen bubbles, the stagnation cycles are undesired when considering the implementation of a temperature regulation system. Continuous flow is required for an efficient cooling. The operation at a current density of 0.017 A/cm^2 shows to be promising based on the continuous flow observed through the top channel. Operating at a lower current density also shows to be more efficient, based on the data from chapter 4.2, but does lead to a lower production rate of oxygen and hydrogen, as explained in chapter 2.10.

4.3.2. Slug flow analysis.

The data gathered during the microscope experiments regarding the flow regimes and observed slugs is presented in table 4.7 for the varying current density range. The slugs through the channel have been counted and their length recorded. Representative video footage was chosen and for each current density value 2.5 minutes of video footage were observed. When the oxygen flow stagnation was solved, slugs where observed for all current densities which had length longer the top channel part visible on the microscope camera footage. These slugs are not presented in the data in the table.

Table 4.7: Relevant data gathered about the observed slugs through the top channel for a pressure of 47-50 bar and a temperature range of 40-45 °C. Data represents 2.5 minutes of observed video footage.

Current density [A/cm^2]	Main flow regimes through channel	Average slug length [mm]	Number of slugs counted	Volume of slugs [mm^3]
0.017	Bubbly flow	2.04	11	29
0.1	Alternating slug flow and plug flow	2.77	16	64
0.2	Alternating slug flow and plug flow	3.85	27	160
0.3	Slug flow	5.3	30	255

The flow regime observed through the top channel for 0.3 A/cm^2 showed to be mainly slug flow and 30 slugs were counted during a period of 2.5 minutes. During operation, slugs were observed with lengths longer than the observed channel length. These slugs appeared the most at the 0.3 A/cm^2. For 0.2 and 0.1 A/cm^2 the flow showed to be alternating between slug flow and plug flow. At 0.2 A/cm^2 slugs were observed more regular where 27 slugs where counted compared to the 16 seen at 0.1 A/cm^2. In between slugs, plug flow was observed for which the duration increased for operating at 0.1 A/cm^2. Operating at 0.017 A/cm^2 showed a flow regime mainly consisting of bubble flow with 11 periodic, almost circular, slugs observed. All the slugs counted and their distribution of length, is presented in the histograms visible in figure 4.22.

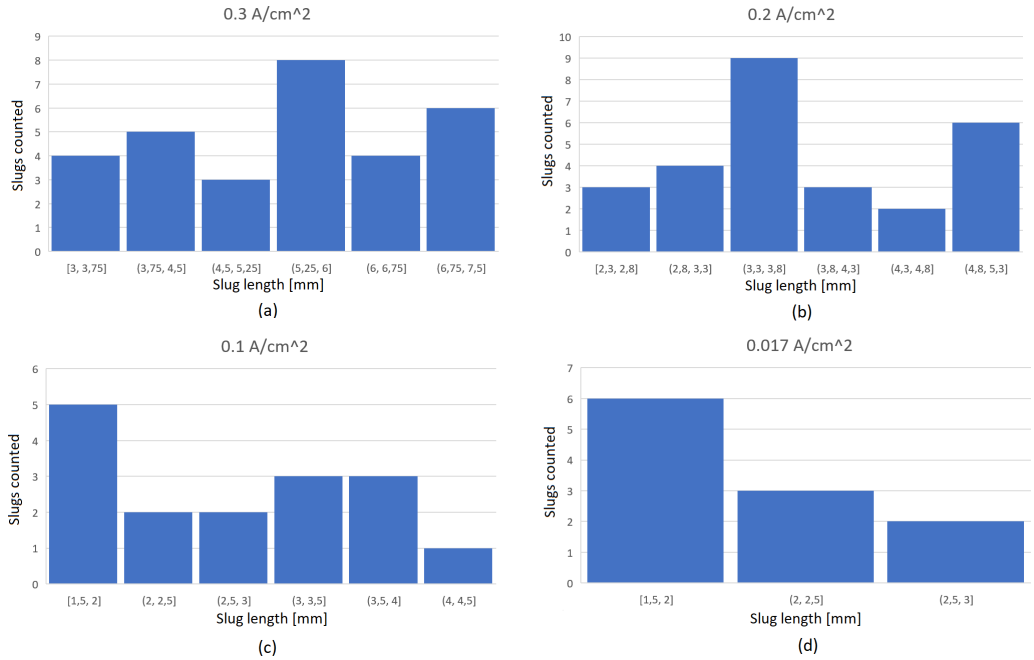

Figure 4.22: Length distribution for slugs observed through the top channel at a pressure of 47-50 bar and a temperature range of 40-45 °C for current density values of 0.3 (a), 0.2 (b), 0.1 (c) and 0.017 (d) A/cm^2.

From the histograms, it is observed that the slug length does increase with increasing current density, as would be expected according to the increase in oxygen production as explained in chapter 2.10. The maximum observed slug length shows to increase from a maximum of 2.6 mm for 0.017 A/cm^2 up to a maximum length of 7.5 mm for 0.3 A/cm^2. From the flow regime map presented in figure 2.9 in chapter 2.11, it is seen that an increase in superficial gas velocity and electrolyte velocity does lead to slug flow occurring. The increase in oxygen production, which comes from operating at a higher current density, relates to the increase in oxygen gas velocity through the top channel. The increase in buoyancy driving force also leads to an increase in electrolyte velocity through the top channel. This validates the observed increase in slugs when increasing the operating current density. In the section below, the volume of the total amount of slugs observed during a flow stagnation cycle is compared with the theoretical produced volume of oxygen gas during the period the flow through the top channel is not stagnant.

4.3.3. Preliminary oxygen flow stagnation analysis.

The video footage and data from the temperature sensor both show that the oxygen flow through the top channel stagnates during certain periods in time when operating at a high pressure range of 47-50 bar. It was shown that electrolyte is able to flow past bodies of gas in the channel as back flow, see figure 4.17, but the volume of electrolyte flow is assumed to be really small for convenience. This enables the use of the words: flow stagnation and flow stagnation cycle. Both the video footage and temperature data showed to be in line with each other, which gives the assumption that the data should be representative.

The first relevant set of data gathered, provides insight in the average time period of a flow stagnation cycle, which is presented in figure 4.23. The data was gathered for operating at a pressure of 47-50 bar, for a temperature range of 40-45 °C and for varying current density between 0.017-0.4 A/cm^2. For operating at 0.4 A/cm^2 mostly sensor data was gathered during experiments and at the end of the experimental phase video footage was shot for this current density. Because the data seems representative, it is added to the analysis is this section. The period of a flow stagnation cycle, t_{cycle}, can be divided into a period where there is flow through the top channel and a period where there is stagnation of the flow, as presented in equation 4.3.

$$t_{cycle} = t_{flow} + t_{stagnation} \tag{4.3}$$

Where t_{flow} stands for the time for which flow is observed in a flow stagnation cycles, which was monitored and the average is presented in figure 4.24. The time the flow is stagnant during a flow stagnation cycle, $t_{stagnation}$, is presented in figure 4.23.

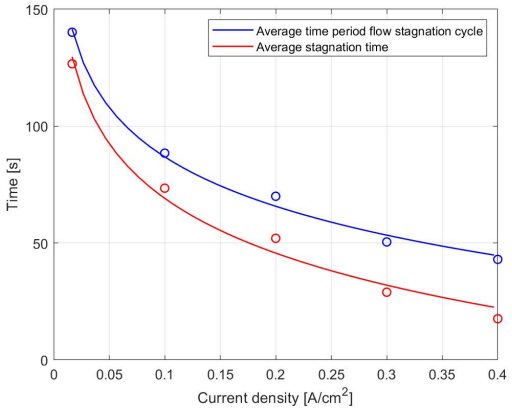

Figure 4.23: Time between occurrence of flow stagnation for a varying current density while operating at a pressure range of 47-50 bar. Line fit through the data points is made with $t = a \cdot log(j) - b$, with a = -30.48, b = 16.671 for the average time period flow stagnation cycle and a = -33.8, b = -8.7189 for the average stagnation time.

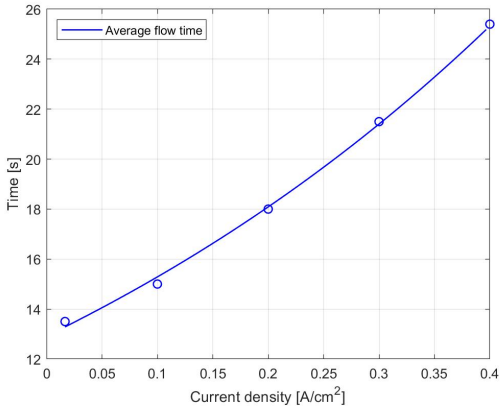

Figure 4.24: Electrolyte flow duration time after flow stagnation for a varying current density while operating at a pressure range of 47-50 bar. Line fit through the data points is made with $t = a \cdot e^{b \cdot j}$, with a = 12.918, b = 1.6829.

In order to do a clear analysis, the data of the plots, visible in figure 4.23 and 4.24 is presented in table 4.8. From the table 4.8 and the graphs presented above, it becomes clear that the period of a flow stagnation cycle decreases with increasing current density. The time period of flow during a stagnation cycle increase with increasing current density, leading to a shorter period of flow being stagnant which lowers from 90 % of flow being stagnant for 0.017 A/cm^2 to 41 % for 0.4 A/cm^2. The current density increases the production rate of oxygen at the electrode, mainly ensuring more volume of oxygen is generated in the electrolyser cell. This seems to have a positive effect on the period of a flow stagnation cycle. The increased buoyancy force is expected to be the main contributor to the shorter period of a flow stagnation cycle, allowing the oxygen to be pushed through the channel against the surface tension, and friction force from eventual back flow. During some quick experiments, the current density was increased to 0.5 A/cm^2. During these experiments, no stagnation at the top channel occurred due to the to large amount of bubbles, and bubble volume, produced.

Table 4.8: Flow stagnation cycle data gathered at 47-50 bar and 40-45 °C for a varying current density of 0.017-0.4 A/cm^2.

Current density [A/cm^2]	**Average time period flow stagnation cycle [s]**	**Average flow period during flow stagnation cycle [s]**	**Average stagnant flow period [s]**	**Fraction stagnant flow of flow stagnation cycle. [%]**
0.017	140	13.5	126.5	90
0.1	88	15.0	73.0	83
0.2	70	18.0	52.0	74
0.3	50	21.5	28.5	57
0.4	43	25.4	17.6	41

The data from table 4.8 can be used together with the data from table 4.7 to compare the volume of the total amount counted slugs, during a flow stagnation cycle, with the theoretically produced oxygen gas during the period the flow through the top channel is observed. Since the slugs where observed and counted for a period of 2.5 minutes, the average flow duration had to be adapted based on the video footage which was used for the determination of the amount of slugs and their length. The result is shown in figure 4.25.

It must also be noted that observed slugs which where longer than the channel length in the video were not implemented in the data in table 4.7. Bubbles with a diameter which were smaller than the channel width were not counted as slugs. An estimation has been made for the length of the uncounted long slugs, which is assumed to be 13 mm based on top channel length, and the volume calculated, which alters figure 4.25 into figure 4.26.

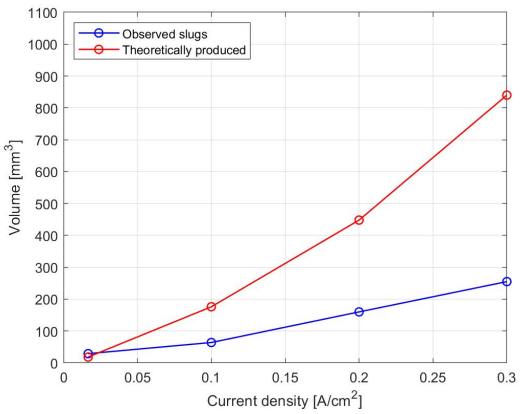

Figure 4.25: Time between occurrence of flow stagnation for a varying current density while operating at a pressure range of 47-50 bar.

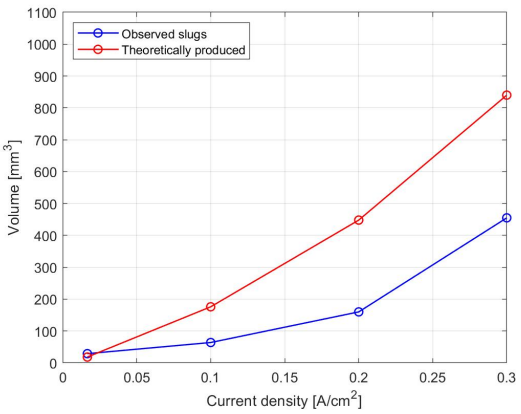

Figure 4.26: Electrolyte flow duration time after flow stagnation for a varying current density while operating at a pressure range of 47-50 bar.

From both figures, it is seen that the observed slugs have less volume than the theoretically produced oxygen during the period flow is observed through the top channel, except for operating at a current density of 0.017 A/cm^2 where the observed volume of slugs is higher. This comes due to the opening of the hydrogen purge valve during operation, re-circulating oxygen gas from the oxygen flash tank, through the downcomer, into the electrolyser cells. This phenomena is explained in more detail in chapter 4.5. The observed volume of slugs being lower than the theoretically produced oxygen is due to bubbles traveling through the top channel not being counted with the slugs. Especially during operation at 0.3 A/cm^2 bubbles were observed which had a diameter smaller than the channel width. It must also be considered that all of the applied current over the electrolyser stack is assumed to go into producing oxygen, which is lower due to leaking currents and due to bubble coverage of the electrode. A slight curve is also observed in the theoretically produced oxygen data ,due to average values for flow duration being used, which can be assumed linear based on equation 2.20 in chapter 2.10 when constant pressure and temperature are assumed. This should bring the observed and theoretical produced oxygen closer together.

4.3.4. Entrance top channel.

Experiments were conducted, for the same conditions as with the top channel experiments, with the microscope camera positioned at the entrance of the top channel. The conditions were a current density range of 0.017-0.3 A/cm^2 at a pressure range between 47 and 50 bar for temperatures between 40 and 45 °C The position and camera view are made visible in figure 4.27.

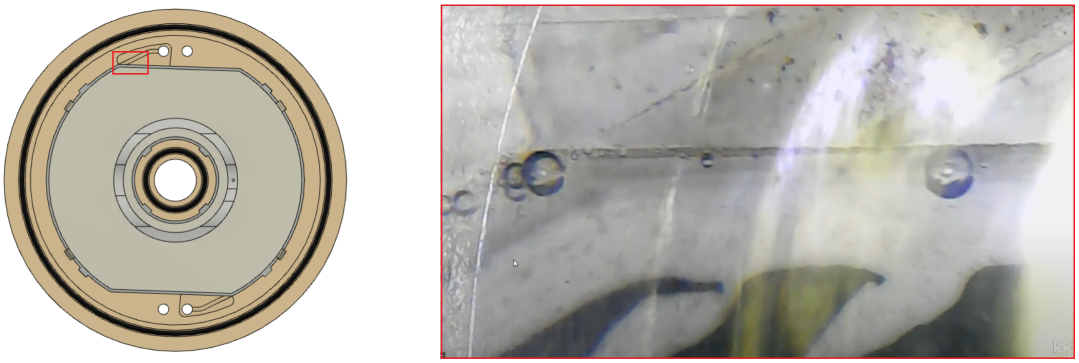

(a) (b)

Figure 4.27: (a) Filming position of microscope camera for the entrance top channel, visible in the red rectangle. (b) Microscope camera view on the entrance of the top channel.

As observed during the previous experiments at the top channel does stagnation of the oxygen flow occur during operation at high pressures. During all the experiments this flow stagnation is preceded by bubbles coalescing before the entrance of the channel. The bubbles coalescing are bubbles flowing to the entrance of the channel or trapped bubbles around the entrance. If bubbles big enough get stuck before the entrance, flow stagnation occurs due to the blocking of the channel. This effect is presented in appendix chapter B figure B.9

If bubbles get stuck before the entrance, bubbles with a smaller size ,compared to bubbles being stuck, are able to slip past into the channel. Eventually the oxygen flow through the channel stagnates, gradually lowering the void fraction in the channel up to this moment. Because of the blocking of the channel, the re-circulation of the electrolyte decreases in velocity, due to the flow of the electrolyte being halted by the coalescence of bubbles. The assumption that the electrolyte velocity, and volumetric flow, through the channel decreases come from the data temperature sensors, which shows the fluctuating pattern as seen in figure 4.8.

If the coalesced bubbles before the channel reach a critical size, around 2.5 mm, it can be seen that the bubble wants to enter the channel, due to the buoyancy force, but the surface tension pulls it out. Figure 4.28(a) shows the moment the bubbles before at entrance of the top channel have coalesced into a volume body of oxygen, which tries to enter the channel but is denied from the entering the channel by the surface tension. Figure 4.28(b) shows at later moment in time when the gas liquid interface in the electrolyser cell started to drop due to the build up of oxygen gas.

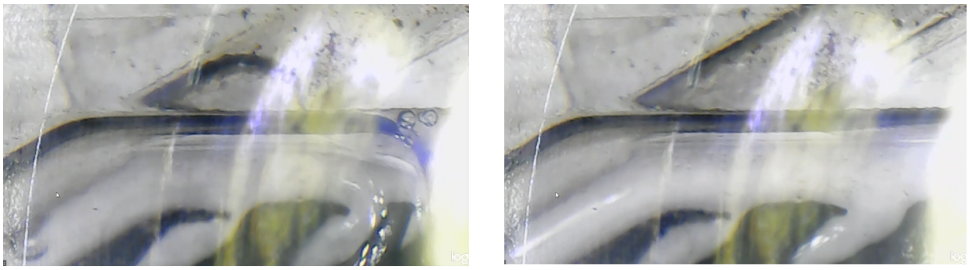

(a) (b)

Figure 4.28: (a) Volume body of oxygen stuck before the entrance of the top channel. Oxygen is partially entering the channel but not completely, due to the surface tension counteracting the buoyancy force. (b) Volume body of oxygen increases in volume. More electrode surface starts to become covered with oxygen gas. From the reflections, it seems that there is a thin electrolyte film present.

During the flow stagnation, the gas liquid interface in the electrolyser cell drops steadily until a large enough volume of oxygen gas is reached, with enough buoyancy driving force, to push the build up oxygen volume into the channel to the flash tank. Due to the lowering of the gas liquid interface, the electrode could become dry, only being in contact with the oxygen gas. However during the video footage a thin film of electrolyte seems to be present on the electrode surface. During the experiments with the microscope camera at the ceiling, the video footage provides a better view during this particularly moment so this phenomena is treated in chapter 4.3.5.

Effect of varying current density.

With the top channel experiments at 0.3 A/cm^2, the flow in the channel showed to be slug flow. The video footage from the entrance of the top channel confirms this observation. Just after flow stagnation, bubbles are observed to travel to the entrance, most of them coming from the right against the ceiling. These bubbles enter the channel resulting in slug flow, which can be seen in figure 4.29(a). Only a few seconds later more bubbles appear from the right of the figure, which coalescence before the entrance of the channel into larger bubbles with a diameter around 2.5 mm. After this moment, slug flow through the channel is observed as can be seen in figure 4.29(b). The slug flow remains to be observed until flow stagnation occurs.

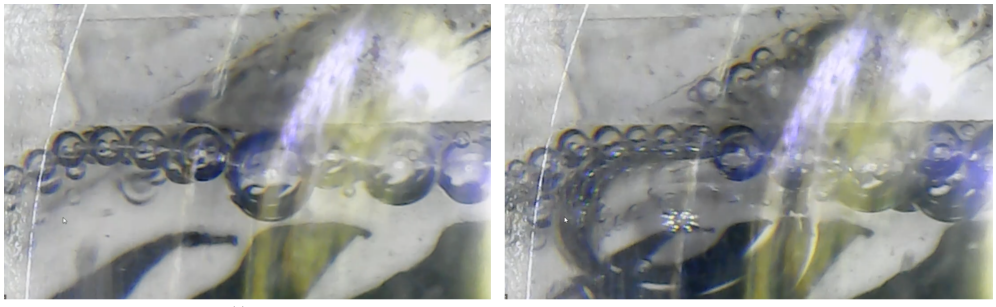

(a) (b)

Figure 4.29: (a) Oxygen bubbles entering the entrance of the top channel at 0.3 A/cm^2. Slug flow seems to be visible in the channel due to the velocity of the bubbles blurring the image.(b) Slug flow observed through the entrance of the channel due to coalescing of bubbles. The larger bubble visible before the entrance eventually grows in size and blocks the channel completely.

At an operating current density of 0.2 A/cm^2 or 0.1 A/cm^2, the same effect is observed as with 0.3 A/cm^2. Bubbles coalesce before the entrance of the top channel, leading to slug flow due to the large bubbles being pushed through the channel and eventually causing flow stagnation. However, it is observed that smaller bubbles can slip past the partly blocked channel from time to time. This results in alternating plug and slug flow through the channel, which was also observed with the earlier experiments at the top channel. In figure 4.30 the partially blocking of the channel by bubbles is shown, with smaller bubbles being able to pass through into the channel, resulting in alternating plug and slug flow.

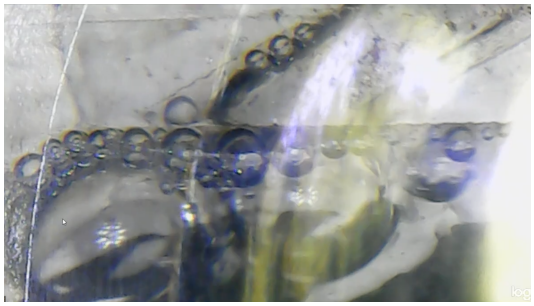

Figure 4.30: Coalescent oxygen bubbles blocking the entrance of the channel, with small bubbles being able to pass through into the channel, resulting in mixed plug and slug flow.

Entrance top channel 0.017 A/cm^2

When operating at a current density of 0.017 A/cm^2, two different observations were made for two sets of experiments. As stated in chapter 4.3.1, did operating at a current density of 0.017 A/cm^2 result in continuous flow through the top channel, without flow stagnation occurring. The same behaviour of flow was seen with the experiments at the entrance of the top channel. The video footage shows that due to the low current density value, the generated bubbles move at a lower velocity compared to operating at a higher current density. This due to the production rate of oxygen being lower, as explained in chapter 2.10. The result is that the lower gas fraction reduces the buoyancy driven re-circulation, leading to a decrease in bubble velocity. The lower oxygen production rate, combined with a decrease in velocity of the oxygen bubbles, leads to a constant flow through the top channel. Bubbles get stuck before the entrance occasionally, as can be seen in figure 4.31. Other bubbles are able to slip past into the channel when this occurs.

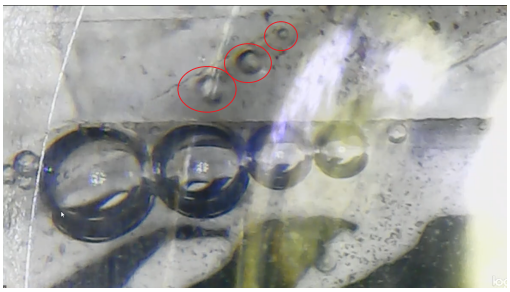

Figure 4.31: Top entrance of the channel when operating at a low current density of 0.017 A/cm^2. Smaller bubbles can be seen entering the channel, encircled in red, even though larger bubbles partially block the channel.

The observations done at the entrance of the top channel,when operating at a low current density of 0.017 A/cm^2, imply that the combination of a low velocity buoyancy driven electrolyte re-circulation and smaller bubble size lead to a continuous operation without flow stagnation occurring. As mentioned in the top channel experiments, are occasionally slugs observed through the top channel.

Bubbles can get stuck in the left corner of the ceiling or at the entrance. These bubbles take longer to grow, due to the lower current density, but can eventually block the entrance of the channel. Figure 4.32(a) shows bubbles stuck before the entrance, with an at the ceiling coalescent bubble moving from the right. When the moving bubble connects to the most right of the bubbles being stuck, they coalescence into a larger bubble which slowly enters the channel due to the buoyancy force, as shown in figure 4.32(b). The assumption is the fluidic shear stress is counteracting the buoyancy force, which results in the slow movement of the bubble trough the channel. At higher current densities it is assumed that the surface tension is dominant in keeping the bubble from entering the channel.

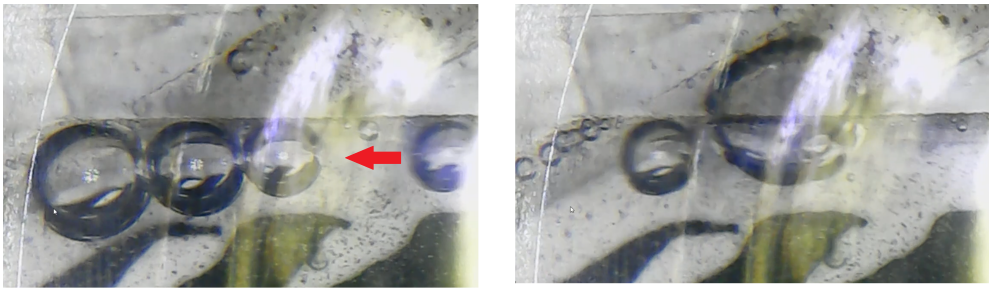

(a) (b)

Figure 4.32: (a) Three oxygen bubbles partially blocking the channel with a bubble coming in from the right. The red arrow shows the path the rightmost bubble takes before coalescing with the bubbles before the entrance. (b) All the bubbles coalescent into one large bubble, which is slowly driven into the top channel.

After the experiments conducted above, a new set of experiments was conducted with the same operating conditions and microscope camera present at the entrance of the top channel. Before this set of experiments, a small leak was found in a manual purge valve at the hydrogen storage tank. The faulty leak valve was replaced and the experiments treated in the section above repeated. It must be noted that all the experiments presented in this chapter were done with a leak tight setup, except the first set of experiments done at the entrance of the top channel for a current density of 0.017 A/cm^2 in chapter 4.3.4 . For the current density range of 0.1-0.3 A/cm^2 the video footage showed to be the same as with the earlier experiments. However when operating at a current density of 0.017 A/cm^2 or below, flow stagnation did occur. This due to coalescent bubbles not being able to enter the channel anymore. Figure 4.33 shows a coalescent bubble that would have gone into the channel, as previously observed, but immediately gets stuck.

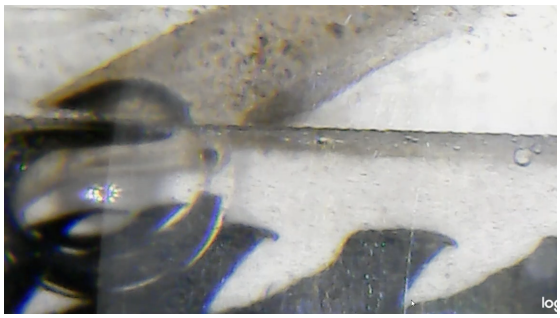

Figure 4.33: Coalescent bubble seen stuck at the entrance of the top channel when operating at a current density of 0.017 A/cm^2.

When comparing the sensor data from both the experiments, the only difference found was that the pressure slowly dropped with the first set of experiments, due to the leaking needle valve. Data from the pressure sensors for both experiments are shown in figure 4.34 and figure 4.35 for respectively an experiment with pressure leakage and without the leaking needle valve. The operating current density for pressure leak plot is at 0.017 A/cm^2 while the other plot shows the pressure during standby when no oxygen or hydrogen is produced.

The different observation between the two experiments shows that the steady decline in pressure, due to gas being purged at the hydrogen side of the electrolysis system, has a positive influence on the occurrence of flow stagnation through the top channel at the oxygen side at lower current densities. This phenomena is treated in more detail in chapter 4.9.

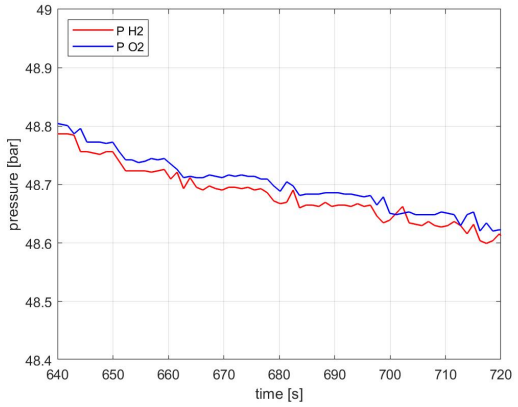

Figure 4.34: Pressure plot during operation at 0.017 A/cm^2 with leaking needle valve. The pressure drops steadily during operation.

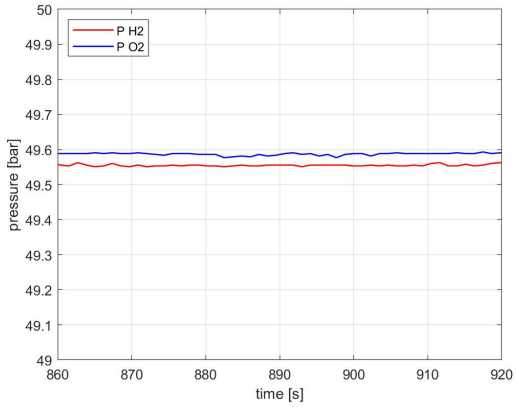

Figure 4.35: Pressure plot during standby at a pressure of 49.5 bar without pressure leakage. The pressure shows to be constant.

4.3.5. Ceiling electrolyser cell.

Experiments were conducted with the microscope camera positioned at the ceiling of the electrolyser cell. The position of the camera is presented in appendix chapter B in figure B.10(a), where the camera view is presented in figure B.10(b).

From the video footage, the effects of flow stagnation were clearly visible. When the oxygen flow stagnates, increase in volume of oxygen can be observed at the top of the electrolyser cell. On the video footage a gas liquid interface can be seen moving to the right, as can be seen in figure 4.36. Eventually the entire electrode visible in the video footage is covered by oxygen gas. This was observed for all operating current densities and temperatures and can be seen in figure 4.37.

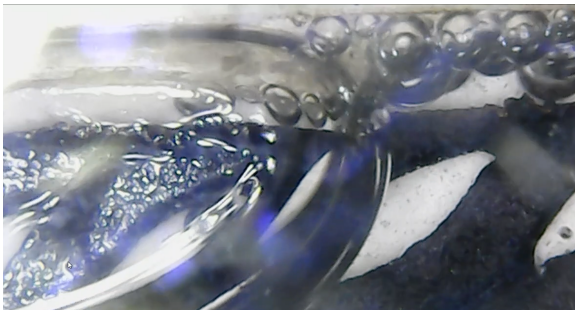

Figure 4.36: Gas liquid interface shifting to the right, due to the increase of volume of oxygen gas in the electrolyser cell due to flow stagnation occurring at the entrance of the top channel.

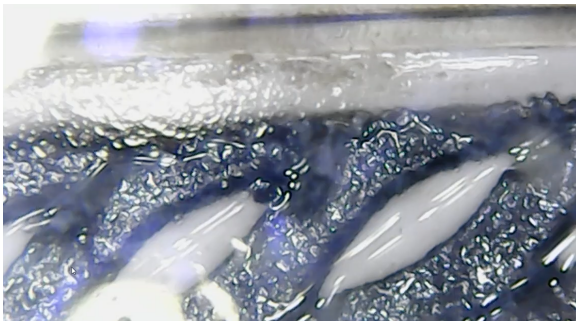

Figure 4.37: Volume of oxygen gas completely covering the view of the microscope camera. A thin liquid film seems to be present on the electrode surface, based on the reflection of light on the surface.

The electrode becoming dry, the moment when the electrolyte is directly in contact with the oxygen gas instead on the electrolyte, poses a threat to the degradation of the electrode material. However a small liquid film was observed on the electrode surface and on the Zirfon diaphragm in the electrode holes. When the video footage was inspected closely, oxygen could be seen generated at the electrode surface in the thin liquid film. It must be noted that the assumption that the electrode has a thin film of electrolyte on the surface comes only from the video footage. Reflections of light on the surface suggest that a liquid film must be presented.

An interesting observation made was the coalescence and movement of bubbles at the ceiling. It was seen that bubbles flow upwards to the ceiling and tend to get stuck at the ceiling, visible in figure 4.38(a). These bubbles grow in size due to coalescing with other bubbles, until a size is reached where bubbles will start moving to the entrance of the top channel due to the small incline of the ceiling. If these moving bubble come from the right corner of the electrolyser cell, they push bubbles in motion or coalescence with bubbles stuck at the ceiling while moving to the entrance of the top channel, increasing in size as can be seen in figure 4.38(b). Eventually, the train of coalesced bubbles reaches the entrance of the top channel and blocks it, due to the large volume of bubbles suddenly appearing, leading to a new flow stagnation cycle.

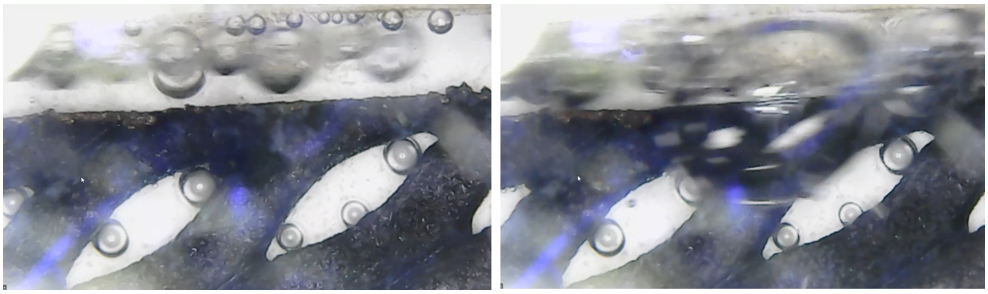

(a) (b)

Figure 4.38: (a) Bubbles can be seen stuck at the ceiling, varying in diameter size from 0.19 to 0.42 mm. The blurry bubbles which are larger in size, with an average diameter of 0.85 mm, are moving to the left towards the entrance of the top channel. (b) Larger bubble with a diameter of 3.84 mm, seen moving to the left towards the entrance of the top channel. The large bubble is a coalescence of bubbles stuck a the ceiling of the electrolyser cell.

4.4. GoPro overview.

The GoPro camera was used to get an overview footage of the top half of the electrolyser cell. Experiments were conducted for the same operating pressure and temperature range as with the microscope experiments treated above. Unfortunately no GoPro footage is made for a current density of 0.017 A/cm^2. The overview with the GoPro allows for the possibility to observe the conditions leading to stagnation of the oxygen flow and the increase of volume of oxygen gas at the top of the electrolyser cell. The volume of produced oxygen gas can be quantified based on the observation and used to determine the buoyancy driving force to push the quantity of oxygen gas through the channel. The filming position of the GoPro camera and the video view are presented in figure in appendix chapter B B.11.

The video footage from the GoPro gave more insight on the occurrence of flow stagnation in the stack. The same observation was made as with the microscope camera at the ceiling of the electrode. Bubbles tend to get stuck at the ceiling and grow in size by coalescence. Eventually the grown bubbles start moving to the left, pushing bubbles towards the entrance while also coalescing with other bubbles, which is presented in figure 4.39.

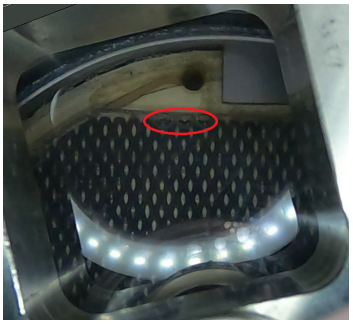

Figure 4.39: Three larges bubbles moving from the right corner of the electrolyser cell towards the entrance of the channel. The bubbles have grown in size due to coalescing with other bubbles stuck a the ceiling of flow upwards to the ceiling. The bubbles are encircled with the red oval.

When these bubbles reach the entrance of the channel, they coalesce and block the channel starting a new flow stagnation cycle, presented in figure 4.40. The oxygen volume in front the channel increases during the flow stagnation cycle, seen in figure 4.41, until the buoyancy force of the oxygen volume is large enough the allow it to enter the channel. The build up oxygen volume will from now on be referred to as a large oxygen bubble. This phenomena is analysed in more depth in the section below.

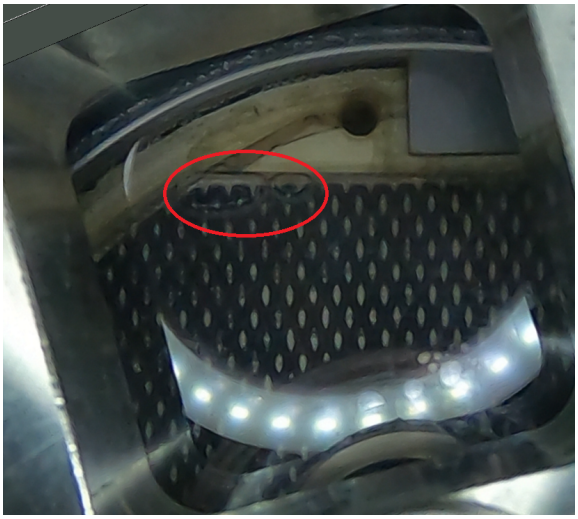

Figure 4.40: Coalesced bubbles stuck before the entrance of the top channel, after moving from the right corner of the electrolyser cell to the left, as presented in figure 4.39. The bubbles are encircled with the red oval.

Figure 4.41: Increase of oxygen volume in the electrolyser cell due to oxygen flow stagnation through the channel. The increase in oxygen volume is encircled with the red oval.

4.4.1. Flow stagnation calculations.

The assumption is made that the during a flow stagnation cycle, the surface tension of the large oxygen bubble prevents the large oxygen bubble from entering the channel. The buoyancy force increases during the increase in volume of the large oxygen bubble and eventually overcomes the surface tension force. In order to verify this assumption, calculations are made regarding the buoyancy force and the surface tension that is needed to be overcome. Data will used from the gathered data about the stagnation of the flow, from chapter 4.3.3. For convenience, the data is presented below in table 4.9.

Table 4.9: Flow stagnation data gathered from experimental phase.

Current density [A/cm^2]	**Average time for flow stagnation cycle [s]**	**Average electrolyte flow duration after stagnation [s]**	**Average stagnant flow duration [s]**
0.017	140	13.5	126.5
0.1	88	15.0	73.0
0.2	70	18.0	52.0
0.3	50	21.5	28.5
0.4	43	25.5	17.5

Table 4.9 shows that the period for a flow stagnation cycle reduces for an increasing current density. This due to the increase in oxygen production at the electrodes, as can be seen in equation 2.20. The duration of the electrolyte flow shows to increase with increasing current density. Both findings result in that an increase in operating current density allows for a shorter period of time in which there is no electrolyte re-circulation. In order to validate the findings about flow stagnation, a comparison was made between the observed volume production of oxygen, as the large oxygen bubble, and the calculation of produced oxygen during a flow stagnation cycle. The theoretical production volume of oxygen for a three cell electrolyser stack can be determined based with equation 2.20 from chapter 2.10. When multiplied with average time the flow is stagnant during a flow stagnation cycle,taken from table 4.9, an estimation can be made for the produced volume of oxygen during a flow stagnation cycle. The results are presented in figure 4.43

The observed production volume of oxygen during the period of stagnant oxygen flow through the top channel, is based on the video footage from the GoPro at the top half of the electrode. The build up of volume of oxygen in the electrolyser half cell was determined based on the size of the large oxygen bubble that increases in size during the flow stagnation cycle, as can be seen in figure 4.42. The channel width was used a reference to calculate the volume of oxygen based on the gap size and the circumference of the large bubble. Various large oxygen bubbles have been measured with this method, for the current density range of 0.1 and 0.4 A/cm^2, and their volume calculated. The volume for the observed and theoretical produced oxygen is presented in figure 4.43 for comparison.

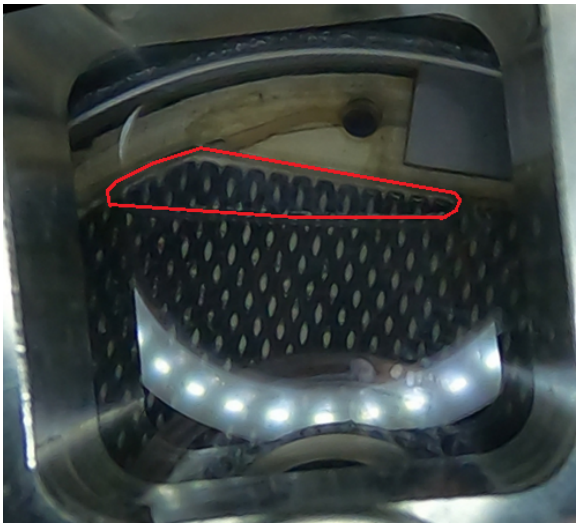

Figure 4.42: GoPro view of the in volume increasing large oxygen bubble. The bubble is traced with the red line. The volume is calculated based on the gap width between the electrode and the PMMA plate, and on the circumference of the bubble, which is used to determine the area of the bubble. The circumference is related to the circumference of a circular area and the surface area calculated and multiplied with the gap width to determine the volume of the large oxygen bubble.

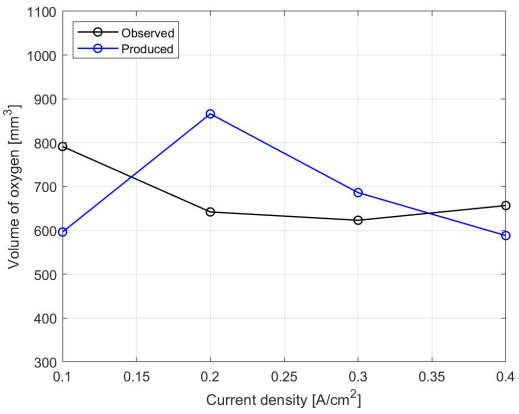

Figure 4.43: Observed and calculated oxygen volume production for the large oxygen bubble during the period the flow is stagnant during a flow stagnation cycle. The calculated production is done with average values and the observed production done by referencing the size to large bubble the width of the channel. Both are crude methods and based on the observed an calculated oxygen being roughly similar it can be assumed that the observed volume of oxygen is determined correctly.

From observing the graph, the observed volume of oxygen shows to be roughly similar for the varying current density range with the exception of 0.1 A/cm^2 being slightly higher. One large oxygen bubble measured at 0.1 A/cm^2 showed to have a volume of 1067 mm, which increased the average of the 0.1 A/cm^2 measurement. It is assumed that when more data is gathered, the average of the varying current density range will lead to the same observed volume of oxygen during a flow stagnation cycle. The graph also shows that the calculated produced oxygen volume does differ from the observed oxygen volume. However an average value was used for the time the flow was stagnant and with more data points gathered might flatten the curve of the produced oxygen volume. Since the lines are relatively close to each other, and both volumes are determined with crude methods, the assumption is made that the observed volume of oxygen is determined correctly.

The driving force for the large oxygen bubble to go into the channel is expected to come from the buoyancy force, but can be translated to the height of the large oxygen bubble above the entrance of the channel, and to a pressure by multiplying by the density and the gravity constant, as shown in equation 4.4.

$$\Delta p = h_{bubble} \cdot \rho_{elec} \cdot g \tag{4.4}$$

The large bubble is prevented from completely entering the channel due to the surface tension, that wants to minimize the surface area of the bubble. The top channel has the shape of a rectangular duct with a height of 1.5 mm and a width of 1.5 mm, as shown in figure 4.44. When the bubble is partially in the channel, the pressure difference over the liquid gas interface can be calculated with the Laplace pressure difference. Equation 4.5 can be used to determine the Laplace pressure difference for a slug in a duct according to R. Lenormand et al. [30]. In the equation, 0.94 comes from a constant calculated based on the dimension of the duct.

$$\Delta p = 2 \cdot \sigma_{elec} \cdot cos(\alpha_{slug}) \cdot 0.94 \cdot \left(\frac{1}{x} + \frac{1}{y}\right) = 2 \cdot 0.096 \cdot cos(58) \cdot 0.94 \left(\frac{1}{0.0015} + \frac{1}{0.0015}\right) = 120pa \tag{4.5}$$

The equation uses the surface tension σ, the dimensions of the channel, width x and height y, and the contact angle of the slug against the wall for the calculation. The value for the surface tension is taken from research by P.M Dunlap et al. [11]. The contact angle of the slug was determined based on the video footage at the top channel at the moment the slug would start flowing further into the channel, and the average was taken for the calculation of the Laplace pressure. The contact angle of the slugs showed to be roughly the same for all the operating current densities, with an average contact angle of 58 degrees. The method for obtaining the contact angle is visible in figure 4.45.

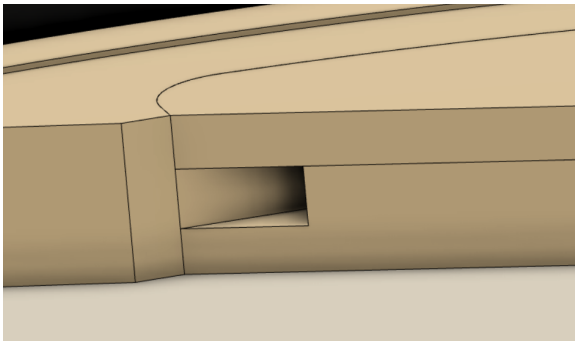

Figure 4.44: Zoom in of the entrance of the top channel. The channel has a square duct geometry with a height of 1.5 mm and a width of 1.5 mm. The large oxygen bubble needs to pushed into the channel while the surface tension wants to minimize the surface area of the large oxygen bubble. Image obtained from ZEF.

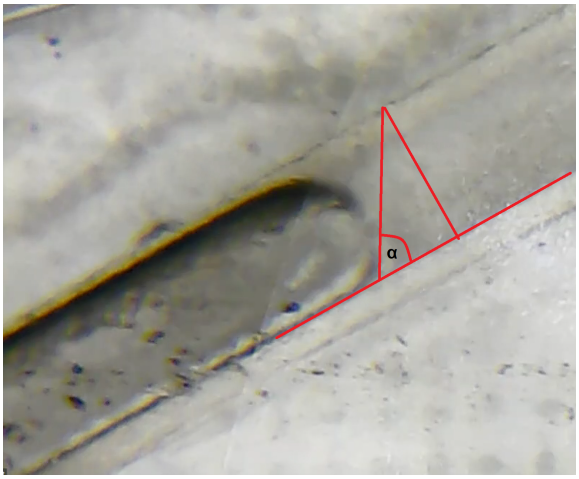

Figure 4.45: Calculation of the contact angle of the slug against the wall the moment the slug starts flowing into the channel completely. The microscope camera is placed at a small angle during these experiments, due to the size of the look through windows, which affects the determining of the contact angle of the slug with the wall.

The Laplace pressure can also be translated into a height by dividing by the density of the KOH and the gravity constant. The height taken from this calculation can be plotted against the height determined for the large oxygen bubbles, to verify the assumption that the surface tension prevents the large oxygen bubble from completely entering the top channel. In figure 4.44, the height of the large oxygen bubble and height taken from the Laplace pressure are plotted against the current density range. The same is done in figure 4.47 for the pressure corresponding with the height. The heights show to be of roughly the same magnitude, which validates the assumption that the surface tension is keeping the bubble from entirely entering the channel. From 4.43 it becomes clear that there is no difference in necessary volume for the large oxygen bubble to travel through the channel. This further verifies the assumption that surface tension is the main counter force to the buoyancy force.

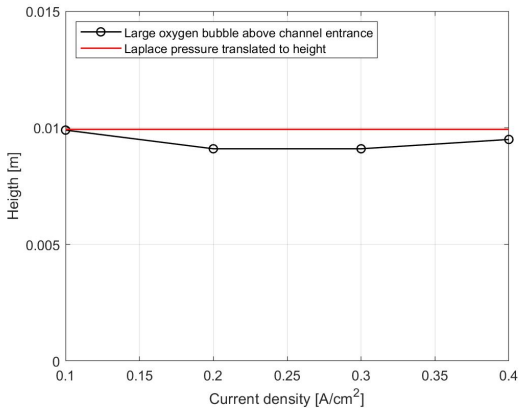

Figure 4.46: Height of the large oxygen bubble compared against the translation of the Laplace pressure in the top channel to a height. The height and Laplace pressure are determined at the moment the large oxygen bubbles starts flowing into the top channel.

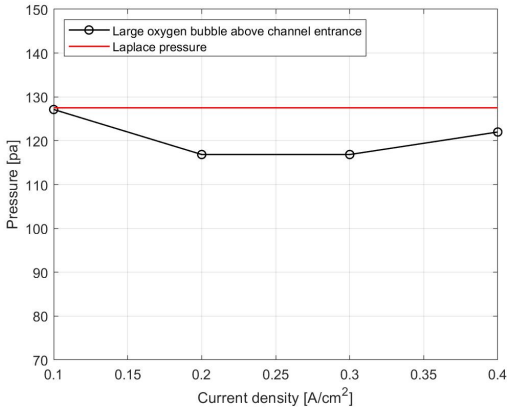

Figure 4.47: The eight of the large oxygen bubble translated to a pressure difference against the Laplace pressure in the top channel. Both pressures are determined at the moment the large oxygen bubbles starts flowing into the top channel.

The stagnation of the flow has a main disadvantage in that the electrolyte circulation is stopped for a period of time, which becomes longer with decreasing operating current density. The electrolyte circulation allows for better regulation of the temperature inside the electrolyser stack, even more with an eventual heat exchanger implemented in the downcomer. The temperature increase during a flow stagnation cycle leads to an increase of oxygen dissolved in the electrolyte bulk, which has a negative impact on gas crossover and the UEL, as explained in chapter 2.8. Another downside for the flow stagnation is that less oxygen is produced at the electrode surface due to less contact with the electrolyte. During the experiments a thin film of electrolyte was seen present at the electrode during a flow stagnation cycle, but this could not be verified by other means. Based on the flow stagnation occurring in all the electrolyser cells and due to coalescence of bubbles before the entrance, it can be assumed that even with a larger electrolyser stack, consisting of more electrolyser cells, stagnation of flow in the top channels will occur. It must be noted that the eventual electrolyser stack should be able to operate at higher temperatures, which increases the volume of produced oxygen according to the ideal gas law, and should lead to a shorter period for flow stagnation cycles.

One interesting observation was made during experiments with a previous electrolyser stack design, which consisted of electrolyser discs with a thicker bipolar plate. These experiments were done to get a feel for the setup and how to operate it. During these experiments current densities were reached, at a pressure range of 47-50 bar, of 0.7 A/cm^2. When disassembling the stack, black residue was found on the oxygen side of the Zirfon diaphragm, only for the middle electrolyser cell, as can be seen in appendix chapter B in figure B.12. The black residue came from the electrodes, which where slightly degraded, and from the PSU material, which was melted and burned. This was seen on both the hydrogen side and the oxygen side, where the Zirfon diaphragm had black residue on the same position as where the large oxygen bubble would be expected during a flow stagnation cycle. This phenomena requires further investigation but hints that the build up of oxygen gas can lead to an sudden increase in temperature for higher current densities.

4.5. Influence of pressure control valves

During operation of the electrolyser stack, the pressure control system activates at certain moments, as explained in chapter 3.2, resulting in the opening of the oxygen or hydrogen purge valve for respectively 100 and 50 ms. The opening of the valves influences the pressure level and the electrolyte level in the electrolysis system, resulting in flow of electrolyte to certain parts of the system. This chapter will give an insight in the influence of the opening and closing of the purge valves on the electrolyser cell, based on the video footage shot by the microscope camera when operating at a high pressure range of 47-50 bar. Three different filming positions are checked in this chapter: the top channel, the entrance of the top channel and the bottom channel.

4.5.1. Top channel.

The opening of one of the two purge valves resulted in the same observation for the video footage at the top channel. Directly after opening one of the valves, a drastic increase in electrolyte re-circulation velocity would be observed. The bubbles through the channel become blurry on the video footage due to the increase of velocity. Electrolyte and bubbles are sucked into the channel, trough the entrance, for a few seconds before the electrolyte re-circulation velocity seems to lower in velocity. In case of flow stagnation, when the oxygen gas is observed motionless in the channel, the opening of both of the valves resulted in an immediate increase of electrolyte and bubble velocity through the channel, solving the flow stagnation. The slug made up of the build op oxygen during a flow stagnation cycle can be seen in figure 4.48. The only difference between the opening of the oxygen purge valve and the hydrogen purge valve is the duration of the increased electrolyte re-circulation velocity, which takes one or two seconds longer after opening of the oxygen purge valve. The difference comes from the oxygen flash tank being directly connected to the oxygen side of the electrolyser cell through the top channel, header and riser tube. The pressure drop in the flash tank creates a pressure difference compared to the electrolyser cell, which triggers the flow of electrolyte. Besides, the model from I. Danniil [9] showed that it takes longer for the pressure in the oxygen flash tank to stabilize.

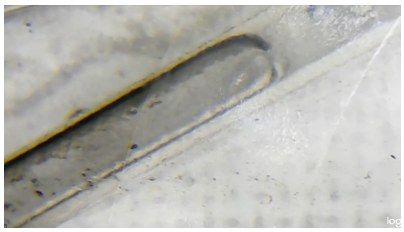

Figure 4.48: Large slug observed after opening of the oxygen or hydrogen pruge valve in the top channel.

4.5.2. Entrance top channel.

The effect of opening the oxygen and hydrogen purge valve on the electrolyte flow through the channel was also observed for the entrance of the top channel. The same effect was observed as with the top channel experiments, namely the increase in electrolyte re-circulation velocity after the opening of one of the valves. In case of flow stagnation or bubbles being stuck around the entrance, the opening of one of the purge valves resulted an immediate solving of the flow stagnation. The video footage corresponding with this observation is shown in figure 4.49.

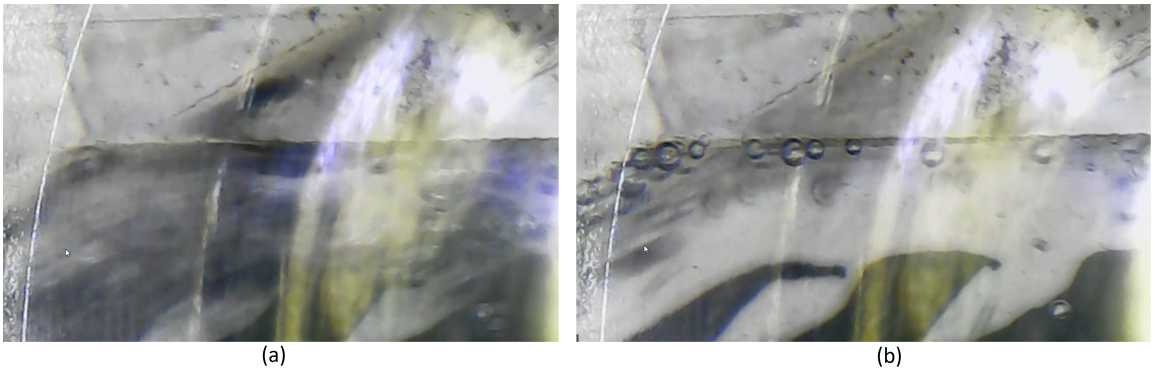

(a) (b)

Figure 4.49: (a) Flow of the large oxygen bubble through the entrance of the top channel, one second after opening of the oxygen purge valve. The oxygen flow through the channel was stagnant before the opening of the purge valve. The image is blurry due to the immediate increase of velocity of oxygen gas through the channel. (b) Surge of bubbles through the entrance of the top channel after the large oxygen bubble left the electrolyser cell. Bubbles show to move at a higher velocity through the channel, compared to the flow velocity without opening of the oxygen purge valve. The bubbles clearly visible are bubbles that are stuck at the ceiling.

Here figure 4.49(a) shows the flow of the large oxygen bubble through the entrance of the top channel. A increase in velocity of electrolyte and bubbles was observed, due to the blurry images. Figure 4.49(b) shows the flow through the channel four seconds after figure 4.49 (a). The flow velocity through the channel seem to be higher compared to the flow without opening of the purge valve. The increased flow velocity relates to a higher electrolyte re-circulation velocity, which shortens the residence time of bubbles on the electrode surface. This results in smaller bubbles leaving the electrode surface and a lower chance for bubbles to coalescence. The electrolyte velocity slowly decreases until a level comparable to flow through the channel, without the opening of the oxygen purge valve, and eventually flow stagnation will occur.

4.5.3. Bottom channel.

Video footage was shot with the microscope camera at the bottom channel of the electrolyser cell. Since this filming position and view of the microscope camera were not yet treated, they are presented in appendix chapter B in figure B.13. The bottom channel video footage resulted in different observations for the opening of respectively the oxygen and hydrogen purge valves. The opening of each valve is treated individually below.

Opening of oxygen purge valve.

As explained above in this chapter does the opening of the purge valves show to have an effect on the re-circulation of the electrolyte flow. When the oxygen purge valve was opened, an immediate increase in electrolyte velocity through the bottom channel was observed followed by a slug through the channel. The effect showed to be the same for various operating conditions and is made visible in figure 4.50.

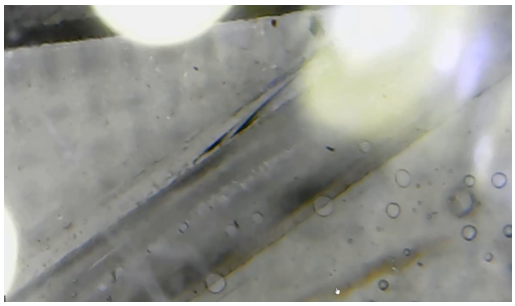

Figure 4.50: A slug observed through the bottom channel just after opening of the oxygen purge valve. The high velocity of the slug only allows for blurry images due to the low frame rate of the microscope camera.

The re-circulation of oxygen in the form of bubbles or slugs poses no threat to the electrolysis process. However when the bubbles re-circulating are made up of hydrogen gas, they pose a risk due to the increase in gas crossover. The slug observed in figure 4.50 did travel through the oxygen footer to the anode side of the electrolyser cell, where oxygen is produced. It seems unlikely that the slug comes from the oxygen flash tank, based on the direction of the flow in the electrolysis system after opening of oxygen purge valve, as explained in chapter 3.2.2. It also seem unlikely that the slug travelled from the hydrogen side, either the flash tank or one of the electrolyser half-cells, through the pressure equalization tube to the oxygen half-cell, due to the length of the Swagelok tubing on the hydrogen side and the length of the pressure equalization tube. This is explained in more detail in chapter 4.6. An explanation may be the formation of hydrogen at the top plate of the electrolyser stack. The top plate serves as a cathode and will produce hydrogen inside the half cell it is connected to. However it will also produce hydrogen at the channels in the top plate and the connecting Swagelok tubes. Due to the flow stagnating for considerable periods of time, hydrogen bubbles are allowed to grow and coalescence in the stagnant electrolyte in those parts. When the electrolyte

re-circulation starts flowing again due to the opening of the oxygen valve, the accumulated hydrogen bubbles travel through the footer channels to the hydrogen side of the electrolyser cells but also to the oxygen side of the electrolyser cells, resulting in an increase in gas crossover of hydrogen to the oxygen side. This theory is examined in more depth in chapter 4.7.

Opening of hydrogen purge valve.
The opening of the hydrogen purge valve has a similar effect on the re-circulation of the electrolyte as the opening of the oxygen purge valve. There is an increase in electrolyte velocity through the bottom channel immediately after opening the valve. However there is a secondary effect observed that differs from the opening of the oxygen purge valve. Instead of a small slug or bubbles travelling through the bottom channel, large slugs are observed, presented in figure 4.51(a). The length of the first slug is longer than the width of the camera view, visible in figure 4.51(b), followed by shorter slugs which range between 1.5 mm and 0.3 mm

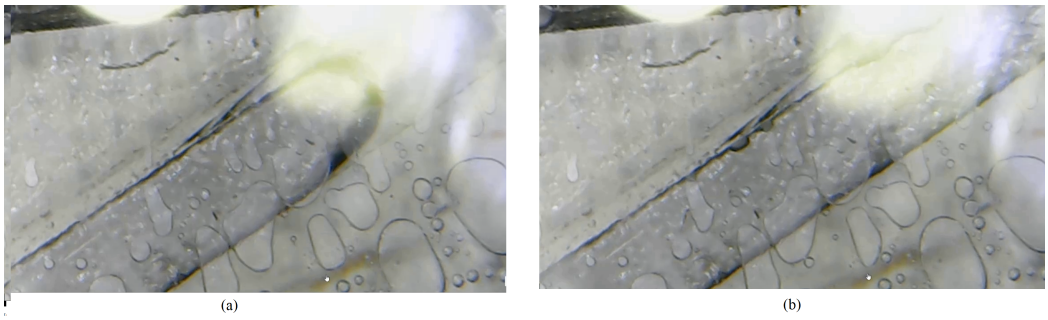

Figure 4.51: (a)(b) Slugs observed through the bottom channel after opening of the hydrogen purge valve. The flat looking bubbles are pockets of gas stuck between the PSU covering the bottom channel and the PMMA plate.

Based on the flow of electrolyte in the electrolysis system, as explained in chapter 3.2.2, it is assumed that the slugs consist of oxygen gas that is re-circulated through the downcomer into the electrolyser cell. In chapter 4.6, this observation is analysed into further depth.

4.6. Electrolyte flow direction electrolysis system.

The direction of the electrolyte flow in the electrolysis system can have a negative impact on the safety during operation. Gas crossover can occur through electrolyte mixing, as mentioned in chapter 2.8, which can lead to reaching the explosion limits for either oxygen or hydrogen. There is a small constant flow of electrolyte through the pressure equalization tube from the oxygen side to the hydrogen side, due to the small pressure difference in both of the flash tanks. However the opening of the oxygen or hydrogen purge valve results in larger pressure drops in the flash tanks, 0.4 bar and 2.7 bar for respectively the oxygen and hydrogen purge valves when operating at 50 bar. This is verified by the experimental data, in chapter 4.1.3 and predicted in the model of I. Daniil. These larger pressure drops result in a higher velocity of electrolyte in the system, which enhance the possibility of electrolyte mixing through the pressure equalization tube. This chapter will focus on validating the electrolyte flow direction as predicted by the model of I. Daniil by comparing it with the observations during the experiments and with calculations made for the resistance coefficients in the system.

4.6.1. Resistance coefficient calculations.

In order to determine the direction of the electrolyte flow after the opening of one or both of the purge valves, the pressure control scheme in chapter 3.2.2 can be consulted. The control scheme is based on the electrolyser model from I. Daniil. In order to validate the electrolyte flow direction, resistance coefficients were calculated for the components through which the electrolyte is transported in the electrolysis system. Based on the pressure drop and the resistance coefficients, the direction of the electrolyte flow and the volume flow rate can be determined. Flow follows the path of the least resistance, corresponding with the lowest resistance coefficient. The pressure difference over certain parts in the system relates to equation 4.6.

$$\Delta p = \dot{V}_{elec} \cdot K \tag{4.6}$$

where $\dot{V}_{elec}$ stands for the volume flow of electrolyte and K is the resistance coefficient. The resistance coefficients dependent on the geometry of the components in the electrolysis system. There are three different geometries present in the system, namely: circular tubes, square ducts and planar cells. For each different geometry, the resistance coefficient is calculated. For the calculations the assumption is made the flow in the system is laminar. For simplicity, entrance and corner effect are not taken into consideration.

For circular tubes, such as the downcomer, the riser and the pressure equalization tube, the resistance coefficient can be determined based on the Hagen Poiseuille equation, shown in equation 4.8. The Darcy friction factor can be determined with equation 4.7, where D stands for the channel diameter.

$$f_D = \frac{64}{Re} = \frac{64 \cdot \mu_{elec}}{\rho_{elec} \cdot u \cdot D} \tag{4.7}$$

$$\Delta p = f_D \cdot L \cdot \frac{\rho_{elec}}{2} \cdot \frac{u^2}{D} = \frac{8}{\pi} \cdot \frac{L \cdot \mu_{elec}}{r^4} \cdot \dot{V}_{elec} = K_{circ} \cdot \dot{V}_{elec}. \tag{4.8}$$

The top and bottom channels in the electrolyser cells have a square duct geometry. For square ducts, a hydraulic diameter needs to be calculated before the resistance coefficient can be determined. The hydraulic diameter can be calculated with equation 4.9, from which the resistance coefficient calculation follows as presented in equation 4.10.

$$D_h = \frac{4 \cdot A_{duct}}{P_{duct}} \tag{4.9}$$

$$\Delta p = f_D \cdot L \cdot \frac{\rho_{elec}}{2} \cdot \frac{u^2}{D_h} = \frac{32 \cdot L \cdot \mu_{elec}}{A^2} \dot{V}_{elec} = K_{duct} \cdot \dot{V}_{elec}. \tag{4.10}$$

where P stands for the wetted perimeter of the cross section of the duct. The resistance coefficient for the electrolyser cell is determined based on a flow between two plates. The pressure drop from which the resistance coefficient is determined can be calculated with the Hagen-Poiseuille equation for flow between two plates, as shown in equation 4.11, with w being the gap width between the plates.

$$\Delta p = \frac{12 \cdot \mu_{elec} \cdot H_{electrode}}{w^3} \cdot \dot{V}_{elec} = K_{plan} \cdot \dot{V}_{elec} \tag{4.11}$$

4.6.2. Electrolyte flow direction.

Based on the dimensions of the electrolysis system, the resistance coefficients can be calculated for the entire system. Figure 4.52 shows a schematic of the electrolysis system with all the points for which the resistance coefficients have been calculated. The calculated resistance coefficients are presented in appendix chapter B table B.2 from highest to lowest.

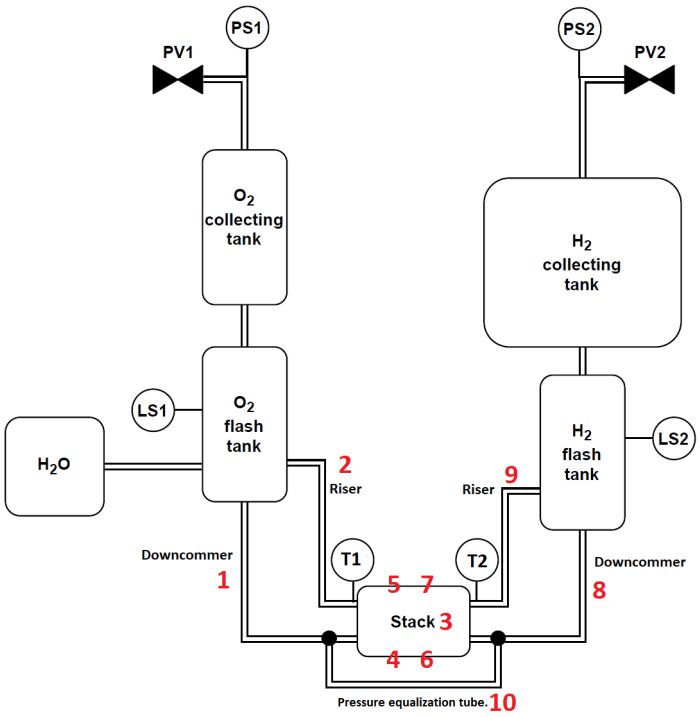

Figure 4.52: Schematic of the electrolysis system with the points presented for which the resistance coefficients were calculated. The points correspond to the numbers and the dimensions for each point can be found in table B.2.

The table gives a clear overview which components in the system have the highest resistance coefficient, which provides insight in which the electrolyte flow direction will go after the opening of the purge valves. If the hydrogen purge valve opens, the pressure will drop in the hydrogen flash tank, resulting in an electrolyte flow. The highest pressure after the opening of the valve is in the oxygen flash tank, so the electrolyte will flow from the oxygen flash tank to the hydrogen flash tank. The resistance coefficient in the oxygen downcomer is lower compared to the summation of resistance coefficients of the riser, and the channels in the electrolyser cell. This means most of the electrolyte will flow through the downcomer to the pressure equalization tube and towards the hydrogen downcomer. However there will also be electrolyte flowing through the electrolyser half cells to the pressure equalization tube, only less due to the higher resistance coefficient. This is contradicting with the visual observation made in chapter 4.5, where a flow was observed from the electrolyser half cell toward the oxygen flash tank when either one of the purge valves opened. This can be seen in figure 4.49, where bubbles and electrolyte can be seen flowing into the entrance of the top channel.

It is assumed that the absence of back flow arises due to the buoyancy force of the generated oxygen bubbles, combined with an unintended design error where the connection of the riser to the oxygen flash tank is made above the electrolyte level in the oxygen flash tank. This ensures that the electrolyte cannot flow through the riser back into the electrolyser half cell. The slugs in the channels and the production of oxygen bubbles avoid back flow. In the model of I. Daniil [9], during the opening of the hydrogen purge valve, electrolyte back flow is expected at the oxygen side, presented in figure 4.53 which shows the flow direction in the electrolysis system during the opening of the hydrogen purge valve. The effect of the bubbles was not taken into account in the model, which explains the prediction of back flow and the absence of back flow seen in the experimental setup.

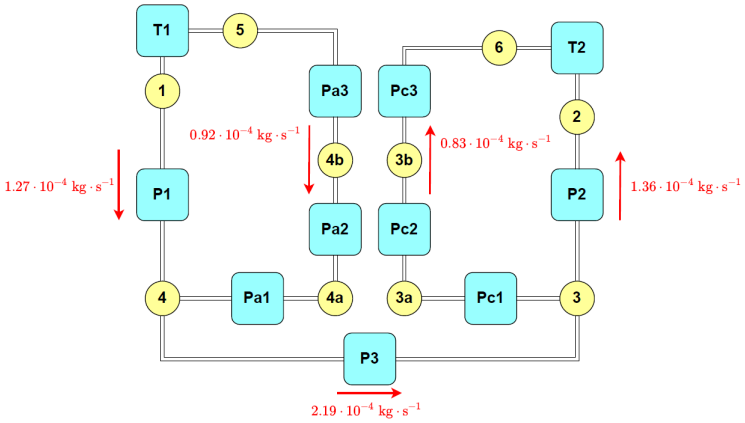

Figure 4.53: Electrolyte flow in a network representing the electrolysis system during main operation, as modelled by I. Daniil. T1 stands for the oxygen flash tank and T2 stands for the hydrogen flash tank. The red arrows indicate the direction of the electrolyte flow, showing back flow at the oxygen side at node 4b. Figure obtained from I. Daniil [9].

From the pressure equalization tube, the hydrogen downcomer has a three times lower resistance coefficient, than the path through the electrolyser half cells to the hydrogen flash tank. Which means three time the amount of electrolyte will flow through the downcomer to the hydrogen flash tank.

For the oxygen side the same principle hold regarding the created pressure difference due to the opening of the hydrogen purge valve. Electrolyte will start flowing from the hydrogen flash tank to the oxygen flash tank through the pressure equalization tube. Due to the oxygen downcomer having a lower resistance coefficient, most of the electrolyte will flow through the downcomer to the oxygen flash tank.

4.6.3. Adaptation pressure equalization tube.

In order to estimate the risk of mixing of electrolyte, that can lead to gas crossover, the volume flow through the pressure equalization tube for the opening of the purge valves needs to be estimated. The volume of oxygen and hydrogen present in the respective flash tanks when the level sensor becomes dry, can be calculated based on the height of the level sensor in the flash tank and the tank dimensions from table 3.1 in chapter 3.2. The gas volume in a flash and storage tanks during operation when the level sensor becomes dry, is presented in table 4.10.

Table 4.10: Gas volume for the oxygen and hydrogen tanks during the moment the level sensors are dry.

Component	Gas volume
Oxygen tanks	196.2 cm^3
Hydrogen tanks	565.5 cm^3

During the opening of the purge valves, the oxygen purge valve opens for 100 ms and the hydrogen purge valve for 50 ms. This leads to a pressure drop of respectively 0.4 bar and 2.7 bar. If isothermal conditions are considered, the change in volume of a gas can be taken from equation 4.12, with κ being the heat capacity ratio shown in equation 4.13. For isothermal conditions, κ equals 1.

$$p \cdot V^{\kappa} = constant. \tag{4.12}$$

$$\kappa = \frac{C_p}{C_V} \tag{4.13}$$

With both equations and the volume of gas estimated in the flash tanks, the increase of gas volume in the flash tank opposite to the opened purge valve can be determined. This is equal to the volume of electrolyte that flows through the pressure equalization tube. The pressure drop of 0.4 bar for the opening of the oxygen purge valve, leads to a hydrogen volume increase of 3.13 cm^3 in the hydrogen flash tank. Similar for the opening of the hydrogen purge valve, does the pressure drop of 2.7 bar lead to an oxygen volume increase in the oxygen flash tank of 10.99 cm^3.

The volume of the pressure equalization tube can be taken from table B.2 and shows to be 2.51 cm^3, which is more than 4 times lower than the volume of electrolyte that flows through the pressure equalization tube when the hydrogen purge valve opens. The 2.51 cm^3 is also lower compared to the 3.13 cm^3 electrolyte that flows to the oxygen side. This shows gas crossover can occur through electrolyte mixing, if the assumption is made that all the electrolyte goes through the pressure equalization tube and the flow is incompressible. If gas is present in the Swagelok tubes, as seen in chapter 4.5 when opening the hydrogen purge valve, impressibility cannot be assumed, since the gas can be compressed. Based on the 4 times large expected electrolyte flow through the pressure equalization tube when opening the hydrogen purge valve, it can be assumed that electrolyte from the oxygen side will reach the hydrogen side.

A solution proposed to solve the gas crossover through electrolyte mixing is the elongation and increase in diameter of the pressure equalization tube. This increases the volume of the tube and cancels the effect of the electrolyte mixing when the purge valves opens. If one looks at equation 4.8, increasing the length of the tube increases the resistance coefficient linear and

increasing the radius decreases the resistance coefficient by the fourth root. For example a using a tube with a length of 40 cm and an inside diameter of 5 cm, present at ZEF, has a volume of 3141 cm^3, which is approximately 285 times the volume that is displaced when the hydrogen purge valve is opened. The resistance coefficient also decreases by a factor of 480, ensuring almost all flow of electrolyte will go through the pressure equalization tube during the opening and closing of the purge valves. It must be said that over time, the electrolyte from the oxygen side will reach the hydrogen side, due to the continuous opening of the hydrogen purge valve during operation and the constant flow of electrolyte toward the hydrogen side through the pressure equalization tube.

4.7. Gas crossover through bottom channels.

During the experiments with the microscope camera at the bottom channel, treated in chapter 4.5.3, bubbles and slugs were observed to enter the electrolyser half cell through the bottom channel after the opening of one of the purge valves. The opening of the hydrogen purge valve resulted in large slugs traveling through the channel, suspected to be oxygen gas that was re-circulated from the oxygen flash tank through the downcomer. The opening of the oxygen purge valve resulted in a smaller slug travelling through the channel, which was suspected to consist of hydrogen gas generated in the 316 stainless steel top plate. Further research was conducted on this phenomena which resulted in two possible cases of induced gas crossover: by production of oxygen at the connector plate and by production of hydrogen at the channels in the top plate. The position where enhanced gas crossover can occur are presented in figure in appendix chapter B in B.14. The red rectangles stand for the production of oxygen at end plate, or the connector plate in the experimental setup, leading to gas crossover of oxygen and the red circles stand for the production of hydrogen in the channels at the top plate, and possibly at the connecting Swagelok tubing, leading to hydrogen gas crossover.

4.7.1. Gas crossover generated at top plate.

In the ZEF electrolyser stack design, does the 316 stainless steel top plate serve as a cathode due to the negative connection to the power supply. This means hydrogen is generated at the surface of the top plate in contact with the electrolyte. Since the channels in the top plate are in connection with the electrolyte, hydrogen is generated at the surface of the hydrogen footer and header but also at the oxygen footer and header, which poses an increase in gas crossover. This has only significance when the leaking currents through the footer and header are significant enough to generate enough hydrogen to pose a risk for gas crossover. Research done by M. Geraedts [17], showed that leaking currents are present in the header and footer channels, and that the voltage over the header and footer was approximately half the total stack voltage. Based on the observed slugs in the bottom channel of the oxygen side of the electrolyser cell, this shows the possibility of gas crossover by production of hydrogen at the channels in the top plate. This phenomena will not be treated in more detail in this thesis report and further research in this phenomena is recommended.

4.7.2. Gas crossover generated at connector plate.

The 316 stainless steel connector plate serves as the connection point for the power supply. A picture of the used connector plate for the experiments, after disassembly of the electrolyser stack, is shown in figure B.16. For a non transparent stack does a stainless steel end plate function as the connection to the power supply. The connector plate does generated oxygen, due its connection to the positive side of the power supply. Since the connector plate is only in contact with electrolyte on the oxygen side of the electrolyser cell, this should not pose a risk of gas crossover. However if one looks closely at the design of the electrolyser discs, the connection to the hydrogen footer and header becomes visible. This is presented in appendix chapter B in figure B.15.

The assumption that oxygen is generated at the contact of electrolyte with the connector plate in the footer and header channel is supported by the circular discoloration on the connector plate, visible in figure B.16. This discoloration takes place when hydrogen or oxygen is generated at the metal surface, and is also observed on the bipolar plate after disassembly, made visible in figure B.17 in appendix chapter B. Discoloration did not occur on the area where oxygen is build up during a flow stagnation cycle.

Based on the above, it can be assumed that oxygen is generated on the hydrogen side, resulting in an increase in oxygen gas crossover. A simplistic model has been made, to estimate the amount of oxygen generated at the surface area of the connector plate in contact with the electrolyte in the footer or header. The model serves only to estimate the possible effect on gas crossover and provide insight in the phenomena. A scenario of the experimental experiments will used to showcase the results of the model. The operating conditions are set at a pressure of 50 bar, a temperature of 41 °C and a current density of 0.2 A/cm^2, which leads to a total voltage of 6.9 V over the electrolyser stack.

First an estimation is made for the voltage over the footer of 3.2 V. Based on the voltage and the dimensions of the footer, such a cross sectional area and length, the current over the channel can be determined with the electrical conductivity. This is done in equation 4.14.

$$I = \frac{\sigma_{elec} \cdot A_{c,footer} \cdot U_{est}}{L_{footer}} = \frac{87 \cdot 1.25 \cdot 10^{-5} \cdot 3.2}{0.036} = 0.1\ A \tag{4.14}$$

here σ stands for the electrical conductivity. Since the footer is in series with connector plate, the current that runs through the connection area of the connector plate and the electrolyte in the footer is the same. The current density over the small area can be calculated and results in 0.77 A/cm^2. The voltage over the area is estimated based on the line fit taken from the IV curve at a high operating pressure and a temperature of 41 °C in chapter 4.2. With the use of the line fit, the voltage over the area can be crudely estimated, as shown in equation 4.15. The constant values can be taken from table 4.4 in chapter 4.2.

$$U_{circ} = U_{rev} + a \cdot log\left(\frac{b + \frac{c}{T} + \frac{d}{T^2} \cdot 0.77 + 1}{e}\right) + \left(\frac{f + g \cdot T}{e}\right) \cdot 0.77 = 3.7\ V \tag{4.15}$$

Finally the total stack voltage should equal the voltage over the channel plus the voltage over the small connection area, as presented in equation 4.16. If this is not the case, by iteration the model will guess the correct voltage over the footer and get tot the correct total stack voltage value.

$$U_{stack} = U_{circ} + U_{est} = 3.7 + 3.2 = 6.9 \tag{4.16}$$

If the equation above gives the correct value for the total stack voltage, the current density over the small circular area can be used to determine the produced oxygen with the use of equation 2.20 from chapter 2.10. The estimated voltage over the footer shows to be slightly lower than half of the stack voltage. This is in line with the research from M. Geraedts, predicting half of the total stack voltage over footer and header due to leaking currents. If the produced oxygen is compared with the produced hydrogen, the gas crossover can be determined. The gas crossover in percentage based on the operating current density is plotted in figure 4.54.

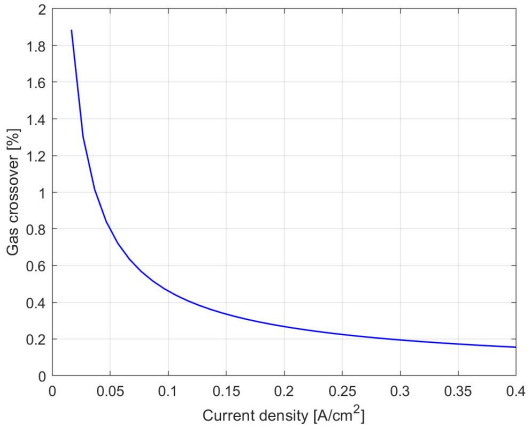

Figure 4.54: Oxygen gas crossover due to the connector plate being in contact with the electrolyte in the footer. Line fit: $g = a \cdot x^b$, with a = 0.07567, b = -0.7854.

At first glance, the graph in figure 4.54 shows that the gas crossover induced by the small circular area does not pose a significant threat for reaching the upper explosion limit when operating at a current density above 0.1 A/cm^2. The highest calculated oxygen gas crossover is 1.88 %, which does pose a threat, for a current density of 0.017 A/cm^2, and decreases significantly with increasing current density, reaching 0.16 % for a current density of 0.4 A/cm^2. However since gas crossover is induced by other mechanics as well, as explained in chapter 2.8, the extra percentage could raise the gas crossover above the UEL. This issue can be solved by simply closing up the hole in the electrolyser disc in the future design, so the end plate is not in contact with the footer and header. A coating of the surface area of the connector plate, or end plate in the micro-plant design, in the footer and header can also solve the problem.

4.8. Velocity measurements of the flow.

The flow in the electrolysis system consist of electrolyte, oxygen and hydrogen flow. The electrolyte flow is in the liquid phase, while the oxygen and hydrogen flow in the gas phase, and partially dissolved in the liquid electrolyte. In order to get more insight in the flow inside the electrolysis system, a UDV device was used to measure the velocity of the electrolyte in different positions in the system. Two positions were chosen for the measurement: the riser tube to the oxygen flash tank and downcomer tube from the oxygen flash tank to the electrolyser stack. The Swagelok tubes where the measurements were taken have an inside diameter of 4 mm and a cross sectional area of 12.57 mm^2. Due to the limited space in the setup, the flow in the pressure equalization tube was not measured. The positions where the UDV transmitter was placed are shown in figure 4.55.

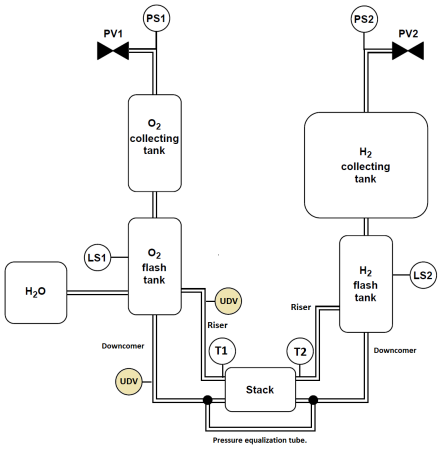

Figure 4.55: Schematic of the electrolysis setup. Placement of the UDV transmitter is visualized by the yellow circles at the riser and downcomer tube on the oxygen side.

4.8.1. UDV measurements.

Measurements were done during the pressure build up to 50 bar at a current density of 0.2 A/cm^2, and at the high pressure operating range for varying current densities. Due to the difficulty in applying the UDV device in the electrolysis system, combined with the viscous gel dripping from the Swagelok tubes, only a few experiments with the UDV succeeded. The successful experiments were conducted at the riser and downcomer for the pressure build at 0.2 A/cm^2. Unfortunately the experiments at the riser and downcomer at a high operating pressure, for various current densities, did result in non representative data.

Riser electrolyte velocity during pressure build up.

The electrolyte velocity was measured a the riser for a pressure build up from 2 to 48 bar at a current density of 0.2 A/cm^2. The UDV device is able to measure the velocity for a certain depth, which allows the see the velocity profile in the circular downcomer tube. The velocity profile in the downcomer tube showed to be parabolic, as can been seen in figure 4.56. The measurement was done after sufficient pipe length, with a length of 10 cm after a corner bend of 90 degrees. In order to determine the average velocity in the downcomer, equation 4.17 can be used.

$$u_{average} = \frac{1}{\pi r^2} \int_0^r u(r) 2\pi r \, dr \tag{4.17}$$

Fluctuations in the velocity measurements were observed in the data, especially during the operation at a lower pressure. Eventually the velocity would reach zero and only have positive peaks in measured velocity, with a few negative peaks at higher pressures. Figure 4.57 shows the velocity measurement at one point in the downcommer during the pressure build up. It only serves to present the fluctuations that are observed in the flow during pressure build up, and the velocity measurement is treated in more detail later in this section.

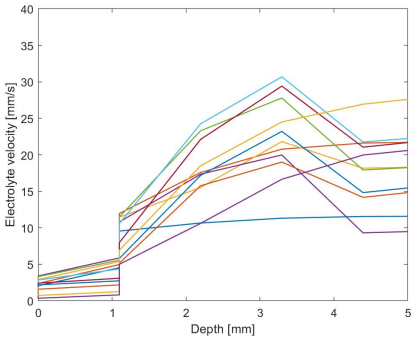

Figure 4.56: Velocity profile in the downcomer tube, measured by the UDV device for 2 seconds. The diameter of the tube, 4 mm, seems to differ from the UDV reading, which shows to be 3.4 mm. The profile shows to be parabolic with the exception of three velocity measurements being a slightly curved line. The average velocity in the channel can be determined with equation 4.17

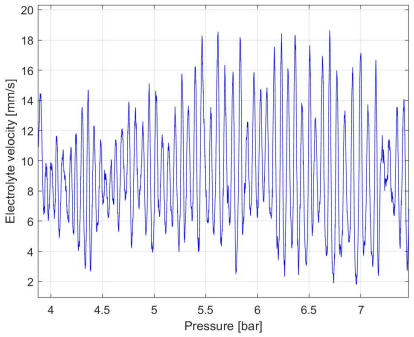

Figure 4.57: Velocity measurement for one point in the downcomer tube during the pressure build up from 2 bar to 48 bar at a current density of 0.2 A/cm^2. Fluctuations in the velocity are clearly visible. The assumption is that the fluctuations come from the large volume of oxygen traveling through the riser, based on the ideal gas law.

In order to minimize the amplitude, to get a clear picture of the electrolyte velocity behaviour over the entire pressure build up, the moving average is plotted for the electrolyte velocity in the downcomer. The moving average was determined with the average of 100 data points for a data set which consisted of 60322 data points. The moving average curve for the electrolyte velocity is presented against the pressure in figure 4.58.

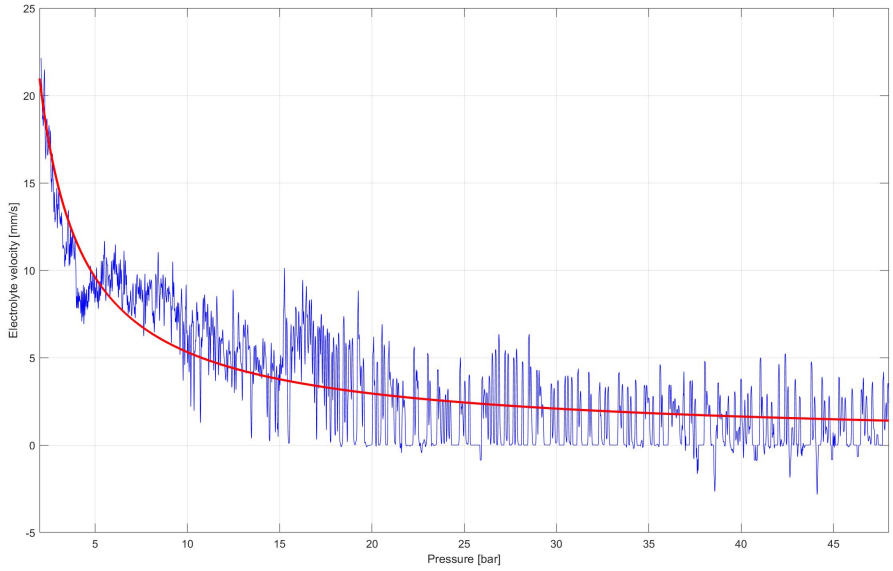

Figure 4.58: Electrolyte velocity measurement at the riser tube on the oxygen side. A moving average curve was made based on the average of 100 data points. A curve fit was made for the average electrolyte velocity, which is represented by the red line, made by using the function $v = a \cdot x^b$ with a = 37.87 and b = -0.8524. The average velocity in the riser starts at 22 mm/s at 2 bar and decreases to 1.4 mm/s at 48 bar.

A first glance at the data shows that the electrolyte velocity through the riser is the highest at low pressures, starting at 22 mm/s at 2 bar and 20 °C, and decreases over time to a velocity of 1.4 mm/s when reaching 48 bar and a temperature of 43 °C. After reaching a pressure of 5 bar, the amplitude of the electrolyte velocity fluctuations starts to increase. It must be noted that these fluctuations are partially damped compared to the raw data of the UDV due to the moving average curve fit. Based on figure 4.58, there are two different time periods in the graph. The first one is before the occurrence of flow stagnation and the second one is during the period in the pressure build up where flow stagnation occurs. Both periods are examined in more detail and are shown respectively in figure 4.59 and 4.60.

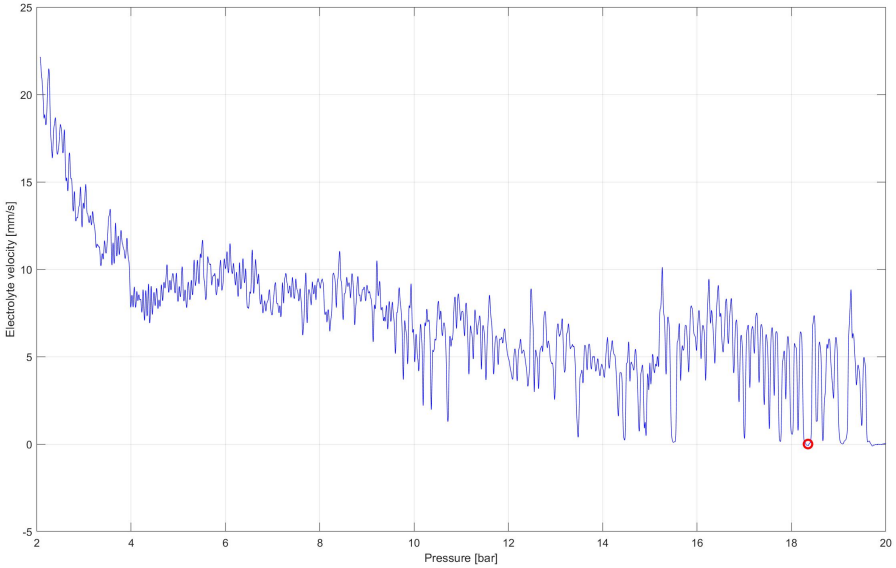

Figure 4.59: Measurement of electrolyte velocity by the UDV device at the riser to the oxygen flash tank from 1 to 20 bar. Flow stagnation occurs for the first time at 18.5 bar, made visible by the red circle in the graph. The electrolyte velocity becomes 0 during flow stagnation.

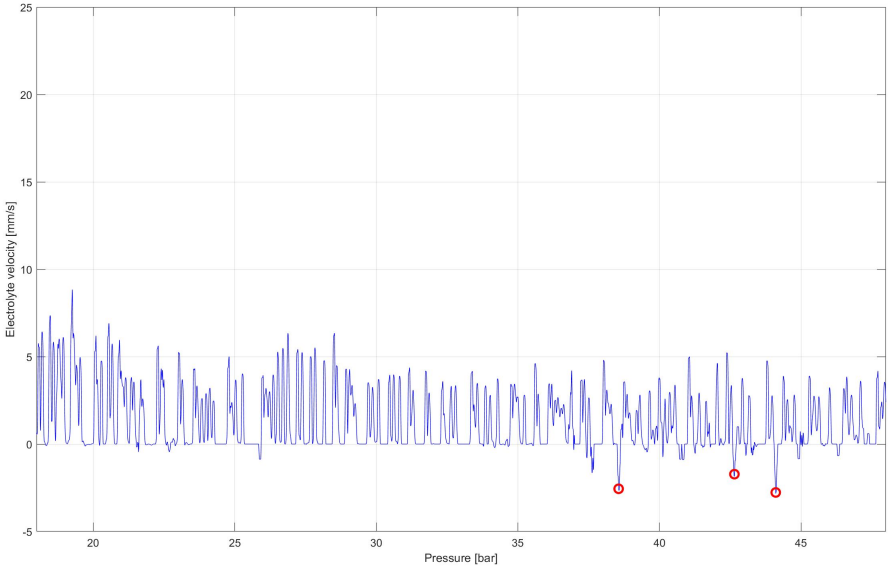

Figure 4.60: Measurement of electrolyte velocity by the UDV device at the riser to the oxygen flash tank from 18 to 48 bar. Flow stagnation starts to occur frequently and back flow is observed with distinct negative velocity peaks, from which three are marked with a red circle.

Figure 4.59 shows that when reaching a pressure of 18.5 bar, visible in the plot by the red circle, the electrolyte flow through the riser starts to stagnate by reaching a velocity of 0 mm/s from time to time. This is in line with the microscope camera experiments in chapter 4.3.1 and chapter 4.3.4. An interesting observation is that at certain points in the graph the velocity shows to be negative, meaning the electrolyte flows in the opposite direction from the flash tank to the electrolyser cells. This can be seen in figure 4.60 and is highlighted for three negative velocity peaks by three red circles. These negative peaks occur for the first time around 22 bar and appear more frequently after reaching 35 bar while also increasing in velocity. The peaks are not connected to the opening or closing of either one of the purge valves. Figure 4.61 shows a zoom onto the electrolyte velocity for a pressure around 32 bar. Multiple flow stagnation cycle can be clearly seen and identified by the periods where

the electrolyte flow is stagnant and shows to have a velocity of 0 mm/s. In figure 4.62, two peaks with a negative electrolyte velocity are shown, implying back flow of electrolyte into the electrolyser cell. This is not observed on the corresponding video footage made at the top channel during the experiments. The assumption is made that the occurring back flow of electrolyte goes through the first electrolyser cell in the electrolyser stack, being the closed to the top plate. This due to being the shortest path to the pressure equalization tube through the stack. Since this cell was not filmed, back flow was not observed during the visualization experiments.

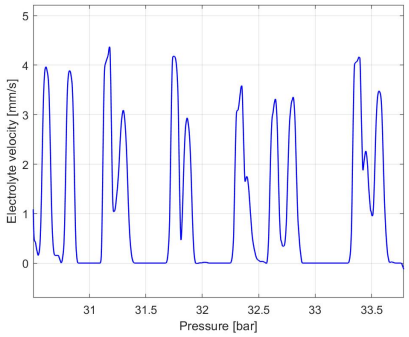

Figure 4.61: Zoom in on the electrolyte velocity during the periodic occurrence of flow stagnation. Flow stagnation occurs when the electrolyte velocity becomes zero.

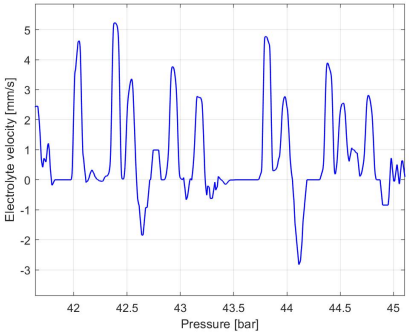

Figure 4.62: Observed back flow during operation at higher pressures in the electrolyte velocity measurement. It is assumed that back flow can occur through the first electrolyser cell, which cannot be observed with the visualization equipment.

UDV at downcomer during pressure build up.

The velocity in the downcomer was measured during pressure build from 13 bar to 50 bar, at a current density of 0.2 A/cm^2. Unfortunately, the software from the UDV device crashed during operation and had to rebooted and the velocity measurement started at 13 bar. Due to a limited time frame and a lot of unrepresentative data before, the experiment was continued when the data looked representative. The electrolyte velocity data also showed to fluctuate, as seen with the data at the riser, and a moving average curve fit was applied to the data, based on the average of 100 data points. The moving average of the electrolyte velocity in the downcomer is shown in the graph in figure 4.63 with a power curve fit through the data to represent the average electrolyte velocity.

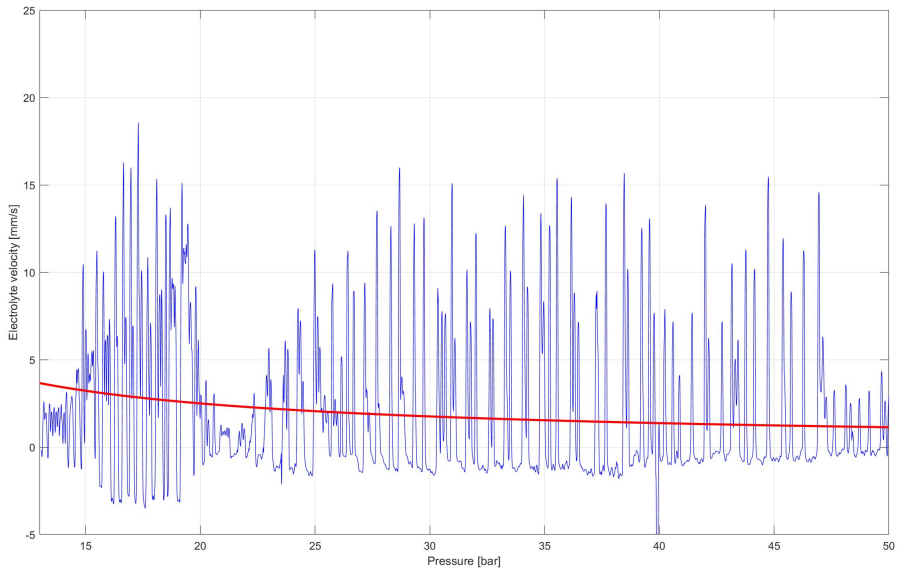

Figure 4.63: Measurement of electrolyte velocity by the UDV device at the downcomer from the oxygen flash tank to the T junction of the pressure equalization tube and the electrolyser stack. Positive direction electrolyte velocity means the electrolyte flows from the oxygen flash tank to the pressure equalization tube and the electrolyser stack. Negative electrolyte velocity is observed, which occurs during flow stagnation in the top channel. On average, the electrolyte flows from the oxygen flash tank to the pressure equalization tube and the electrolyser stack. This can be seen with the curve fit through the data, represented with the red line. The curve fit is made by using the function $v = a \cdot x^b$ with a = 37.49 and b = -0.9179.

According to the temperature sensor data, visualization video footage and the UDV data at the riser, flow stagnation starts occurring for the first time between 18 and 20 bar. The UDV data at the downcomer shows a decrease in electrolyte velocity amplitude at 20 bar, which increases afterwards reaching a steady amplitude at 27 bar. The amplitude decreases again at a pressure of 47 bar. The link to flow stagnation occurring can be made based on the negative peaks of electrolyte velocity seen after reaching 20 bar, which are comparable to the flow stagnation occurring at the top channel. A zoom onto some of the peaks are shown in figure 4.65. The negative peaks in electrolyte velocity relate to an electrolyte flow towards the oxygen flash tank from the T junction connected to the pressure equalization tube and the electrolyser stack. This contradicts with the expected electrolyte flow direction, as explained in chapter 3.2, which is assumed to flow from the oxygen flash tank to the T junction during operation when both purge valves are closed.

Before the occurrence of flow stagnation, the electrolyte velocity fluctuates with shorter periods and lower negative peaks. It is assumed that this behaviour comes from the higher volume of oxygen bubbles being produced at lower pressures.

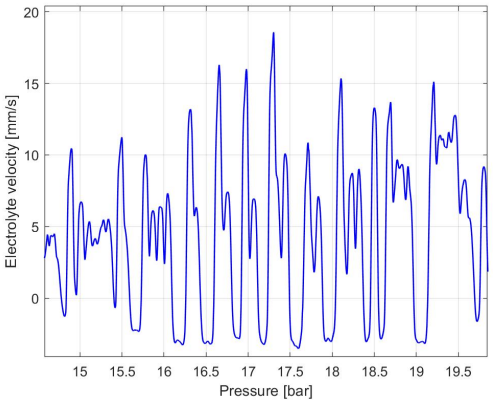

Figure 4.64: Negative peaks in electrolyte velocity observed before stagnation of the flow occurring.

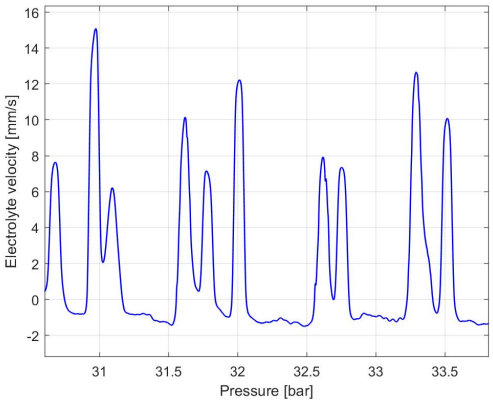

Figure 4.65: Negative peaks of electrolyte velocity observed during flow stagnation in the riser tube.

It is assumed that the negative electrolyte peaks occur due to flow stagnation occurring at the top channels on the oxygen side. Under normal operation, it is expected that pressure in the oxygen flash tank increases at a higher rate that the pressure in the hydrogen flash tank, as explained in chapter 3.2. This leads to a decrease in electrolyte level at the oxygen flash tanks, and an increase in gas pressure. Due to oxygen gas being held in the electrolyser cells and no flow stagnation occurring at the hydrogen side, the gas pressure in the hydrogen flash tank increases at a higher rate, inciting a flow from the hydrogen side to the oxygen side. This can be seen in figure 4.66. When the flow stagnation at the top channels on the oxygen side is solved, a peak in positive electrolyte velocity is observed in the UDV data, comparable to the expected flow behaviour during operation with both purge valves closed, represented in figure 4.67.

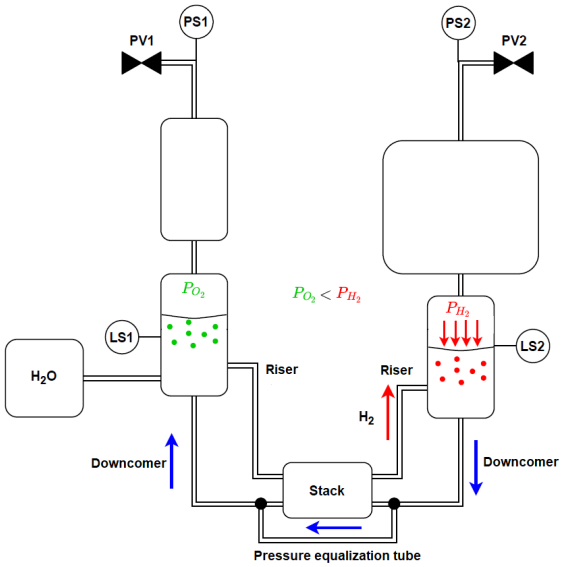

Figure 4.66: Schematic of the electrolysis setup. The figure shows the behaviour of the electrolyte flow during operation when flow stagnation occurs, based on the pressure difference in the flash tanks.

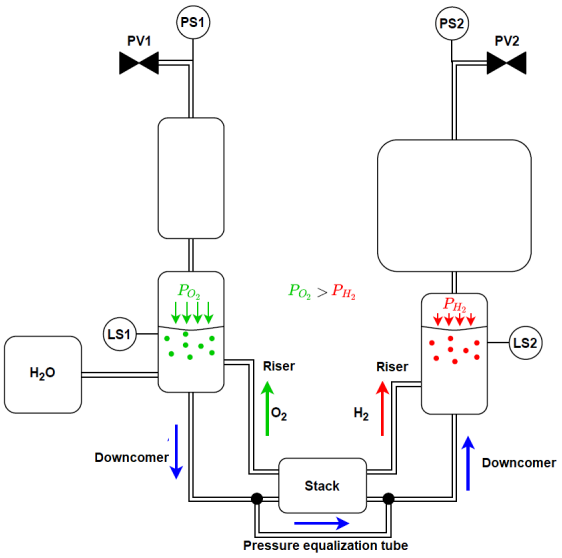

Figure 4.67: Schematic of the electrolysis setup. The figure shows the expected behaviour of the electrolyte flow during normal operation based on the pressure difference in the flash tanks.

The observed electrolyte velocity direction in the downcomer, and in the riser, has a negative impact on the cooling of the electrolyte stack. Continuous re-circulation of the electrolyte is required for an efficient cooling, especially with a temperature regulation system using for example a heat exchanger implemented in the downcomer. Since it is assumed that flow stagnation will also occur in a stack consisting of more electrolyser cells, a problem Since, according to the UDV data at the riser, no electrolyte flow is observed towards the oxygen flash tank during a flow stagnation cycle, electrolyte is expected to flow through the bottom channels in the electrolyser cells towards the T junction with the pressure equalization tube. I. Daniil suggested possible back flow in his research, however this was not observed during the visualization experiments. Based on the findings in this chapter, the assumption is made that back flow occurs through the bottom channels during a flow stagnation cycle, even though it is not observed in the visualization data probably due to poor resolution and frame rate of the video footage. However the electrolyte velocity is low and oxygen bubbles are not flowing out of the electrolyser cell through the bottom channels, which can be observed and was not seen in the video footage at the bottom channels.

4.8.2. Production rate and oxygen gas velocity.

The production of oxygen, and hydrogen, at the electrodes can be calculated with the use of the equations in chapter 2.10. This is under the assumption that all of the applied current goes into producing the two gasses at the electrodes. The production of oxygen a the connector plate surface is also neglected. For operating under the conditions for the electrolysis, at a pressure of 50 bar and a temperature of 43 °C, the production of oxygen and hydrogen can visualized in figure 4.68 for a varying current density. The effect of temperature on the production rate of oxygen is shown in figure 4.69. Both equations are based on the ideal gas law as explained in chapter 2.10.

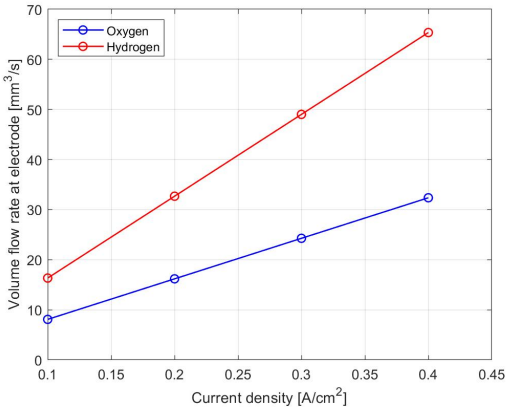

Figure 4.68: Production of oxygen and hydrogen at the electrodes for a temperature of 43 °C

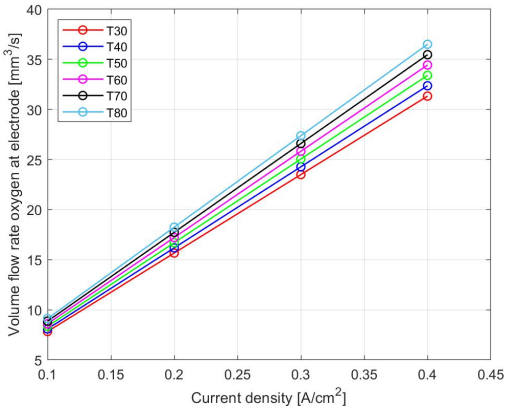

Figure 4.69: Production of oxygen and hydrogen at the electrodes for a pressure of 50 for varying temperatures.

The velocity of oxygen gas in the electrolysis system can be estimated on the amount of oxygen produced at the electrode surfaces, and the cross sectional surface area of the channels and the tubes in the system. The calculation of the velocity through a channel can be expressed with equation 4.18 where the cross sectional area of the channels can be taken from table B.2 in chapter 4.7.

$$u_{channel} = \frac{\dot{V}_{O_2}}{A_{channel}} \tag{4.18}$$

With equation 4.18, the velocity can be calculated for the produced oxygen gas through one top channel and through the riser, for an operating pressure of 47-50 bar and a temperature of 43 °C. The oxygen gas travelling through the riser is composed of the entire produced oxygen quantity in the electrolyser stack. The calculation for the velocity is based on the average duration of flow through the top channels, which has been determined in chapter 4.3.3, and the produced oxygen during that time period. The time it takes for the large oxygen bubble to leave the electrolyser cell and its effect on the velocity has been taken out of the calculation. The plots for the velocity in one top channel and in the riser are shown in figure 4.70. The velocity for the large oxygen bubble can be determined based on the time it takes for the volume of the large oxygen bubble to leave the electrolyser cell through the channel, and the channel dimensions. The calculation is shown in equation 4.19. The velocity is plotted in figure 4.71 for the top channel and for the riser. In the equation, $t_{Lbubble}$ stands for the time it takes for the large oxygen bubble to completely travel through the channel.

$$u_{Lbubble} = \frac{V_{O_2}}{A_{channel} \cdot t_{Lbubble}} \tag{4.19}$$

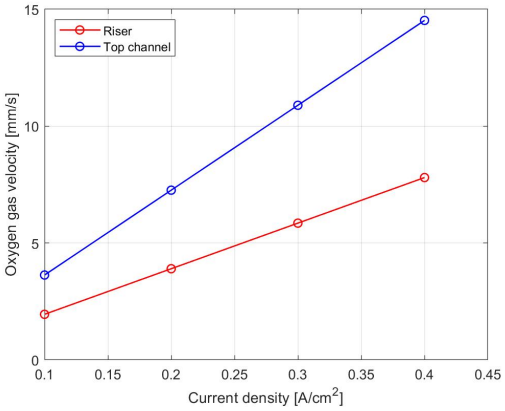

Figure 4.70: Average velocity of oxygen through the top channel en through the riser.

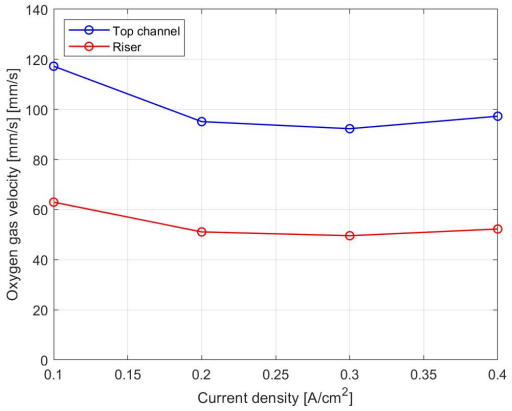

Figure 4.71: Average velocity of the large oxygen bubble through the top channel en through the riser.

4.8.3. Flow regime map.

Based on the electrolyte velocity measured by the UDV device in the riser, in the section above, and the calculated velocity of oxygen through the top channel, a flow regime map can be devised for the flow through the top channels of the electrolyser cells. The observed flow regimes through the top channel from chapter 4.3.1 can be linked to the velocity for the liquid electrolyte and the oxygen gas based on the current density. Electrolyte velocity measured by the UDV device for a current density of 0.2 A/cm^2 in the riser channel needs to be translated to the velocity in one of the three top channels. The velocity can be used to calculate the mass flow with equation 4.20, where the cross sectional area for the riser comes from table B.2 in chapter 4.6. If dived by three, the mass flow of electrolyte through the top channel is determined and the velocity through one top channel can be calculated, as shown in equation 4.21.

$$\dot{m}_{riser} = u_{riser} \cdot \rho_{elec} \cdot A_{riser} = 0.005 \cdot 1300 \cdot 1.25 \cdot 10^{-5} = 8.17 \cdot 10^{-5}\ kg/s \tag{4.20}$$

$$u_{topchannel} = \frac{\dot{m}_{riser}}{3 \cdot \rho_{elec} \cdot A_{topchannel}} = \frac{8.17 \cdot 10^{-5}}{3 \cdot 1300 \cdot} = 9.30\ mm/s \tag{4.21}$$

Since the electrolyte velocity is only measured by the UDV device for a 0.2 A/cm^2 operation, the velocity for the current density range used during the experiments is linked to the velocity of the oxygen gas at the corresponding current density. This means that for a current density of 0.1 A/cm^2, the electrolyte velocity is assumed to be half of the velocity when operating at a current density of 0.2 A/cm^2. It must be noted that this a crude method, which is used only to provide insight in a flow regime map for KOH electrolyte and oxygen gas flow through a square duct. In table 4.11, the electrolyte velocity and oxygen gas velocity with the corresponding flow regime through the top channel, based on the corresponding current density, are shown.

Table 4.11: Electrolyte liquid velocity and oxygen gas velocity with corresponding current density and flow regime for flow through a top channel.

Current density [A/cm^2]	Gas velocity [mm/s]	Electrolyte velocity [mm/s]	Flow regime
0.017	10.90	13.95	Bubbly flow
0.1	7.26	9.30	Plug flow, slug flow
0.2	3.63	4.65	Slug flow, plug flow
0.3	0.60	0.78	Slug flow

Based on the data presented in table 4.11, a flow regime line can be devised for the flow through the top channel of the electrolyser cells. In order to make a flow regime map, an estimated guess is made based on the information and flow regime map in chapter 4.3.1, and the video footage. The flow regime map is presented in figure 4.72

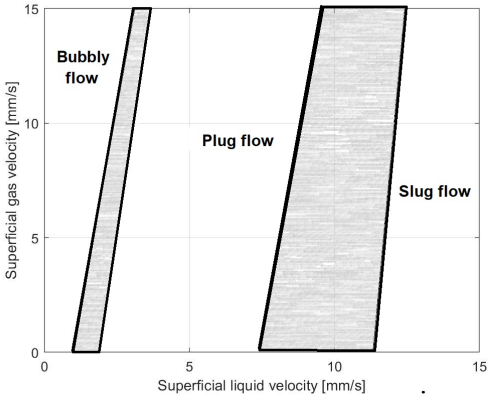

Figure 4.72: Flow regime map for flow through the top channel of the electrolyser cell. Due to the superficial liquid and superficial gas velocity being results from a set current density value, only a flow regime line could be obtained at first. Based on the information and flow regime map in chapter 4.3.1, and the video footage, an estimated guess is made to make a flow regime map. The gray areas in the flow regime map present the transition area between the specific flow regimes on the left and the right of the area.

4.9. Leakage of pressure at the hydrogen side.

The visualization experiments done at the entrance of the top channel, discussed in chapter 4.3.4, showed that a small pressure leak at the hydrogen side had a positive effect on the occurrence of flow stagnation when operating at a current density of 0.017 A/cm^2. The small pressure leak on the hydrogen side can be compared with the opening of the hydrogen purge valve, with the difference being the gradual reduction of pressure. Opening of the hydrogen purge valve showed to have a positive effect by solving flow stagnation occurring at that specific moments. Due to the pressure drop being significantly larger compared to a small pressure leak, only when operating at 0.017 A/cm^2 a positive effect is seen regarding the solving of flow stagnation. Based on the observations from the UDV data in chapter 4.8.1, the stagnation of the flow has a negative impact on the electrolyte re-circulation and the electrolyte flow direction on the oxygen side. In future designs, this effect has to be taken out and the positive effect from the opening of the purge valves implemented at a gradual level. The use of capillary tubes at the purge valves on the flash tanks should results in a gradual reduction of pressure, which should have a positive effect on the flow and flow stagnation when regarding the UDV data from chapter 4.8.1 and the data for opening of the purge valves in chapter 4.5.

4.10. Visualization of oxygen bubbles.

The generation of oxygen bubbles at the electrode surface in the electrolyser cell was observed for a varying current density range and for low and high pressure operation. The same operating current densities were used as with the experiments for comparing the effect of low and high pressure operation on the overpotential at the electrolyser cells. Operation at low pressure was done for a pressure range between 1.8 and 3 bar, and operation at high pressure was done at 47-50 bar. The goal of the experiments was to observe the bubble size visible on the video footage at the bottom of the electrode and at the top of the electrode and visualize the effect of operating at a higher pressure compared to operating at a lower pressure, and compare the findings with literature. Unfortunately, due to the poor resolution and frame rate of the microscope camera, bubble tracking programs used were not able to track the individual bubbles and determine their size. The perpendicular camera view on the electrode, and the bubble curtain, also increased the difficulty of characterising the bubbles. The only option left was to determine the bubble characteristics by hand, which was not done due to the time consuming process and the time left for the thesis. In the end, only interesting phenomena occurring at the electrodes are analysed in this thesis. The analysis is done in appendix chapter A.10.

4.11. Heat exchanger implementation.

As mentioned in chapter 1.3, is it desired to implement a temperature regulation system in the electrolysis system. At the moment, the temperature is an uncontrolled variable, that needs to be kept in check in order to remain the structural integrity and to

prolong the life time of certain components of the electrolyser stack with the transparent add on. In future designs, a temperature regulation system allows for the possibility of conducting precise experiments. A solution proposed is the implementation of a heat exchanger in the downcomer on both the oxygen side and the hydrogen side, to cool down the electrolyte that is re-circulated into the electrolyser stack. The cooled down electrolyte serves to lower the temperature in the electrolyser stack back to a desired level when the temperature increases above a certain level. An air cooled finned tube heat exchanger has been chosen to be implemented, based on several finned tubes being present at ZEF. An example of one of the finned tubes is shown in figure 4.73. Fans are suggested to be used in addition with the finned tube heat exchanger to enhance the cooling capacity. A numerical model has been made, to represent a finned tube heat exchanger implemented on of the downcomers of the electrolysis system. The model is presented in appendix chapter A.7.1.

Figure 4.73: Representation of a finned tube present at ZEF, which will be used in the modelled heat exchanger.

The model is based on operation at a set pressure of 50 bar, a variable current density that results in certain temperatures in the electrolyse stack and an electrolyte of 30 wt% KOH. Thermophysical properties for the electrolyte were taken from research done be D. Le Bideau et al. [29], presented in appendix chapter A.1. The equations used in the model were taken from VDI-Gesellschaft Verfahrenstechnik und Chemieingenieurwessen (2010) [4] and Mills, A.F (2013) [35].

4.11.1. Model results.

The model has been run, and the results are presented in this chapter. The model was first used to check the heat exchanger length necessary for the experimental setup, which uses the three cell electrolyser stack with the transparent add on. Assumptions made for the model are that there is no flow stagnation occurring, as in I. Daniil's model, and no bubbles or oxygen gas is re-circulated during the operation of the electrolyser stack. The increase in diameter of the downcommer due to the finned tube parameters, resulting in a lower mass flow rate which allows for better cooling, is not implemented in the model. The operating conditions for the model were a pressure of 50 bar, a current density of 0.3 A/cm^2 and an ingoing temperature and constant mass flow through the heat exchanger of respectively 90 °C and $0.21 \cdot 10^4$ kg/s. The high temperature is chosen to check the performance of the heat exchanger on a sudden increase in temperature. The mass flow velocity is taken from the model of I. Daniil. Since the temperature is desired to stay below 60 °C due to the transparent add on, the model was used to cool the electrolyte stream to 40 °C. The heat transfer coefficient between the air and the finned tube, enhanced by the fans, was set at 40 W/m^2 K.

The model shows that a heat exchanger length is required of 11 cm for the oxygen side, which means in order to implement a heat exchanger in the electrolysis system the height of the flash tanks needs to be raised. If the fans are modeled to be less efficient, with a heat transfer coefficient of 20 W/m^2 K, the heat exchanger length needs to be 15 cm. In the case of no fans being present, the heat transfer coefficient shows to be 2.8 for the stagnant air surrounding the heat exchanger. This leads to a necessary heat exchanger length of 40 cm.

The mass flow of the electrolyte in the downcomer increases when the stack consist of more electrolyser cells, due to the increased buoyancy driving force by the higher production rate of hydrogen and oxygen. For the eventual electrolyser stack in the ZEF micro-plant, 18 electrolyser cells are present. This will result in more heat being produced and a corresponding increase in mass flow in the downcomer. If the assumption is made that from 3 to 18 cells results in a 6 times as high mass flow, the mass flow in the downcomer is $1.27 \cdot 10^4$ kg/s. The outgoing temperature is estimated at 90 °C, based on operation of a 18 cell electrodeless stack by B. Mulder [36]. If a heat transfer coefficient of 40 W/m^2 K is assumed, a heat exchanger length of 0.29 cm is required. Less efficient fans with heat transfer coefficient of 20 W/m^2 K, will require a heat exchanger length of 38 cm. This results in the necessity of longer downcommer tubes if the heat exchanger is planned to be implemented in the electrolysis system. The flash tanks in the system need to be raised in order to lengthen the downcommer tubes. When implemented, the heat exchanger can cool down the flow of electrode to any desired temperature level, even with a sudden outgoing temperature of 90 °C.

4.12. ZEF electrolysis system flow characterisation map.

Based on the analysis of the experimental data and calculations made in this chapter, a flow characterisation map can be devised for the electrolysis system. The map shows the occurrence of flow stagnation and the different observed flow regimes through the top channel for an operating current density. The implementation of a temperature regulation system is not considered in the ZEF electrolysis system flow characterisation map. In figure 4.74 the flow characterisation map is shown.

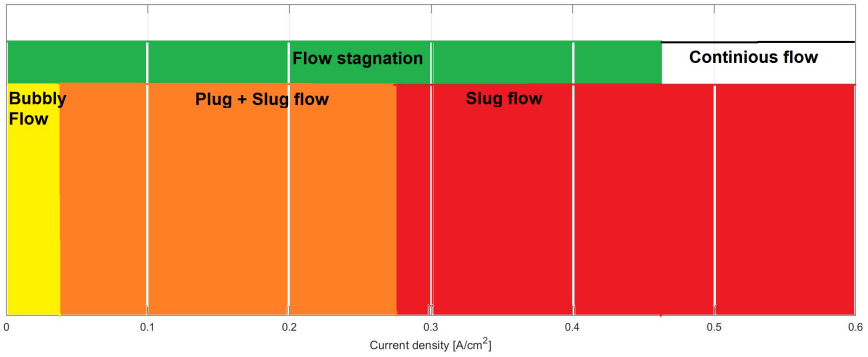

Figure 4.74: ZEF electrolysis system flow characterisation map. The map shows for which current densities flow stagnation occurs,

5

Conclusions & Recommendations.

The final chapter of this report summarizes the findings from the experimental research, described in the experimental results and analysis chapter, and tries to answer the research questions proposed at the start of the thesis. The thesis questions are itemized below for convenience.

- **Does the characterisation of the flow and bubble phenomena, by a flow characterisation map, in the electrolysis system impose operational restrictions for the electrolyser stack, regarding efficient and safe operation?**
- **Does the influence of the pressure control system lead to unexpected or undesired flow behaviour inside the electrolysis system?**
- **Can an effective temperature regulation system be modeled and eventually installed for the electrolyser stack, based on the observation and characterisation of the flow inside the electrolysis system?**
- **Does operating at a low pressure and a low current density lead to the same bubble behaviour as operating at a high pressure and a high current density?**

Subsequently recommendations are provided to improve the operation of current ZEF electrolysis system. The recommendations are based on the new insights about the ZEF electrolysis system, obtained during the experimental phase and the analysis of the experimental data, and on the drawn conclusions.

5.1. Conclusions

When regarding the research question proposed in the first chapter, the last question could not be answered in this thesis due to the bubble behaviour not being characterised. Since this research question was added as a more scientific question, recommendations are provided in order to answer this question in future research. The main conclusions of this research project are itemized below.

- Operating at low pressures, 2-3 bar, was compared with operating at high pressure, 47-50 bar, for a varying current density range and the same temperature level. The results showed that the difference in overpotential is almost negligible, when operating at the same current density and temperature, and operating at higher pressures does not lead to a more efficient operation regarding the applied voltage to the electrolyser stack for a same current density range. A curve fit was made to estimate the overpotential as a function of temperature and current density, which shows to provide representative curve fits for operating at a high pressure.
- Different flow regimes were observed at the top channel of the electrolyser stack for a varying current density range. The main flow regimes were determined and the observed slugs through the channel counted and the observed length and volume compared with the theoretical produced volume of oxygen, which showed to be in line.
- Experiments with the microscope camera and the GoPro camera showed that the flow through the top channel of the electrolyser cells on the oxygen side stagnates, during a flow stagnation cycle, when operating at the desired pressure range of 47-50 bar. The stagnation of the flow occurs due to the coalescence of oxygen bubbles before the entrance of the top channels in the electrolyser cells. The driving force of the coalescent bubble, the buoyancy force, is overruled by the surface tension force which needs to be overcome before the bubble can enter the channel. Calculation were made to validate this assumption and the outcome shows that the surface tension of the large coalescent bubbles in the main reason flow stagnation occurs. Increasing the operating current density showed to decrease the duration of a flow stagnation cycle, by increasing the production of oxygen at the electrode surface, resulting in a faster increase of buoyancy force. If operating at or above a current density of 0.5 A/cm^2 flow stagnation was not observed. This means that the continuous presence of oxygen gas in the riser channel has positive effect on the occurrence of flow stagnation. The higher current density however results in an increase in the overpotential for an electrolyser cell, which lowers the efficiency and does lead to an increase in operating temperature.
- When operating at higher current densities, above 0.5 A/cm^2, the combination with flow stagnation occurring resulted in the degradation and burning of a Zirfon diaphragm in the middle electrolyser cell. This phenomena requires further research but shows the possible risks of operating with flow stagnation occuring on the oxygen side.

- The model made by I. Daniil predicted electrolyte back flow on the oxygen side of the electrolyser stack. Visualization of the flow in the electrolyser cells showed that back flow does not occur during operation in the visualized cell, assumed due to the generation of gas bubbles and slugs being present in the channels. The UDV data showed a few negative electrolyte velocity peaks, suggesting back flow does occur but probably only on the first electrolyser cell
- The effect of the pressure control system was investigated with the use of the microscope camera and the UDV device. The microscope camera showed the positive effect of the opening of the purge valves on occurring flow stagnation, which positive effect showed to be comparable to a small pressure leak at the hydrogen side leading to a better flow through the top channel at lower current densities. Gas crossover does occur through the pressure equalization tube when both of the purge vales are opened during operation at high pressure.
- The heat exchanger model showed that, with simple heat exchanger made out of a finned tube and installed in the downcomer tube, a temperature regulation system can be implemented in the electrolysis system. The necessary length for the heat exchanger results in that the flash tanks need to be raised compared to the electrolyser stack. It is assumed that is this will have a positive impact on the occurrence of flow stagnation due to oxygen gas being in the channel for a longer period of time.
- Enhanced gas crossover was noticed, based on observations made at the bottom channel of the electrolyser cell during the opening of the purge valves. The gas crossover occurs due to the design of the electrolyser stack and the connection of the header and footer channels to the positive anode and negative cathode for respectively the hydrogen side and the oxygen side.
- The velocity in the riser and downcomer tube was measured with a UDV device during pressure build up to 50 bar at a current density of 0.2 A/cm^2. Flow stagnation was observed in the riser and hints were seen of possible back flow. The downcomer electrolyte flow direction showed to be counter intuitive compared to expected operation when a flow stagnation cycle occurred. The build up of oxygen gas in the electrolyser cells blocks the top channel during operation, leading to a electrolyte flow the hydrogen side to the oxygen side when the flow is expected to go the other way.

5.2. Recommendations.

In this section, recommendations are proposed to help improve the future design of the ZEF electrolysis system and the electrolyser stack.

- Based on the observation of large slugs entering the electrolyser cell through the bottom channel, after the opening of the hydrogen purge valve, it is desired that the electrolyte flow velocity in the system does not increase drastically during the opening of the hydrogen purge valve. This leads to an increase in gas crossover due to electrolyte mixing of electrolyte flowing through the pressure equalisation tube. Since the increase in velocity is caused by the immediate pressure drop, a slower extended pressure drop is preferred. The implementation of capillary tubes on both the flash tanks, should solve this problem. This also limits the sudden pressure difference over the diaphragms in the electrolyser cells and the gradual pressure drop has a positive effect on the occurrence of flow stagnation.
- In order to solve the occurrence of a flow stagnation cycle, the channel width of the top channel could be increased. This lowers the surface tension force necessary to be overcome by the buoyancy force. The leaking currents should be kept and calculations are necessary.
- The height between the flash tanks and the electrolyser stack should be increased, to allow for implementation of a heat exchanger. This also ensures the residence time of the oxygen in the riser increases which has a positive effect on the occurrence of flow stagnation, due to a constant driving force of the buoyancy force increasing the electrolyte recirculation. The increase in downcomer diameter due to implementing a finned tube heat exchanger does also result in a lower resistance coefficient, allowing the electrolyte to more easily flow towards and through the pressure equalization tube from both of the flash tanks, instead as back flow through the electrolyser cells.
- Gas crossover can occur through the pressure equalization tube in the form of electrolyte mixing. The opening of the purge valves enhances this effect, especially the hydrogen purge valve. In order to solve this problem, the implementation of a longer and wider pressure equalization tube is proposed. This increases the volume of the tube, which counters the amount of volume displaced by the opening of the purge valves. The lower resistance of the pressure equalization tube also ensures that during the opening of either one of the purge valves, most of the electrolyte will flow through the pressure equalization tube and due to the generation of gas in the electrolyser cells almost no back flow will be seen in the electrolyser cells.
- In order to prevent the enhanced gas crossover of oxygen due to the connector plate or end plate being in contact with the electrolyte in the footer and header, the hole in the electrolyser disc should be closed for the disc against the end plate in the future designs. A coating can also be applied on the metal surface area in the header or footer.
- The enhanced gas crossover of hydrogen, occurring at the top plate footer and possibly some length of Swagelok tubing connected to the top plate, due to leaking currents should also be addressed. A possible solution is applying a high resistance coating in the Swagelok tubing and in the channels of the top plate. This increase in resistance should ensure the leaking current does flow through the first electrolyser cell before the top plate, not posing a risk to gas crossover.
- Ensure the diaphragm is pressed tight between both of the electrodes, to prevent bubbles being generated in between the electrodes and the diaphragm.
- In order to have more insight in the height of the electrolyte level, multiple level sensors should be installed in both flash tanks. If for example three level sensors are installed, the bottom one could be the trigger point for the opening of a purge valve while the top level sensor can indicate how much electrolyte in is the system when operation starts. It ensures the electrolyte concentration in the system can be determined more correctly and shows how much water needs to be added after the bottom level sensor becomes dry. The middle level sensor allows to determine the time left before water needs to be added to the system.

A

Appendix

A.1. Thermophysical properties of 30 wt% KOH electrolyte.

In this section, the thermophysical properties with respect to different temperatures for alkaline water electrolysis are presented, for an electrolyte with 30 wt% KOH. The thermophysical properties are the the electrical conductivity, density, viscosity and specific heat capacity. The graphs for thermophysical properties shown in this chapter come from the work of D. Bideau et al. [29]. The effect of pressure on each of the properties with respect to the operating pressure on the electrolysis system is treated.

A.1.1. Electrical conductivity.

The influence of temperature on the electrical conductivity of 30 wt% KOH at atmospheric pressure is presented in figure A.1. The influence of pressure was studied by Hamann et al. [18], who observed an increases in electrical conductivity of KOH with increasing pressure. The research concluded that there was a 29% increase in electrical conductivity of KOH regarding a pressure increase from 1 bar to 75000 bar. Other research conducted by Gancy et al. [16] concluded that the electrical conductivity of aqueous potassium chloride electrolytes increased only 15% between 1 bar and 2000 bar, when operating at a temperature of 5 °C, and approximately 1% when operating at 80 °C. Based on these two studies, it can be assumed that a pressure increase to 50 bar for the operating temperatures of the electrolyser stack does not lead to a difference in electrical conductivity.

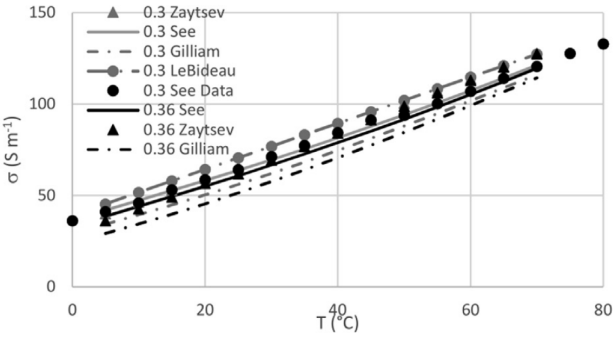

Figure A.1: Electrical conductivity of 30 wt% KOH dependence of temperature at atmospheric pressure. [29].

A.1.2. Density.

The influence of temperature on the density of 30 wt% KOH at atmospheric pressure is presented in figure A.2. The general assumption is that water is incompressible and pressure does not influence the density. However according to D. Bideau et al. [29] does the density of water increase with 2% when increasing pressure from 1 to 200 bar. Nevertheless will the effect of pressure on the density be neglected due the small effect when operating at a pressure of 50 bar.

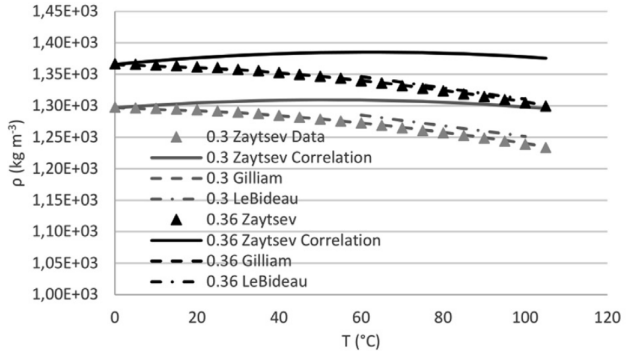

Figure A.2: Density of 30 wt% KOH dependence of temperature at atmospheric pressure. [29].

A.1.3. Viscosity.

The influence of temperature on the viscosity of 30 wt% KOH at atmospheric pressure is presented in figure A.3. Since water is not incompressible, the viscosity increases with increasing pressure. For convenience, the assumption is made in this report that water is incompressible and the effect of pressure on viscosity in negligible.

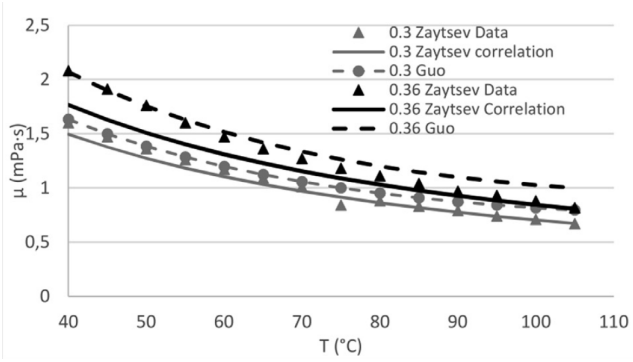

Figure A.3: Viscosity of 30 wt% KOH dependence of temperature at atmospheric pressure. [29].

A.1.4. Specific heat.

The influence of temperature on the specific heat of 30 wt% KOH at atmospheric pressure is presented in figure A.4. The assumption made above, that water is compressible, results in that the specific heat is constant with increasing pressure.

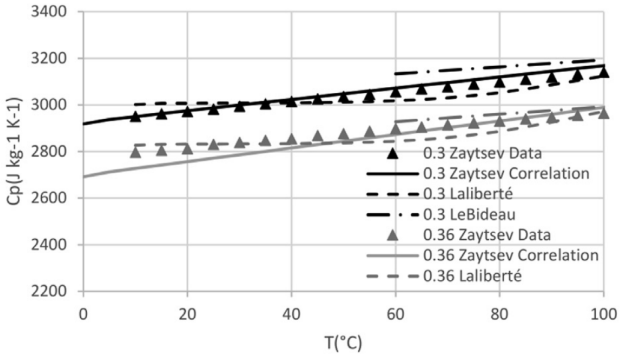

Figure A.4: Specific heat of 30 wt% KOH dependence of temperature at atmospheric pressure. [29].

A.1.5. Thermal conductivity.

The influence of temperature on the thermal conductivity of 30 wt% KOH at atmospheric pressure is presented in figure A.5. D. Le Bideau [29] shows that for aqueous electrolytes the thermal conductivity increases with increasing pressure. The thermal conductivity of water increases with 3% for all temperatures when increasing pressure from 1 bar to 1100 bar. Since this effect is small compared to the operating conditions of the electrolysis system, the effect is assumed to be negligible.

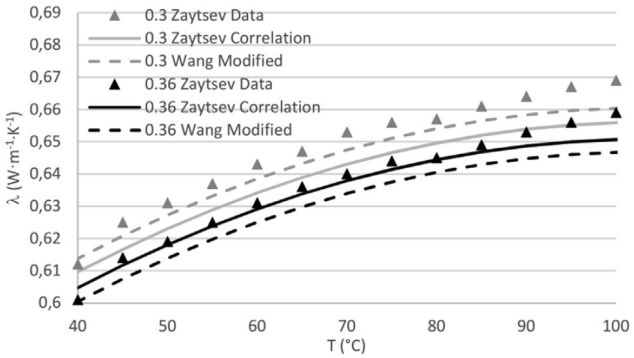

Figure A.5: Thermal conductivity of 30 wt% KOH dependence of temperature at atmospheric pressure. [29].

A.2. Electrolyser cell geometry.

In this section, the main configurations of an alkaline water electrolyser cell are treated. The cell configuration of an alkaline water electrolyser consist usually of cells that are assembled in a stack. There are two main stack designs, namely the monopolar and the bipolar stack design [53]. A geometrical aspect of alkaline water electrolysers is the gap distance between the electrodes and the diaphragm.

A.2.1. Monopolar design.

A monopolar electrolyser consists of alternating positive and negative electrodes, which are separated by porous diaphragms. The positive electrodes are connected in parallel, as are the negative electrodes, and all electrodes are immersed in a single electrolyte bath [71]. A schematic of the monopolar design is represented in figure A.6.

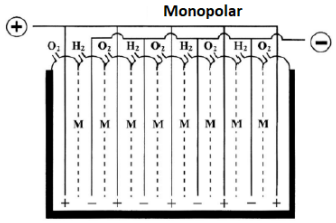

Figure A.6: Schematic of monopolar electrolyser design [53].

This is a called a unit cell, and plant scale size electrolysers are build up by connecting different units in series. In a monopolar design, each cell has the same voltage as the whole stack, while the sum of the current through each cell is the total current applied to the stack. The main advantage of a monopolar electrolyser is a simple configuration which is easy to fabricate and maintain [6]. The downside is that the design suffers from high electrical currents at low voltages. This leads to large ohmic losses. Ohmic losses and other resistance losses are discussed later in chapter 2.4.

A.2.2. Bipolar design.

With the bipolar design, the electrodes in the electrolyser cells are connected in series. This means that every electrode experiences the same current and the sum of the voltages of the cells is the total voltage that is applied to the stack. Metal bipolar plates separate each electrolyser cell, which contains two electrodes, and pass through all electronic current but do allow for (almost) no ionic current to pass through [71]. The electrical connection is only to the two outer electrodes, while all electrodes are connected in series trough the bipolar plates. Figure A.7 shows a schematic of a bipolar design.

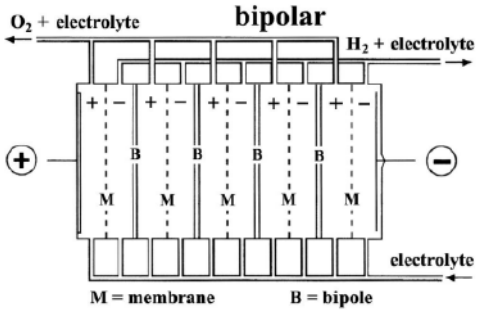

Figure A.7: Schematic of bipolar electrolyser design [53].

The advantages of a bipolar configuration are reduced ohmic losses with increase the efficiency of the design. This however, results in a precision demanding design and complex manufacturing process, to prevent electrolyte and gas leakage between cells [6].

A.2.3. Finite gap and Zero gap design.

A geometrical aspect of alkaline water electrolysers is the gap distance between the electrodes and the diaphragm. In general, most commercial AWE have a layout consisting of two solid electrodes that have a fixed distance between them an the diaphragm and The gap is filled with electrolyte. This design is called the finite gap design.

Finite gap alkaline electrolysers operate at lower current densities at low efficiencies ($< 60\%$) [44]. This effect comes from high internal resistance losses. As mentioned earlier, in chapter 2.4, does the electrolyte contributes to the ohmic losses in the electrolyser cell [71]. Earlier studies [37] showed that decreasing the electrode gap results in a lower cell voltage at lower current densities. At high current densities, the evolution of gas bubbles increases and so does the void fraction in the electrolyte. This increases the electrical resistance so a small gap is desired.

An alternative design is the zero gap design. The zero gap design consists of two porous electrodes that are compressed against each other, with in the middle a hydroxide ion conduction diaphragm. This results is a gap between the electrodes that is equal to the thickness of the diaphragm. The thickness of the diaphragm can with the zero gap design be decrease to 0.5mm or smaller. In figure A.8(a) a schematic is shown of the traditional finite gap design and the zero gap design is shown in figure A.8(b).

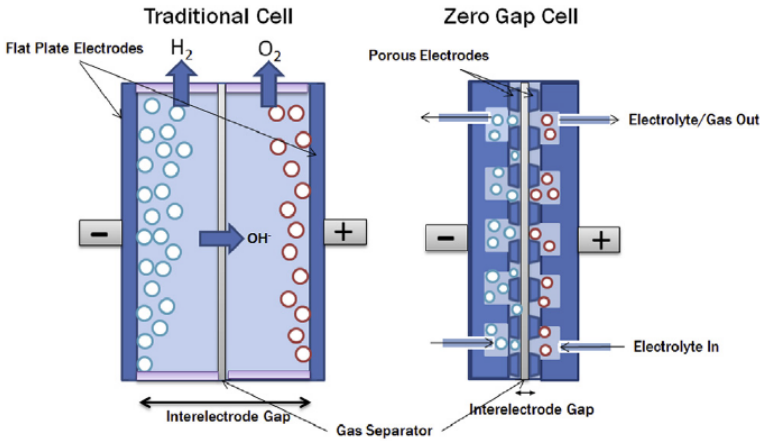

Figure A.8: Schematic of traditional finite gap design and zero gap design. [44]

A.3. Electrode kinetics

With the relation between the current and the reaction rate, the dependence of the current density on the surface potential and the composition of the electrolytic solution adjacent to the electrode surface, is given by the Butler-Volmer equation [5]. The Butler-Volmer equation can be simplified into equation A.1.

$$j = j_{cathode} - j_{anode} = j_0 \left(e^{-\alpha \frac{F \cdot \eta}{R \cdot T}} - e^{(1-\alpha) \frac{F \cdot \eta}{R \cdot T}} \right) \tag{A.1}$$

where i_0 represents the exchange current density, which is the current of the reversible water splitting reaction [71], and α refers to the electron transfer coefficient, with a value between 0 and 1 and η stands for the activation overpotential. With the

Butler-Volmer equation, the overpotential at each electrode can be derived. For relatively large overpotentials, the Butler-Volmer can be further simplified into the Tafel equation A.2[1].

$$\eta = a + b \cdot log(j) \tag{A.2}$$

Here a and b are both Tafel constants, where b represents the Tafel slope. The Tafel equation uses the Tafel slope and the exchange current density to to determine the linear relationship between the overpotential and the logarithm of current density. It also enables prediction of the rate of electrode surface reactions [57].

Figure A.9 shows a typical Tafel plot for water electrolysis. In order to compare the electrode kinetics, the Tafel slope and the exchange current density are used. If the exchange current density becomes high and the slope is lower, a higher electrode activity is achieved.

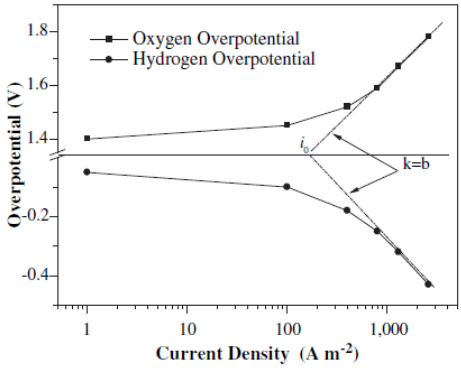

Figure A.9: Typical tafel plot for oxygen and hydrogen overpotential [71].

A.3.1. Hydrogen evolution reaction.

The reaction for the evolution of hydrogen at the cathode can be described in three steps: the Volmer, the Tafel and the Heyrovsky step [57]. The steps are shown below in respectively equation A.3, A.4 and A.5.

$$H_2O + e^- + M \rightleftharpoons M - H + OH^- \tag{A.3}$$

$$2M - H \rightleftharpoons H_2 + 2M \tag{A.4}$$

$$M - H + H_2O + e^- \rightleftharpoons H_2 + OH^- + M \tag{A.5}$$

where M denotes the electrode surface empty site. The overpotential at the cathode side can be determined with the Tafel equation, as shown in equation A.6.

$$\eta_{cathode} = 2.3\frac{RT}{\alpha F} log\frac{j}{j_0} \tag{A.6}$$

The overpotential is directly linked to the evolution of hydrogen at the cathode electrode.

A.3.2. Oxygen evolution reaction.

The oxygen evolution reaction, also known as a 2 or 4 electron step, can be describes in 5 steps [57]. The steps are shown below in respectively equation A.7, A.8, A.9, A.10 and A.11 where M denotes a site on the surface.

$$M + OH \rightleftharpoons MOH + e \tag{A.7}$$

$$MOH + OH^- \rightleftharpoons MO + H_2O + e^- \tag{A.8}$$

$$MO + OH^- \rightleftharpoons MOOH + e^- \tag{A.9}$$

$$MOOH + OH^- \rightleftharpoons MOO^- + H_2O \tag{A.10}$$

$$MOO^- \rightleftharpoons M + O_2 + e^- \tag{A.11}$$

The overpotential at the anode electrode can be determined with the Tafel equation, shown in equation A.12.

$$\eta_{anode} = 2.3\frac{RT}{(1-\alpha)F} log\frac{j}{j_0} \tag{A.12}$$

A.4. Critical bubble diameter.

The behaviour of electrolytic gas bubbles and their effect on the cell voltage in alkaline water electrolysis was studied by [73]. The study tried to predict the critical diameter for the departure of gas bubbles in the electrolyte for a vertical electrode. Two models were developed to study the behaviour of the gas bubbles. Figure A.10a shows a schematic of a gas bubble against the electrode surface. The flow of the electrode is shown as an upward flow in the x direction. Figure A.10b shows the forces that act on gas bubble. There are four main forces that act on the gas bubble. These are the buoyancy force, the surface tension force, the drag force and the lift force.

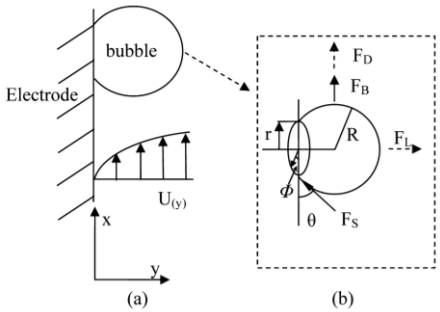

Figure A.10: (a) Gas bubble on electrode with flow direction (b) Forces acting on gas bubble. Figure adapted from Zhang et al. [71].

A.4.1. Buoyancy force.

The buoyancy force, noted as F_B, comes from the pressure and gravity acting on the mass of the gas bubble and can be expressed with equation A.13.

$$F_B = \int_{A_B} p_L(x)dA + \int_{A_C} p_B dA - \int_{V_B} \rho_B g dV \tag{A.13}$$

In the equation, A_B and A_C stand for respectively the contact surface area of the gas bubble and the electrolyte and the contact area of the gas bubble and the electrolyte. p_L and p_B are the pressures of respectively the liquid and the gas bubble. V_B stands for the volume of the gas bubble and ρ_B is the density of the gas bubble. The buoyancy force equation can be simplified into equation A.14 [60].

$$F_B = (\rho_L - \rho_B)g \cdot V_B \cdot e_x + [(\rho_B - \rho_L)g \cdot R + \frac{2 \cdot \sigma}{R}]\pi \cdot r^2 \cdot e_y \tag{A.14}$$

The volume of the gas bubble can be defined with equation A.15.

$$V_B = \frac{1}{3\pi \cdot R^3}(1 + cos(\theta))^2 \cdot (2 - cos(\theta)) \tag{A.15}$$

In the equations, ρ_L stands for the density of the liquid, θ stands for the contact angle between the liquid-solid and liquid-gas interfaces, σ is surface tension between the gas bubble and the electrolyte, R is the radius of the gas bubble and r is the circular contact area of the gas bubble with electrode surface area. e_x and e_y represent the vectors in the force is directed.

A.4.2. Interfacial tension force.

The interfacial tension force is exerted on the gas bubble at the circular contact area between the bubble and the electrode surface. It can be expressed in a x and a y direction component. Both are represented respectively by equation A.16 [60], where ϕ is the circumferential angle as shown in figure A.10b .

$$F_s = r \cdot \sigma \int_0^{2\pi} cos(\theta)cos(\phi)d\phi \cdot e_x - r \cdot \sigma \int 2\pi_0 sin \cdot g(\theta)d\phi \cdot e_y \tag{A.16}$$

A.4.3. Lift and drag forces.

The lift and drag forces acting on the gas bubble, depend on the flow velocity distribution in the electrolyser cell. They can be derived with equation A.17 and equation A.18 respectively.

$$F_L = \frac{1}{2}C_L \cdot \rho_L \cdot u_{el}^2 \cdot A_c \cdot e_y \tag{A.17}$$

$$F_D = \frac{1}{2}C_D \cdot \rho_L \cdot u_{el}^2 \cdot A_c \cdot e_x \tag{A.18}$$

In the equations, C_L and C_D respectively stand for the lift and drag coefficients and α stands for the bottom contact angle of bubble with the electrode. The electrolyte velocity is represented by u and the cross sectional area of the bubble perpendicular to the flow is represented by A_c [12]. A_c can be calculated with equation A.19.

$$A_c = \pi \cdot R^2 \left(1 - \frac{\theta - cos(\alpha)sin(\alpha)}{\pi}\right)^{1.5} \tag{A.19}$$

A.4.4. Prediction of bubble departure.

In order for the gas bubble to detach from the electrode surface, all the sum of the forces in the x direction and in the y direction should be zero. If this condition is not met, the gas bubble will lift or detach from the electrode surface. For a stagnant electrolyte, the critical diameter depends on the force in the x direction. If the gas bubbles attaches on the electrode surface, it means that the sum of the forces in the x direction is equal to the buoyancy force and both are greater than zero [73]. This is shown in equation A.20

$$\sum F_x = \sum F_B > 0 \tag{A.20}$$

The buoyancy force is not balanced with the sum of the other forces that are applied on the gas bubble. Because of the unbalance, the bubble is forced to tilt upwards where it will reach a new force balance. When the bubble cannot tilt further after it has reach a certain size, it will detach. Figure A.11 shows an upward tilting gas bubble. The contact angles are denoted as α and β.

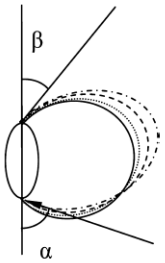

Figure A.11: Changing of gas bubble angles because of tilting.

When the bubble is moving upwards, without detaching from the electrode surface, the interfacial force in the x direction is balanced by the buoyancy force in the x direction. The relationship between the contact angles α and β and the circumferential angle can be represented by equation A.21, explained by [27].

$$\theta = \beta + (\alpha - \beta) \cdot (\frac{\phi}{\pi}) \tag{A.21}$$

When the substituted into equation A.16 and separated for the x and y components, the interfacial tension force equation results into respectively equation A.22 and equation A.23 for the x and y direction.

$$F_{S,x} = -2r\sigma \frac{\pi(\alpha - \beta)}{\pi^2 - (\alpha - \beta)^2}(sin(\alpha) + sin(\beta)) \tag{A.22}$$

$$F_{S,y} = -2r\sigma \frac{\pi}{\alpha - \beta}(cos(\beta) - cos(\alpha)) \tag{A.23}$$

With the force balance that needs to hold in order for the bubble to stay detached to the electrode surface, $F_{B,x} + F_{S,x} = 0$, and equations A.14 and A.16 the force balance can be simplified into equation A.24.

$$\frac{1}{3}(\rho_L - \rho_B)g \cdot \pi \cdot R^3 \cdot (1 + cos(\theta))^2(2 - cos(\theta)) - 2 \cdot r\sigma \frac{\pi(\alpha - \beta)}{\pi^2 - (\alpha - \beta)^2}(sin(\alpha) + sin(\beta)) \tag{A.24}$$

The critical diameter for the gas bubble, for which bubble detachment occurs, can be taken from equation A.24. The radius R is taken to the left side of the equation and multiplied by two. The calculation for the critical gas bubble diameter is shown in equation A.25

$$d_{crit} = 2 \cdot \sqrt{\frac{6sin(\theta)\sigma(\alpha - \beta)(sin(\alpha) + sin(\beta))}{(\rho_L - \rho_B)[\pi^2 - (\alpha - \beta)^2]g(1 + cos(\theta)^2(2 - cos(\theta)}} \tag{A.25}$$

In order to calculate the critical diameter of the gas bubbles at the electrode surface, a few parameters need to be obtained. The average values for the contact angle were found by [34], and showed to be 43 and 50 °C for respectively hydrogen and oxygen bubbles.

If the drag force is added to the force balance, the balance can be represented by equation A.26.

$$\frac{1}{3}(\rho_L - \rho_B)g \cdot \pi \cdot R^3 \cdot (1 + cos(\theta))^2(2 - cos(\theta)) - 2 \cdot r\sigma \frac{\pi(\alpha - \beta)}{\pi^2 - (\alpha - \beta)^2}(sin(\alpha) + sin(\beta)) + \frac{1}{2}C_D \cdot \rho_L \cdot v^2 \cdot A_c \tag{A.26}$$

This shows that when there is an electrolyte flow, the critical diameter for the bubble will decrease.

A.5. Gas crossover mechanisms.

In this chapter, the three of the contributing gas crossover mechanisms are treated, namely concentration driven mass diffusion, differential pressure driven mass convection and electro-osmotic mass drag convection.

A.5.1. Concentration driven mass diffusion.

The concentration driven gas crossover comes from mass diffusion through the diaphragm. The mass diffusion can be estimated using Fick's law [54]. When steady state is assumed, the concentration gradient of the dissolved gasses is constant across the diaphragm. This means that there is no pressure difference between the hydrogen side and the oxygen side of the electrolyser cell and that there is no flow. The molar flux can then by calculated using Fick's first law of diffusion A.27

$$\dot{n}_i^{diff} = -D_i^{eff} \cdot \frac{\partial c_i}{\partial x} = -D_i^{eff} \cdot \frac{c_{i,cathode} - c_{i,anode}}{L_{dia}} \tag{A.27}$$

where i stands for the specific component, $\dot{n}^{diff}$ is the molar flux by diffusion, $-D_i^{eff}$ is the effective diffusivity, c_i is the concentration at the cathode or the anode and L_{dia} is the thickness of the diaphragm.

From a time perspective, the rate of concentration accumulation inside the diaphragm proportional to the curvature of the concentration gradient, can be estimated with Fick's second law, as shown in equation A.28

$$\frac{\partial c_i}{\partial t} = -D_i^{eff} \cdot \frac{\partial^2 c_i}{\partial x^2} \tag{A.28}$$

The effective diffusivity can be determined based on the diffusion coefficient of the specific component in the electrolyte combined with the geometrical design of the diaphragm [20].

$$-D_i^{eff} = D_i \cdot \frac{\epsilon}{\tau} \tag{A.29}$$

Here D_i stands for the diffusion coefficient, ϵ the porosity of the diaphragm and τ for the tortuosity.

A.5.2. Differential pressure driven mass convection.

Besides mass diffusion is mass convection another mechanism that is responsible for gas crossover through the separator. The molar flux by convection can be determined with equation A.30.

$$\dot{n}_i^{conv} = u \cdot c_i \tag{A.30}$$

where u is the electrolyte velocity perpendicular through the diaphragm. The concentration difference as a function of time can be evaluated with equation A.31.

$$\frac{\partial c_i}{\partial t} = -u_{el} \cdot \frac{\partial c_i}{\partial x} \tag{A.31}$$

The differential pressure difference between the hydrogen side and the oxygen side comes from the opening of the purge valves in ZEF AWE system, which cause a pressure gradient to occur over the diaphragm. The pressure difference can be used to determine the volumetric flow rate through the diaphragm with a modification of Darcy's equation [9], shown in equation A.32.

$$\dot{V} = \frac{K_{dia} \cdot A_{dia}}{\mu \cdot L_{dia}} \cdot \Delta P \tag{A.32}$$

Here $\dot{V}$ stands for the volumetric flow rate, K_{dia} is for the permeability of the diaphragm, A_{dia} is the cross section of the diaphragm and μ stands for the dynamic viscosity of the electrolyte. From the volumetric flow rate, the electrolyte velocity can be calculated with equation

$$u_{el} = \frac{\dot{V}}{A_{dia}} \tag{A.33}$$

The permeability of the diaphragm can be determined with Kozeny's equation A.34[41].

$$K_{dia} = \frac{\epsilon \cdot d_{pore}^2}{32 \cdot \tau} \tag{A.34}$$

where d_{pore} stands for the pore diameter of the diaphragm.

A.5.3. Electro-osmotic drag driven mass convection.

Mass transfer by convection is also influenced by the phenomena electro-osmotic drag. When an AWE is under operation, the applied electric field causes hydroxide ions, OH^-, to move through the diaphragm from the cathode to anode. This can lead to dissolved gasses being dragged, with the OH^- ions ,through the diaphragm [69]. It may enhance the crossover of H_2 and reduce the crossover of O_2 [59]. Recent research was conducted by W. Haverkort [21], who reported a behaviour opposing the transport of OH^- to the anodes. The research saw that an enhanced O_2 crossover to the cathode side is possible, due to the electro-osmotic flow from the anode to the cathode dominating over the drag force.

A.5.4. Supersaturation at the electrode.

The crossover for mass transfer by convection and diffusion is influenced by the formation of supersaturated zones of dissolved gas near the electrodes, especially for zero-gap designs where the electrodes are in close contact with the diaphragm [20]. It is assumed that the evolved gasses at the electrodes are formed in dissolved state before formation of gas bubbles on the nucleation sites on the electrode surface [12]. These nucleation sites are surface irregularities which become active when a certain supersaturation level is achieved locally in the electrolyte [59]. Research was done on the mass transfer mechanics close to the electrode, to estimate the supersaturation concentration [63]. The research resulted in two relevant mass transfer mechanics, namely the mass convection from the electrode to the electrolyte bulk and mass transfer of dissolved gases from the supersaturated boundary layer at the electrode to formation of bubbles at the electrode surface area. Figure A.12 shows the mass transfer mechanics of dissolved gas at the electrode where a part of the formed gas forms a gas bubble and the other part

stays dissolved in the electrolyte bulk. In the figure N_D stands for the amount of gas produced at the electrode, N_G is the amount of gas that is evolved at the electrode surface in gas form and N_E stands for the amount of gas that is dissolved in the electrolyte bulk.

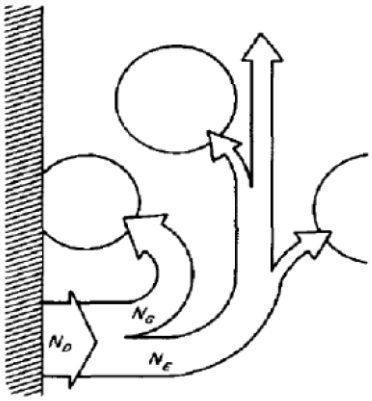

Figure A.12: Mass transfer mechanics at the electrode, with amount of gas production at the electrode, evolved gas on electrode and dissolved gas in the electrolyte bulk [64].

A.6. Electrolyser cell dimensions.

For convenience, an overview of the dimensions of the electrolyser cells is represented in table A.1. These values are used in the evaluation and modeling later in this report.

Table A.1: Dimensions of the components of an electrolyser disc.

Component	Description	Value
Disc	Diameter	130 mm
Disc	Thickness	9 mm
Bipolar plate	Thickness	0.5 mm
Top channel	Length	13.5 mm
Top channel	Width/Height	1.5 mm
Bottom channel	Length	13.5 mm
Bottom channel	Width/Height	1.5 mm
Electrode	height	85 mm
Electrode	Thickness	0.5 mm
Electrode	Surface area	60 cm^2
Diaphragm	Thickness	0.5 mm

A.7. Heat exchanger calculation.

In this chapter, the model for the calculation for a finned tube heat exchanger in the AEC system is treated. The heat exchanger is modeled to be installed in the downcomer tube to cool down the electrolyte flow to the electrolyser stack. The cooling of the electrolyte flow is done with the use of fans. Fin parameters were taken for the finned tube heat exchanger were taken from equipment present at ZEF, see table A.2 below, and can later be altered. The fan is not yet implemented in the report. The operating conditions were set a pressure of 50 bar, a current density of 0.3 A/cm^2 and a temperature of 75 °C with an electrolyte of 30wt% KOH. The thermophysical properties for the electrolyte were taken from Le Bideau et al. [29], discussed earlier in chapter A.1. The euqations used in the model were taken from VDI-Gesellschaft Verfahrenstechnik und Chemieingenieurwessen (2010) [4] and Mills, A.F (2013) [35].

Table A.2: Circular fin heat exchanger dimensions.

Symbol	Value	Description
d_o	$1.90 \cdot 10^{-2}$	Outside diameter heat exchanger tube [m]
d_i	$1.60 \cdot 10^{-2}$	Inside diameter heat exchanger tube [m]
h_f	$8.50 \cdot 10^{-3}$	Fin height [m]
d_f	$3.60 \cdot 10^{-2}$	Fin diameter [m]
s	$2.31 \cdot 10^{-3}$	fin spacing [m]
t_f	$3.00 \cdot 10^{-4}$	Fin thickness [m]

A.7.1. Matlab model.

First the heat that needs to be released from the electrolyte flow is determined based on the electrolyte mass flow the enthalpy difference over the heat exchanger, as shown in equation A.35. The electrolyte flow mass flow is taken from previous research by I. Daniil [9] with a value of $1.27 \cdot 10^{-}4kg/s$.

$$Q_{el} = \dot{m} \cdot (h_{in} - h_{out}) \tag{A.35}$$

The log mean temperature difference can be determined with the inlet and outlet temperature of the electrolyte flow in the heat exchanger tube together with the temperature of the still air. The calculation is shown in equation A.36.

$$LMTD = \frac{(T_{el,in} - T_{air}) - (T_{el,out} - T_{air})}{log(\frac{(T_{el,in} - T_{air})}{(T_{el,out} - T_{air})})} \tag{A.36}$$

The number of fins per meter for the finned heat exchanger can be determined with the fin thickness and fin spacing as shown in equation A.37.

$$Nf_{meter} = \frac{1}{t_f + s} \tag{A.37}$$

With the number of fins per meter, the number of fins for the heat exchanger can be determined with A.38. The length of the heat exchanger is based on an estimation and will later be iterated.

$$Nf = L \cdot Nf_{meter} \tag{A.38}$$

The important surface areas for the heat exchanger can be determined based on the dimensions from the actual finned heat exchanger tube. The outside surface area of the tube without fins can be calculated with the outside diameter of the tube and the length of the tube. This is shown in equation A.39

$$A_{o,tube} = L \cdot \pi \cdot d_o \tag{A.39}$$

The inside surface area of the tube can be determined with equation A.40.

$$A_{i,tube} = L \cdot \pi \cdot d_i \tag{A.40}$$

With the fin thickness, the base surface area of a fin can be determined with equation A.41.

$$A_{b,f} = t_f \cdot \pi \cdot d_o \tag{A.41}$$

With the base surface area of the fins and the outside surface area of the tube, the outside surface area of the tube that is in contact with air can be calculated as seen in equation A.42.

$$A_{air,tube} = A_{o,tube} - (Nf \cdot A_{b,f}) \tag{A.42}$$

The fin surface area in contact with the outside air can be determined with equation A.43. The fin dimensions from table A.2 are used for the calculation.

$$A_f = (0.25 \cdot \pi \cdot (d_f^2 - d_o^2) \cdot 2) + (t_f \cdot \pi \cdot d_f) \tag{A.43}$$

Now the total outer surface area, that is in contact with the outside air, can be calculated with equation A.44. This is done with the fin surface area in contact with the outside air and the outside surface area of the tube that is in contact with the air.

$$A_{o,t} = A_f + A_{air,tube} \tag{A.44}$$

The flow area of the electrolyte through the tube can be determined with A.45.

$$A_{tube} = 0.25 \cdot \pi \cdot d_i^2 \tag{A.45}$$

With the important surface and flow areas known, the velocity of the electrolyte through the heat exchanger tube can be determined. First the inlet velocity and outlet velocity are determined with respectively equation A.46 and A.47. Then the average velocity is calculated and used for further calculations with equation A.48.

$$u_{el,in} = \frac{\dot{m}}{\rho_{in} \cdot A_{tube}} \tag{A.46}$$

$$u_{el,out} = \frac{\dot{m}}{\rho_{out} \cdot A_{tube}} \tag{A.47}$$

$$u_{el,avg} = \frac{u_{el,in} + u_{el,out}}{2} \tag{A.48}$$

With the average velocity known, the Reynolds number can be determined for the electrolyte flow through the heat exchanger tube. This is done in equation A.49 with the use of the inside diameter of the tube and the average velocity, density and dynamic viscosity.

$$Re_{el} = \frac{\rho_{a,avg} \cdot u_{a,avg} \cdot d_i}{\mu_{a,avg}} \tag{A.49}$$

The Reynolds number relates to a laminar flow. For a laminar flow in smooth pipes the Nusselt number can be calculated with equation A.51, using the Prandtl number. Equation A.50 needs to be solved first in order to get the Darcy Weisbach constant.

$$f = \frac{64}{Re_{el}} \tag{A.50}$$

$$Nu_{el} = 3.66 + \frac{0.065 \cdot \frac{d_i}{L} \cdot Re_{el} \cdot Pr_{avg}}{1 + 0.04(\cdot \frac{d_i}{L} \cdot Re_a \cdot Pr_{avg})^{\frac{2}{3}}} \tag{A.51}$$

With the Nusselt number known for the electrolyte flow through the tube, the heat transfer coefficient can be calculated as show in equation A.52. For the calculation, the Nusselt number, Thermal conductivity.

$$h_{c,el} = \frac{Nu_{el} \cdot k_{el}}{d_i} \tag{A.52}$$

The natural convection from the heat exchanger to the environment can be determined based on the Rayleigh number and a Prandtl number function. In order to calculate the Rayleigh number, first the mean film temperature must be determined with equation A.53. With the mean film temperature, B' can be determined as shown in equation A.54.

$$T_r = \frac{T_{air} + \frac{T_{a,in}+T_{a,out}}{2}}{2} \tag{A.53}$$

$$\beta' = 1/T_r \tag{A.54}$$

With B' and the corresponding dynamic viscosity, Prandtl number, gravity constant and length of the heat exchanger, the Rayleigh number can be calculated as shown in equation A.55. The air specific values were taken from REFPROP. The equation relates to convective heat loss of a cylinder.

$$Ra_L = \frac{\beta \cdot LMTD \cdot g \cdot L^3 \cdot Pr_{air}}{\nu^2} \tag{A.55}$$

Now the Prandtl number function Ψ needs to be determined with the use of equation A.56 and the Prandtl number.

$$\Psi = \left(1 + (\frac{0.492}{Pr})^{\frac{9}{16}}\right)^{\frac{-16}{9}} \tag{A.56}$$

With the Prandtl number function Ψ and the Rayleigh number, the Nusselt number can be calculated with equation A.57.

$$Nu_L = 0.68 \cdot 0.67 \cdot (Ra_L \cdot \Psi)^{\frac{1}{4}} \cdot (1 + 1.6 \cdot 10^{-8} \cdot (Ra_L \cdot \Psi))^{\frac{1}{12}} \tag{A.57}$$

With the Nusselt number known, the heat transfer coefficient between the heat exchanger and the ambient air can be determined with equation A.58.

$$h_{c,am} = \frac{k_{air}}{L} \cdot Nu_L \tag{A.58}$$

In case of using fans, the heat transfer coefficient increases due to the forced convection. Based on the type of fans, a heat transfer coefficient can be estimated.

Now the fin efficiency can be determined for the heat exchanger. First the constant Θ needs to be calculated with equation A.59, based on fin parameters. In equation A.60, the constant Θ is used to calculate the fin efficiency parameter X.

$$\Theta = \left(\frac{d_f}{d_o} - 1\right) \cdot \left(1 + 0.35 \cdot log(\frac{d_f}{d_o})\right) \tag{A.59}$$

$$X = \Theta \cdot \frac{d_o}{2} \cdot \sqrt{\frac{2 \cdot h_{c,am}}{k_f \cdot t_f}} \tag{A.60}$$

With the fin efficiency parameter calculated, the fin efficiency can be determined with equation A.61.

$$\gamma_f = \frac{tanh(X)}{X} \tag{A.61}$$

The virtual heat transfer coefficient needs to be calculated in order to determine the heat transfer coefficient E, The values used for the calculation are the natural convection from the heat exchanger to the air, the surface area of the fins and the total outer surface area that is in contact with the outside air, as shown in equation A.62.

$$h_{c,v} = h_{c,am} \cdot \left(1 - (1 - \gamma_f) \cdot \frac{A_f}{A_{t,o}}\right) \tag{A.62}$$

Now with the use of the virtual heat transfer coefficient the heat transfer coefficient E can be calculated as shown in equation A.63 and equation A.64.

$$\frac{1}{E} = \frac{1}{h_v} + \frac{A_{o,t}}{A_i} \cdot \left(\frac{1}{h_{c,a}} + \frac{d_o - d_i}{2 \cdot k_s}\right) \tag{A.63}$$

$$E = (\frac{1}{E})^{-1} \tag{A.64}$$

With the log mean temperature difference, the heat transfer coefficient E and the desired heat release from the heat exchanger, the necessary heat exchanger surface area can be determined. This is shown in equation A.65.

$$A_{heat} = \frac{Q_{el}}{E \cdot LMTD} \tag{A.65}$$

Finally, the desired length for the heat exchanger can be determined with equation A.66.

$$L = \frac{A_{heat}}{A_{o,t}} \cdot 0.25 \tag{A.66}$$

A.8. Ultrasound Doppler Velocimetry method.

In pulsed ultrasound Doppler, an emitter sends periodically short ultrasonic bursts to target particles that are present in the path of the ultrasonic beam. The echoes of these ultrasonic bursts from the particles are collected by a receiver. By sampling the incoming echoes, at the same time relative to the emissions of the bursts, the velocity of the particles can be computed [13]. A special viscous gel is used to conduct the ultrasonic waves from the transmitter to the object in which the velocity is measured. In figure A.13 a visual is shown of the pulsed ultrasound Doppler method, where the red wave stands for the ultrasonic burst send from the device and the blue wave stands for the echo of the ultrasonic burst.

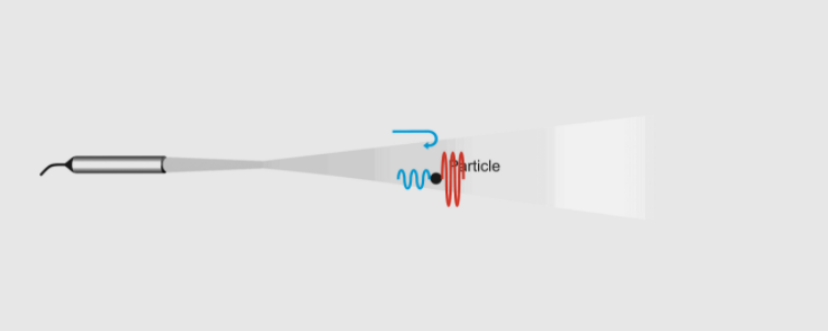

Figure A.13: Visual of periodically short ultrasonic waves (red) send to a particle and echo (blue) [13].

A.8.1. Depth measurement.

A more detailed explanation how the depth of particles is measured is given in the chapter. The explanation is done based on a situation illustrated in figure A.14. In this situation, there is only one moving particle present in the path of the ultrasonic beam.

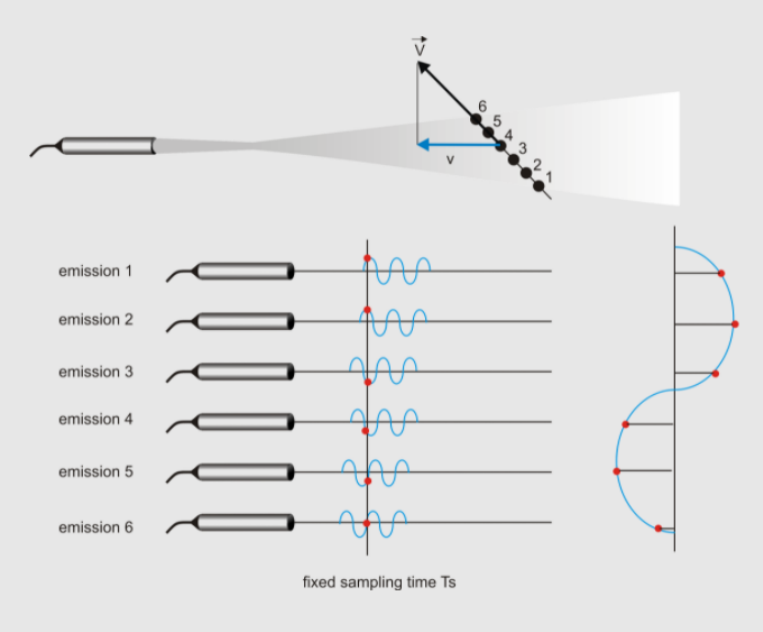

Figure A.14: Velocity measured based on ultrasound emissions [13].

When t is equal to zero, T0, an ultrasonic burst is emitted. The burst travels through the liquid to the particle, which it reaches at T1. If the particle size is much smaller than the wavelength, a small echo is generated, called the scattering effect. The echo travels back to the receiver which it reaches at T2. The depth of the particle can be determined based on the traveling time of the ultrasonic burst, as shown in equation A.67.

$$Depth = \frac{C}{2 \cdot (T2 - T0)} \tag{A.67}$$

where C stands for the sound velocity of the acoustic wave in the liquid. With UDV, the bursts are emitted periodically. After each emission, the signal from the echo is sampled at a fixed delay after the emission. If the particle moves between the successive emissions, values taken from the samples taken at sample time Ts will change over time.

A.8.2. Velocity measurement.

The frequency of the sinusoidal signal, f_d is named after the Doppler frequency and directly connected to the velocity of the particle. The velocity can be determined based on this frequency as shown in equation A.68, where f_e stands for the frequency of the emitted burst and α stands for the angle of the ultrasonic beam with respect to the moving particle.

$$u_{UDV} = \frac{f_d \cdot C}{2 \cdot f_e \cdot cos(\alpha)} \tag{A.68}$$

When there are many particles present in the ultrasonic beam, the echoes from each particle may combine into a random echo signal. In figure A.15 such a case is presented. When there is a low degree of correlation between the different emissions, the velocity reading may be incorrect.

Figure A.15: Randomly distributed particle in ultrasonic beam [13].

A.8.3. Ultrasound scattering.

The ultrasonic wave that are generated are confined inside a narrow cone. As the wave travel in the cone, they might reflect or scatter when they reach a particle with a different acoustic impedance. The acoustic impedance is defined as the density of the material multiplied by the acoustic sound velocity, presented in equation A.69.

$$Z = \rho \cdot C \tag{A.69}$$

If the size of a particle is larger than the wavelength, the ultrasonic wave will reflect and refract by the particle, as shown in figure A.16(a). This will affect the direction of propagation and the intensity of the ultrasonic wave. If the particle is much smaller than the wave length, a different phenomena takes place called scattering. When this happens, a very small amount of the ultrasonic wave is reflected back to the receiver, called backward scattering, made visual in figure A.16. This however does not affect the direction of propagation or the intensity. This shows that UDV needs smaller particles than the wave length in order to get a reliable velocity measurement.

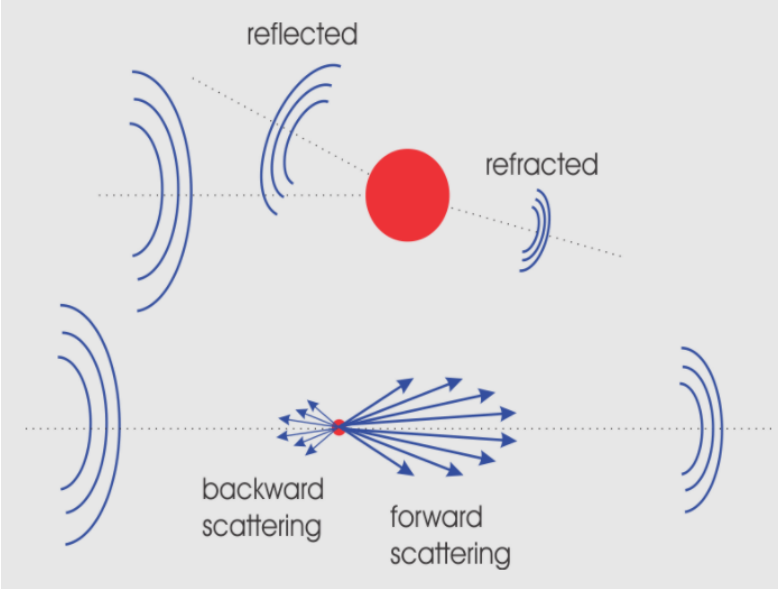

Figure A.16: Visual of pulsed Doppler method [13].

A.9. Comparison of different electrolyser systems.

In figure A.17 the typical specifications for different electrolyser systems are compared.

Specification	Units	Alkaline	PEM	SOE
Technology maturity		Widespread commercialization	Commercialization	Research &Development
Cell temperature	°C	60–80	50–80	900–1000
Cell pressure	bar	< 30	< 30	< 30
Current density	A cm^{-2}	< 0.45	1.0–2.0 [a]	0.3–1.0
Cell voltage	V	1.8–2.4	1.8–2.2	0.95–1.3
Voltage efficiency	%	62–82	67–82	81–86
Specific system energy consumption [b]	kWh Nm^{-3}	4.2–4.8	4.4–5.0	2.5–3.5
Minimum partial load	%	10–40	0–10 [c]	-
Cell area	m^2	3–3.6	< 0.13	< 0.06
Hydrogen production per stack [d]	$Nm^3 h^{-1}$	< 1400	< 400	< 10
Stack lifetime	kh	55–120	60–100	8–20 [e]
System lifetime	year	20–30	10–20	-
Hydrogen purity	%	> 99.8	99.999	-
Cold start-up time	min	15	< 15	> 60
Investment costs	€ kW^{-1}	800–1500	1400–2100	> 2000 [e]

Figure A.17: Typical specifications for different electrolyser systems [10].

A.10. Bubble observations.

During operation of the electrolyser it was observed that bubbles tend to get stuck between the holes of the electrode, especially at high pressures. When operating at a low pressure, the higher produced volume of oxygen gas when, compared to operating at a high pressures, results in the continues generation of bubbles in the electrode holes. This is visualized in figure A.18 for operating at a pressure of 2 bar and a current density of 0.3 A/cm^2.

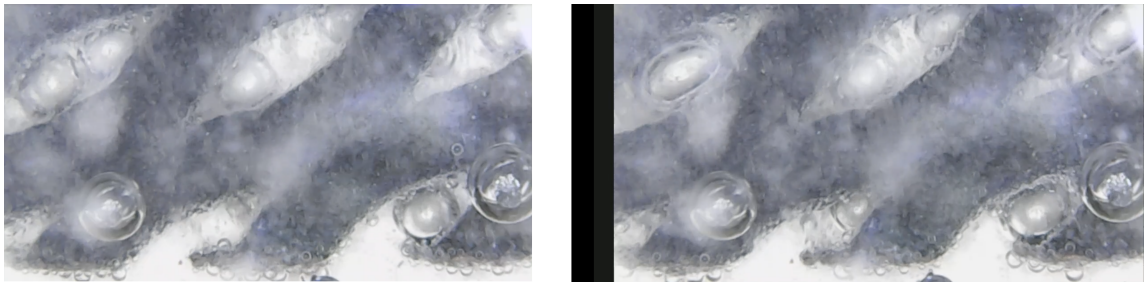

Figure A.18: Bubbles can be seen stuck between the electrode holes. Images from operation at a pressure of 2 bar and a current density of 0.3 A/cm^2.

When operating at a pressure range of 47-50 bar bubbles can be seen between the electrode and the Zirfon Diaphragm during operation. The bubbles seem to be generated between the Zirfon diaphragm and the electrode, growing in size during operation. This is observed for all operating current densities. In figure A.19 a bubbles stuck between the Zirfon diaphragm and the electrode can be observed. These bubbles grow slowly in size and tend to get stuck for entire experiments. When the pressure is relieved from the system, the bubbles grow in size and the cavity between the electrode and the diaphragm. This observation shows that the Zero-gap design might not be Zero-gap after all.

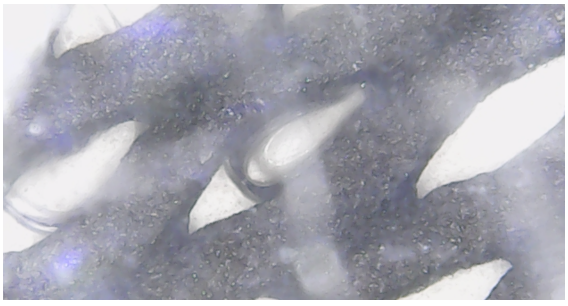

Figure A.19: Bubble being stuck between the electrode and the Zirfon diaphragm when operating at a pressure range of 47-50 bar and at a current density of 0.1 A/cm^2.

During a flow stagnation cycle, the electrode seem to become dry due to the build up of oxygen volume gas. During some experiments, bubbles can be seen stuck in the liquid film on the electrode surface. This validates the assumption that a thin film is present on the electrode surface during a flow stagnation cycle. The observation is shown in figure A.20.

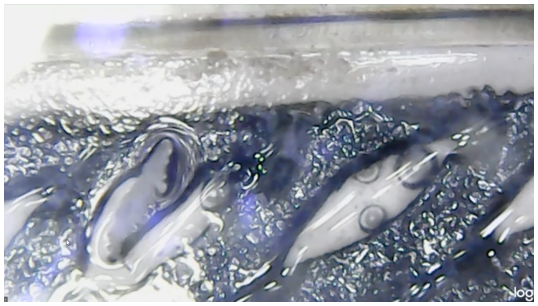

Figure A.20: Bubbles seen stuck in the liquid film on the surface of the electrode and in the electrode holes during a flow stagnation cycle, the moment the electrode seems to become dry.

Bibliography

[1] RM Abouatallah, DW Kirk, SJ Thorpe, and JW Graydon. Reactivation of nickel cathodes by dissolved vanadium species during hydrogen evolution in alkaline media. *Electrochimica Acta*, 47(4):613–621, 2001.

[2] Lara Adrian, Ronald J Adrian, and Jerry Westerweel. *Particle image velocimetry*. Number 30. Cambridge university press, 2011.

[3] J Bard Allen and R Faulkner Larry. *Electrochemical methods fundamentals and applications*. John Wiley & Sons, 2001.

[4] VDI Heat Atlas. *VDI-Gesellschaft Verfahrenstechnik und Chemieingenieurwesen*. 2010.

[5] Allen J Bard, Larry R Faulkner, et al. Fundamentals and applications. *Electrochemical Methods*, 2(482):580–632, 2001.

[6] John O'M Bockris, Brian E Conway, Ernest Yeager, and Ralph E White. Comprehensive treatise of electrochemistry. 1980.

[7] Jun Chi and Hongmei Yu. Water electrolysis based on renewable energy for hydrogen production. *Chinese Journal of Catalysis*, 39(3):390–394, 2018.

[8] Alejandro N Colli, Hubert H Girault, and Alberto Battistel. Non-precious electrodes for practical alkaline water electrolysis. *Materials*, 12(8):1336, 2019.

[9] Ilias Daniil. *Transient modeling and control of a small-scale and self-pressurized electrolysis system*. PhD thesis, Delft University of technology, 2021.

[10] Martín David, Carlos Ocampo-Martínez, and Ricardo Sánchez-Peña. Advances in alkaline water electrolyzers: A review. *Journal of Energy Storage*, 23:392–403, 2019.

[11] Peggy M Dunlap and Sam R Faris. Surface tension of aqueous solutions of potassium hydroxide. *Nature*, 196(4861): 1312–1313, 1962.

[12] John Eigeldinger and Helmut Vogt. The bubble coverage of gas-evolving electrodes in a flowing electrolyte. *Electrochimica Acta*, 45(27):4449–4456, 2000.

[13] Islam Fetoui. Multiphase flow regimes, Nov 2017. URL `https://production-technology.org/multiphase-flow-regimes/`.

[14] Islam Fetoui. Multiphase flow regimes, Nov 2017. URL `https://production-technology.org/multiphase-flow-regimes/`.

[15] Tatsuki Fujimura, Wakana Hikima, Yasuhiro Fukunaka, and Takayuki Homma. Analysis of the effect of surface wettability on hydrogen evolution reaction in water electrolysis using micro-patterned electrodes. *Electrochemistry Communications*, 101:43–46, 2019.

[16] Alan B Gancy and S Barry Brummer. Conductance of aqueous electrolyte solutions at high pressures. data for eleven 1, 1 electrolyte systems. *Journal of Chemical & Engineering Data*, 16(4):385–388, 1971.

[17] Mitch Geraedts. *Assessing the physical phenomena within stacked miniature alkaline electrolysis cells with regards to convective flow and bypass currents*. PhD thesis, Hague University, 2019.

[18] SD Hamann and M Linton. Electrical conductivities of aqueous solutions of kcl, koh and hcl, and the ionization of water at high shock pressures. *Transactions of the Faraday Society*, 65:2186–2196, 1969.

[19] M Hammoudi, C Henao, K Agbossou, Y Dubé, and ML Doumbia. New multi-physics approach for modelling and design of alkaline electrolyzers. *International Journal of Hydrogen Energy*, 37(19):13895–13913, 2012.

[20] Philipp Haug, Matthias Koj, and Thomas Turek. Influence of process conditions on gas purity in alkaline water electrolysis. *International Journal of Hydrogen Energy*, 42(15):9406–9418, 2017.

[21] JW Haverkort. Modeling and experiments of binary electrolytes in the presence of diffusion, migration, and electro-osmotic flow. *Physical Review Applied*, 14(4):044047, 2020.

[22] Isaac Herraiz-Cardona, E Ortega, J García Antón, and Valentín Pérez-Herranz. Assessment of the roughness factor effect and the intrinsic catalytic activity for hydrogen evolution reaction on ni-based electrodeposits. *International journal of hydrogen energy*, 36(16):9428–9438, 2011.

[23] Dohyung Jang, Hyun-Seok Cho, and Sanggyu Kang. Numerical modeling and analysis of the effect of pressure on the performance of an alkaline water electrolysis system. *Applied Energy*, 287:116554, 2021.

[24] H Janssen, JC Bringmann, B Emonts, and Volkmar Schröder. Safety-related studies on hydrogen production in high-pressure electrolysers. *International Journal of Hydrogen Energy*, 29(7):759–770, 2004.

[25] Prabhuram Joghee, Jennifer Nekuda Malik, Svitlana Pylypenko, and Ryan O'Hayre. A review on direct methanol fuel cells–in the perspective of energy and sustainability. *MRS Energy & Sustainability*, 2, 2015.

[26] Seongyul Kim, Nikhil Koratkar, Tansel Karabacak, and Toh-Ming Lu. Water electrolysis activated by ru nanorod array electrodes. *Applied physics letters*, 88(26):263106, 2006.

[27] JF Klausner, R Mei, DM Bernhard, and LZ Zeng. Vapor bubble departure in forced convection boiling. *International journal of heat and mass transfer*, 36(3):651–662, 1993.

[28] Claude Lamy and Pierre Millet. A critical review on the definitions used to calculate the energy efficiency coefficients of water electrolysis cells working under near ambient temperature conditions. *Journal of Power Sources*, 447:227350, 2020.

[29] Damien Le Bideau, Philippe Mandin, Mohamed Benbouzid, Myeongsub Kim, and Mathieu Sellier. Review of necessary thermophysical properties and their sensivities with temperature and electrolyte mass fractions for alkaline water electrolysis multiphysics modelling. *International Journal of Hydrogen Energy*, 44(10):4553–4569, 2019.

[30] Roland Lenormand, Cesar Zarcone, and A Sarr. Mechanisms of the displacement of one fluid by another in a network of capillary ducts. *J. Fluid Mech*, 135(34):337–353, 1983.

[31] RL LeRoy. Industrial water electrolysis: present and future. *International Journal of Hydrogen Energy*, 8(6):401–417, 1983.

[32] Francisco Manzano-Agugliaro, Alfredo Alcayde, Francisco G Montoya, Antonio Zapata-Sierra, and Consolarcion Gil. Scientific production of renewable energies worldwide: An overview. *Renewable and Sustainable Energy Reviews*, 18:134–143, 2013.

[33] Stefania Marini, Paolo Salvi, Paolo Nelli, Rachele Pesenti, Marco Villa, Mario Berrettoni, Giovanni Zangari, and Yohannes Kiros. Advanced alkaline water electrolysis. *Electrochimica Acta*, 82:384–391, 2012.

[34] H Matsushima, Y Fukunaka, and K Kuribayashi. Water electrolysis under microgravity: Part ii. description of gas bubble evolution phenomena. *Electrochimica acta*, 51(20):4190–4198, 2006.

[35] Anthony F Mills. *Basic heat and mass transfer*. Prentice hall, 2013.

[36] Bart Mulder. *Characterization of a high pressure alkaline electrolyser.* PhD thesis, Delft University of technology, 2021.

[37] N Nagai, M Takeuchi, T Kimura, and T Oka. Existence of optimum space between electrodes on hydrogen production by water electrolysis. *International journal of hydrogen energy*, 28(1):35–41, 2003.

[38] Mark New, Diana Liverman, Heike Schroder, and Kevin Anderson. Four degrees and beyond: the potential for a global temperature increase of four degrees and its implications, 2011.

[39] George A Olah. Beyond oil and gas: the methanol economy. *Angewandte Chemie International Edition*, 44(18):2636–2639, 2005.

[40] George A Olah, Alain Goeppert, and GK Surya Prakash. Chemical recycling of carbon dioxide to methanol and dimethyl ether: from greenhouse gas to renewable, environmentally carbon neutral fuels and synthetic hydrocarbons. *The Journal of organic chemistry*, 74(2):487–498, 2009.

[41] Turkuler Ozgumus, Moghtada Mobedi, and Unver Ozkol. Determination of kozeny constant based on porosity and pore to throat size ratio in porous medium with rectangular rods. *Engineering Applications of Computational Fluid Mechanics*, 8(2): 308–318, 2014.

[42] NL Panwar, SC Kaushik, and Surendra Kothari. Role of renewable energy sources in environmental protection: A review. *Renewable and sustainable energy reviews*, 15(3):1513–1524, 2011.

[43] Robert Phillips and Charles W Dunnill. Zero gap alkaline electrolysis cell design for renewable energy storage as hydrogen gas. *RSC advances*, 6(102):100643–100651, 2016.

[44] Robert Phillips, Adam Edwards, Bertrand Rome, Daniel R Jones, and Charles W Dunnill. Minimising the ohmic resistance of an alkaline electrolysis cell through effective cell design. *International Journal of Hydrogen Energy*, 42(38):23986–23994, 2017.

[45] AH Abdol Rahim, Alhassan Salami Tijani, Muhammad Fadhlullah, S Hanapi, and KI Sainan. Optimization of direct coupling solar pv panel and advanced alkaline electrolyzer system. *Energy Procedia*, 79:204–211, 2015.

[46] Md Mamoon Rashid, Mohammed K Al Mesfer, Hamid Naseem, Mohd Danish, et al. Hydrogen production by water electrolysis: a review of alkaline water electrolysis, pem water electrolysis and high temperature water electrolysis. *Int. J. Eng. Adv. Technol*, 4(3):2249–8958, 2015.

[47] Konstantin Räuchle, Ludolf Plass, Hans-Jürgen Wernicke, and Martin Bertau. Methanol for renewable energy storage and utilization. *Energy Technology*, 4(1):193–200, 2016.

[48] Hannah Ritchie and Max Roser. Annual total co□ emissions, by world region, Dec 2020. URL https://ourworldindata.org/grapher/annual-co-emissions-by-region.

[49] Hannah Ritchie and Max Roser. Renewable energy, Dec 2020. URL https://ourworldindata.org/renewable-energy.

[50] Hannah Ritchie and Max Roser. Fossil fuels, Jan 2021. URL https://ourworldindata.org/fossil-fuels.

[51] Joeri Rogelj, Michel Den Elzen, Niklas Höhne, Taryn Fransen, Hanna Fekete, Harald Winkler, Roberto Schaeffer, Fu Sha, Keywan Riahi, and Malte Meinshausen. Paris agreement climate proposals need a boost to keep warming well below 2 c. *Nature*, 534(7609):631–639, 2016.

[52] Amitava Roy, Simon Watson, and David Infield. Comparison of electrical energy efficiency of atmospheric and high-pressure electrolysers. *International Journal of Hydrogen Energy*, 31(14):1964–1979, 2006.

[53] Diogo MF Santos, César AC Sequeira, and José L Figueiredo. Hydrogen production by alkaline water electrolysis. *Química Nova*, 36(8):1176–1193, 2013.

[54] Maximilian Schalenbach, Wiebke Lueke, and Detlef Stolten. Hydrogen diffusivity and electrolyte permeability of the zirfon perl separator for alkaline water electrolysis. *Journal of the Electrochemical Society*, 163(14):F1480, 2016.

[55] Volkmar Schröder and Kai Holtappels. Explosion characteristics of hydrogen-air and hydrogen-oxygen mixtures at elevated pressures. In *International Conference on hydrogen safety, Congress Palace, Pisa, Italy*, 2005.

[56] Shahriar Shafiee and Erkan Topal. When will fossil fuel reserves be diminished? *Energy policy*, 37(1):181–189, 2009.

[57] Tatsuya Shinagawa, Angel T Garcia-Esparza, and Kazuhiro Takanabe. Insight on tafel slopes from a microkinetic analysis of aqueous electrocatalysis for energy conversion. *Scientific reports*, 5(1):1–21, 2015.

[58] Karthick Sriram. *Thermal and flow characterisation of a small scale alkaline electrolysis system for hydrogen production*. PhD thesis, Delft University of Technology, 2019.

[59] P Trinke, P Haug, J Brauns, B Bensmann, R Hanke-Rauschenbach, and T Turek. Hydrogen crossover in pem and alkaline water electrolysis: mechanisms, direct comparison and mitigation strategies. *Journal of The Electrochemical Society*, 165 (7):F502, 2018.

[60] WGJ Van Helden, CWM Van Der Geld, and PGM Boot. Forces on bubbles growing and detaching in flow along a vertical wall. *International journal of heat and mass transfer*, 38(11):2075–2088, 1995.

[61] H Vandenborre, R Leysen, and LH Baetslé. Alkaline inorganic-membrane-electrolyte (ime) water electrolysis. *International Journal of Hydrogen Energy*, 5(2):165–171, 1980.

[62] Ph Vermeiren, W Adriansens, JP Moreels, and R Leysen. Evaluation of the zirfon® separator for use in alkaline water electrolysis and ni-h2 batteries. *International Journal of Hydrogen Energy*, 23(5):321–324, 1998.

[63] H Vogt. Mechanisms of mass transfer of dissolved gas from a gas-evolving electrode and their effect on mass transfer coefficient and concentration overpotential. *Journal of applied electrochemistry*, 19(5):713–719, 1989.

[64] Helmut Vogt. The rate of gas evolution of electrodes—i. an estimate of the efficiency of gas evolution from the supersaturation of electrolyte adjacent to a gas-evolving electrode. *Electrochimica acta*, 29(2):167–173, 1984.

[65] Mingyong Wang, Zhi Wang, Xuzhong Gong, and Zhancheng Guo. The intensification technologies to water electrolysis for hydrogen production–a review. *Renewable and Sustainable Energy Reviews*, 29:573–588, 2014.

[66] MPMG Weijs, LJJ Janssen, and GJ Visser. Ohmic resistance of solution in a vertical gas-evolving cell. *Journal of applied electrochemistry*, 27(4):371–378, 1997.

[67] Hartmut Wendt and Gerhard Kreysa. *Electrochemical engineering: science and technology in chemical and other industries*. Springer Science & Business Media, 1999.

[68] Ruben Wetind. *Two-phase flows in gas-evolving electrochemical applications*. PhD thesis, Mekanik, 2001.

[69] D Wiley and G Fimbres Weihs. Encyclopedia of membranes, chap. electroosmotic drag in membranes, 2016.

[70] Junyuan Xu, Ruiying Miao, Tingting Zhao, Jun Wu, and Xindong Wang. A novel catalyst layer with hydrophilic–hydrophobic meshwork and pore structure for solid polymer electrolyte water electrolysis. *Electrochemistry communications*, 13(5): 437–439, 2011.

[71] Kai Zeng and Dongke Zhang. Recent progress in alkaline water electrolysis for hydrogen production and applications. *Progress in energy and combustion science*, 36(3):307–326, 2010.

[72] Kai Zeng and Dongke Zhang. Evaluating the effect of surface modifications on ni based electrodes for alkaline water electrolysis. *Fuel*, 116:692–698, 2014.

[73] Dongke Zhang and Kai Zeng. Evaluating the behavior of electrolytic gas bubbles and their effect on the cell voltage in alkaline water electrolysis. *Industrial & Engineering Chemistry Research*, 51(42):13825–13832, 2012.

[74] Wenyi Zhong and Joanna D Haigh. The greenhouse effect and carbon dioxide. *Weather*, 68(4):100–105, 2013.

[75] Christian Ziems, Daniel Tannert, and Hans Joachim Krautz. Project presentation: Design and installation of advanced high pressure alkaline electrolyzer-prototypes. *Energy Procedia*, 29:744–753, 2012.